A study on pressure vacuum swing adsorption based process design for carbon dioxide capture

by

Kasturi Nagesh Pai

A thesis submitted in partial fulfillment of the requirements for the degree of

Master of Science

in

CHEMICAL ENGINEERING

Department of Chemical and Materials Engineering

University of Alberta

Abstract

In order to reduce greenhouse gas emissions, realizing an energy efficient CO_2 capture process is important. Adsorption based carbon capture is a potential low energy separation technology. Although there have been considerable advances in this field, a full technological maturity of adsorption for carbon capture is yet to be achieved. The main aim of this thesis is to gain a better understanding of Pressure Swing Adsorption (PSA) design for both pre and post-combustion based CO_2 capture.

The first part of this thesis will investigate post combustion CO_2 capture. Specifically, the recently published of diamine appended metal organic frameworks (MOFs) [1, 2] that shows an unusual S-Shape isotherm for CO_2. The characteristic CO_2 uptake of these materials shows a possibility to obtain larger theoretical working capacities when compared to typical classical materials such as Zeolite 13X which are Langmuirian-type isotherms. The performance of five different materials with S-Shape isotherms in a four step Vacuum Swing Adsorption(VSA) cycle was assessed using comprehensive simulation models. The optimization of VSA processes was achieved using a genetic algorithm. The optimization results establish the key link between feed temperature and the material. The materials showed a 20% improvement in energy reduction to the benchmark adsorbent Zeolite 13X. The diamine appended MOF-Mn showed a parasitic energy of 140 kW hr / tonne CO_2 cap compared to Zeolite 13X, which is 170 kW hr / tonne CO_2 cap. The purity and recovery of CO_2 were maintained at >95% and >90%, respectively for the energy and productivity related studies.

The second part of this study deals with the design of pressure swing adsorption (PSA) cycles for implementation in a pre-combustion based CO_2 capture plant. Working in conjunction with TDA Research Inc. Colorado, we have developed novel pressure swing adsorption cycles for their patented TDA AMS-19 material. The adsorbent is an advanced physical adsorbent that is selective to CO_2 and is used for coal-derived synthesis gas separation for temperatures as high as 300°C. The overall objective of this project was to show that this new material can achieve the targets for

CO_2 purity and recovery set at 95% and 90%, respectively by the US Dept. of Energy (DOE). Six novel cycles were configured and studied in this work. The cycle configurations that achieved the DOE targets were also scheduled using a graphic scheduling approach to use in an 8 bed PSA unit, for field testing.

To my parents

Acknowledgements

I like to first thank my supervisor of the past two years, Prof. Arvind Rajendran for the opportunity to work in his research group. Arvind, I deeply appreciate your guidance throughout my Master's studies, the numerous meetings individual and with the group have been instrumental in expanding my understanding of the adsorption process. I will always be grateful for your excellent inputs with regards to the direction you have provided me for my research projects. I would also like to thank you for your patience when it comes to my various eccentricities.

I would like to extend my thanks to my group mates new and old, Ali, Libardo, Gokul, Nick, Ashwin, Johan, Parinaz, Vishal, Tai, who have made my days at the 3-336.34, DICE building, University of Alberta. highly enjoyable. I appreciate your support, patience, collaboration, and an ear whenever I needed one.

I am also very grateful to my friends here in Edmonton Deepa, Pankaj, Nitya, Naresh, Atreya. You have made me feel welcome, with an ease that is hard to find even among the best of friends. You have made my cold Edmonton winters warm and the few warm summer months cooler.

I acknowledge gratefully the funding received from TDA Research Inc., and the Natural Sciences and Engineering Research Council of Canada (NSERC). I would like to again thank the industrial partner, TDA Research Inc., and Ambal Jayaraman, for the valuable suggestions and useful discussion throughout the course of this project.

Finally, I would like to thank my parents for their constant support at every moment in my life. None of this would have been possible without your love, affection, and understanding. I would also, like to thank my brother and cousins that constantly remind me that home is always closer then you think.

Kasturi Nagesh Pai

Contents

List of Figures

List of Tables

Chapter 1

Introduction

1.1 Global Warming and Climate Change

The global scientific community is in consensus over the causes and effects related to global warming and climate change. In the past few decades, a very noticeable increase in average global temperatures has been observed [5,13]. The cause of which is understood to be an increase in carbon dioxide in the atmosphere. CO_2 is the main byproduct of burning fossil fuel. This upward trend of CO_2 concentrations in the atmosphere was first noticed in the 1950s, but began much earlier, mostly during the first part of the industrial revolution. Its concentration in the atmosphere is rising at an alarming rate. The increase of this magnitude, in such a short time, has never been observed in the measured CO_2 data [3, 4, 13]. Figure 1.1 shows the concentration of the CO_2 in parts per million (ppm) in the atmosphere. The data consists of two independently measured sources, one from Antarctic ice core samples and the other from Mauna Loa research lab, US. On the same plot, the global average temperature is plotted over the same time scale. This is plotted as a temperature anomaly, which is nothing but a normalized value of global average temperature, against the average temperature from 1951 to 1980. The circles are the individual data points for the years and the lines show a 5 year mean value.

The Paris accord of 2015 was a historic milestone for the protection of the environment, through which the world has acknowledged the existence of the phenomenon of global warming. It stipulates the reduction of greenhouse gas emissions and the quotas that have to be fulfilled by the different countries to keep global temperatures "well below 2°C" mark [14]. This can be achieved by moving to more renewable sources of energy and having a more efficient system of power transfer. But it also can be achieved through engineering solutions, such as carbon capture and sequestration, as a way to reduce the carbon dioxide in the atmosphere.

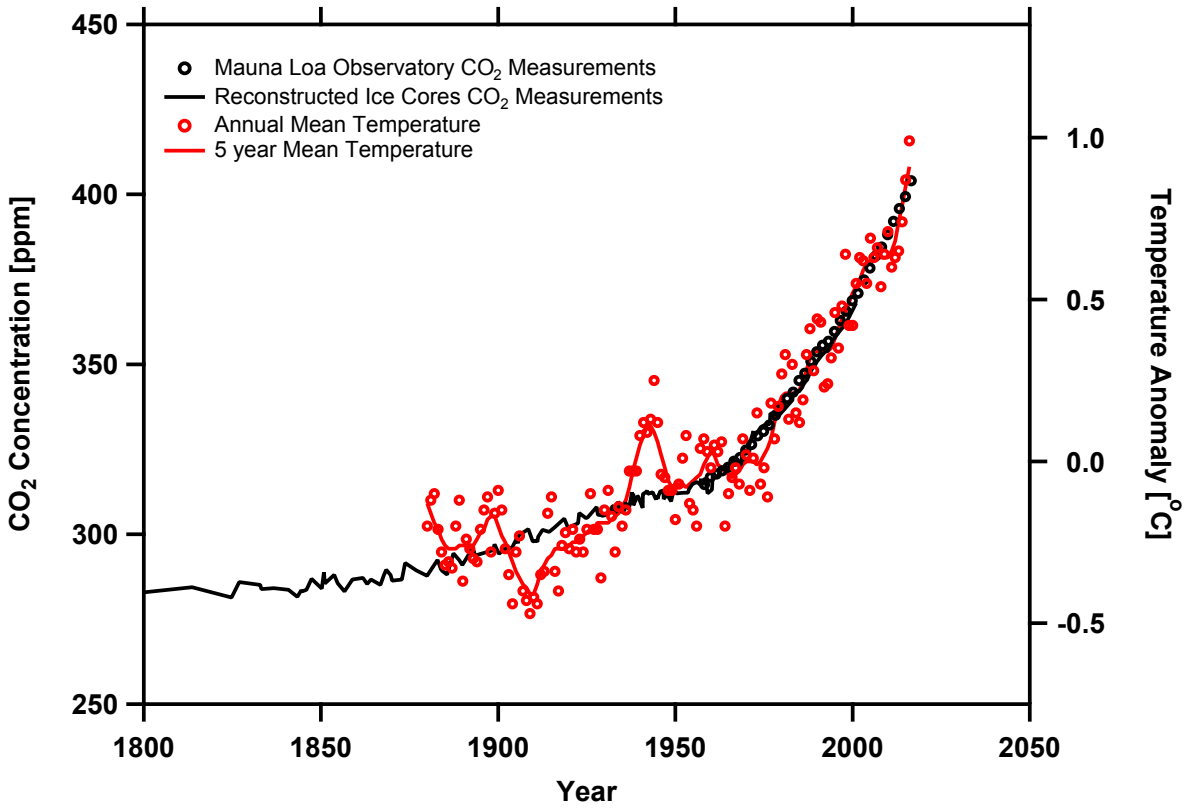

Fig. 1.1: The concentration of CO_2 (black) in the atmosphere in parts per million (ppm), the data is compiled from ice-core samples [3], and from the Mauna loa observatory measurements [4] and the red markers show the global surface temperature relative to 1951-1980 average temperatures [5].

Large point sources of CO_2, such as coal power plants, account for the bulk of the anthropogenic CO_2 produced. It is estimated that the number of coal power plants are growing particularly in Asia, and will supply 28% of the world's energy demands in 2030 [13]. All these points make the reduction of CO_2 emissions a complex engineering problem. Any approach by which the anthropogenic CO_2 emissions can be curbed while continuing to use the existing energy infrastructure needs to be studied. Carbon Capture and Storage (CCS) currently is the only technology able to deliver the significant reduction in emissions, while continuing to burn fossil fuels for energy. The use of carbon capture and sequestration technologies is in its technological infancy, and the capture process in the CCS chain has the biggest techno-economical gaps to overcome in-order for implementation. According to International Energy Agency (IEA) modeling, CCS technologies have the possibility to reduce emissions from various large and small point sources such as power generation, iron and steel, refining, petrochemical, and cement manufacturing [6]. Figure 1.2 shows that CCS could deliver a 13% reduction of the cumulative emissions reductions by 2050. This represents the capture and storage of more than 6 billion tonnes (Bt) of CO_2 emissions per year in 2050 [13].

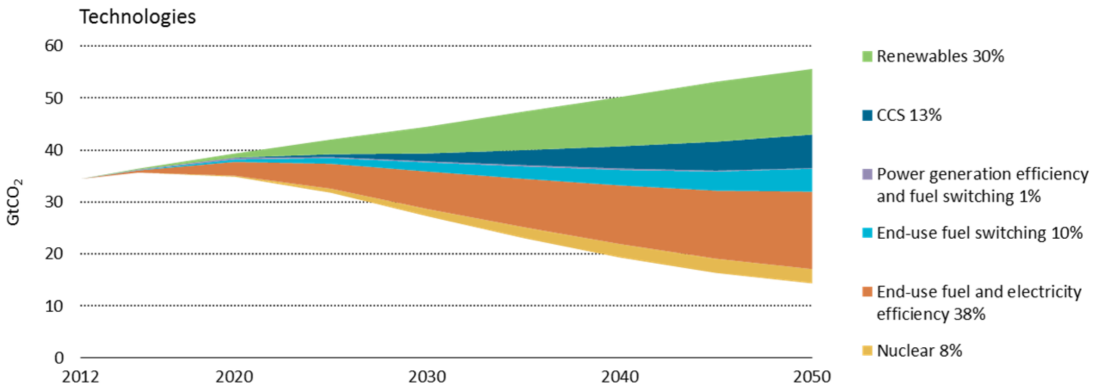

Fig. 1.2: The contribution of technologies and sectors to global cumulative CO_2 reductions [6]

1.2 Carbon Capture Technology

Carbon capture today is being implemented in various small and large scale industrial facilities. The predominant technology used for capture is generally amine based absorption. Today CCS technologies have the potential to capture around 90% CO_2 processed in a power plant. This captured CO_2 can be then compressed and stored in geologically available storage sites [15]. The combined capacity of the four major CCS projects in Canada is estimated to be around 6.4 Mtpa. This represents a 3% reduction that is needed to meet the 2030 target set by the United Nations Framework Convention on Climate Change (UNFCCC), for Canada's emissions [16, 17]. In 2016, the retrofitted coal power plant at Boundary Dam, Regina has captured and sequestered over 1 million tons of CO_2 [16, 17].

There are four main technologies available for carbon capture from large point sources, they are shown in Fig. 1.3.

- Post-combustion: In this process, the CO_2 is separated from the flue gas stream at the outlet of a fossil fuel based power plant, following the combustion of the fuel. The flue gas stream is generally a very dilute stream of CO_2 of (12-15%) and is at near atmospheric conditions of pressure and temperatures in more than 40°C. This technology can be used to retrofit currently active power plants and is thus the most mature in terms of implementation.
- Pre-combustion: In this process, the CO_2 is separated from the syn-gas that is obtained after the gasification of coal. The inlet stream in the process is made up of a higher concentration of CO_2 relative to post combustion CO_2 capture, which means that this separation can be done more efficiently than post combustion capture of CO_2. In this capture technique, the inlet stream is syngas with CO_2 concentration (35-55%) with feed pressures more than 20 bar and temperature that ranges from 200°C to 300°C. This technology is still in the early stages of development.

- Oxyfuel-combustion: Oxyfuel-combustion technology is different from the previous two technologies, i.e. it does not involve separation of CO_2 from any product or waste stream. It is rather the inlet air stream that is separated upstream for the combustion of the fossil fuel using a pure stream of O_2, obtained from an air separation unit. The exit stream comprises mainly of CO_2 and steam that can be then directly compressed and sent for storage. The main energy penalty would be the separation of O_2 from the air in the air separation unit.
- Chemical-looping combustion: This is a relatively new process for CO_2 capture and uses a metal oxide [18] to separate O_2 from the air, like oxyfuel technology. In this process, two reactors, namely, air and fuel reactor are used. In the air reactor, a metal oxide is generated in the presence of air and waste product is a gas stream, that is composed primarily of N_2. The fossil fuel along with the metal oxide is fed into the fuel reactor. The metal oxide reduces in the reaction between the fuel and this produces a waste gas stream composed of CO_2 and H_2O. In terms of performance, chemical looping can recover up to a 100% of the CO_2 generated in the fuel reactor with $> 99\%$ fuel conversion [19].

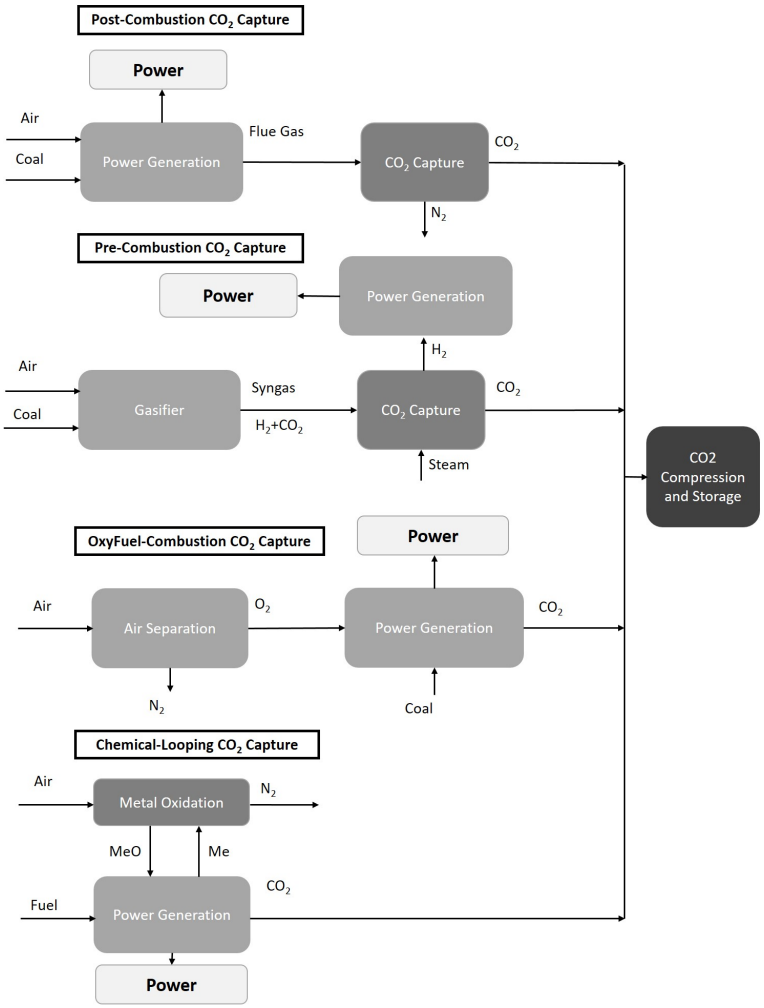

Fig. 1.3: Technologies available for CO_2 capture from large point sources of CO_2, adapted from Leung,*et,al.* [7]

1.3 Adsorbent Based Gas Separation

The fact that certain porous solids have the ability to reversibly adsorb large volumes of vapor was known even in the 18th century, but using this property in large scale industrial processes is a relatively new practice [8]. Adsorption is a mass transfer operation which is based on the attractive forces between the porous solid and the species in the gas phase.

Adsorption forces on porous media can be broadly categorized into:

- van der Waals force: These forces directly correlated to the polarizability of the adsorbing molecule.
- Electrostatic forces: These forces such as polarization forces, surface field-molecular dipole interactions and surface field gradient-molecular quadrupole interactions [20].

The adsorption process has wide spread industrial applications and is implemented in industries in large scale processes mainly in natural gas drying and other gas separations. Literature suggests that these cyclic adsorption processes show promise in CO_2 capture [21–24].

1.3.1 Adsorbents Used in Carbon Capture

Zeolites

Zeolites are porous crystalline aluminosilicates, consisting of an assembly of SiO_4 and AlO_4 tetrahedral structures in regular arrangements to form open crystal lattices. These crystals have pores with molecular dimensions into which molecules can penetrate. These also have a uniform micro-pore size distribution which makes them unique with respect to traditional micro-porous adsorbents. Nearly 200 types of zeolites are known and have been commercialized [25]. Of these, Zeolite 13X, with one of the highest capacity for CO_2, is primarily used for carbon capture applications [26]. The current research gap for post combustion CO_2 capture using Zeolites is the fact that in the presence of moisture it dramatically loses its capacity for CO_2. Thus, making capture from wet flue gas using Zeolite 13X very challenging [27–29].

Metal-Organic Frameworks

Metal-Organic Frameworks (MOFs) are a relatively new class of adsorbent, reported for the first time by Yaghi *et al.* [30]. MOFs are three-dimensional networks made up of organic and inorganic metal-ligand structures. Their structure includes metal ions that are bridged using organic ligands by coordination bonds [31]. The main interest in these materials lies in the fact that they can be designed by selecting the metal and organic linker to tailor make adsorbents for specific gas separations. MOFs have been extensively synthesized for the purpose of CO_2 capture [31]. However, there is limited process design knowledge of these materials. It is therefore not clear as to how these materials would compare to standard adsorbents such as Zeolite 13X.

Activated Carbons

Activated carbons are a class of amorphous adsorbent that has been widely studied for separation and purification of gases [8]. Their physical properties depend on both, the starting material and the activation procedure. The pore size distribution and surface polarities in activated carbons vary extensively. For gas separations such as in this thesis, smaller pore sizes are preferred with a substantial fraction of the total porosity in the micro-pore range. Activated carbons, due to their wide availability of the raw materials can be produced at a very low cost [32]. However, for carbon capture applications, are mostly restricted to pre-combustion capture systems. They are mostly hydrophilic materials, they cannot be used for high purity recovery separation of CO_2 using single

stage PVSAs without reflux streams from flue gas in post combustion, due to their relatively low CO_2 capacities and high N_2 adsorption at feed conditions [33]. But for high pressure based pre-combustion technologies, activated carbons with their CO_2 capacities being relatively higher than zeolites make for the excellent materials to run PSA based CO_2/ H_2 separations [34].

1.3.2 Cyclic Adsorption Processes

Cyclic adsorption processes use porous adsorbents to separate gas mixtures. In Fig. 1.4 and 1.5 a classical type 1 isotherm for hypothetical gas species A is shown. When a gas mixture of preferentially adsorbing gas A and a less adsorbing B, is sent through the adsorbent bed. The gas A, with a preferential affinity to the adsorbent, binds to its surface, till a certain capacity, q_{ads} is reached. This while the other gases pass through partially un-adsorbed. The less adsorbed gas stream is called the light product, the heavily adsorbed product is called the heavy product. Once the bed is saturated with the heavy product, it is regenerated. The regeneration of the adsorbent can be done in one of two ways. Application of a temperature difference or a pressure difference. When a pressure difference is applied, the process cycle is referred to as a Pressure/Vacuum Swing Adsorption (PVSA) cycle, depending on the range of pressure swing. When a temperature difference is applied, the process cycle is often referred to as a Temperature Swing Adsorption (TSA) cycle. In both cases, the regeneration of the adsorbent is done till a loading, q_{eva} is reached. The process of adsorption and regeneration is then cyclically performed to obtain the desired products. The pressure reduction is generally achieved by either by using a vacuum pump or by using an inert gas; which would be in the form of a purge. The working of a TSA unit is similar to a PSA unit, but the temperature reduction is achieved by the use of a cooling and heating stream or by the usage of an external heating/cooling fluid. TSA process is less understood for the application of direct CO_2 capture from flue gas, even though they are widely used in industrial scale processes such as gas drying.

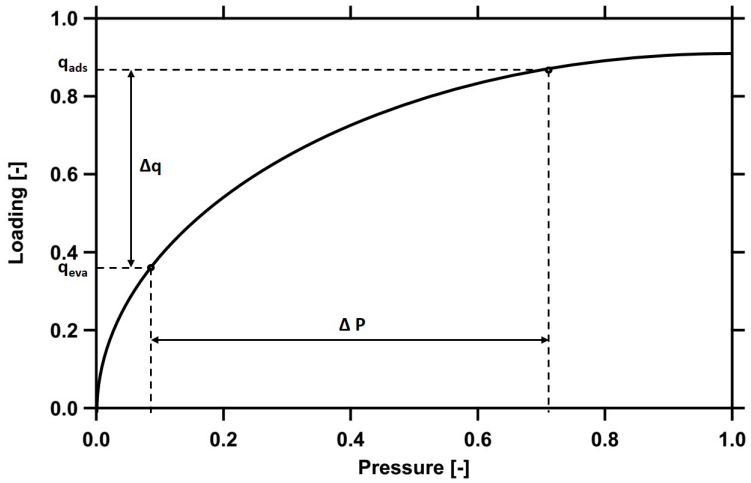

Fig. 1.4: Pressure Swing Adsorption (PSA) description [8]

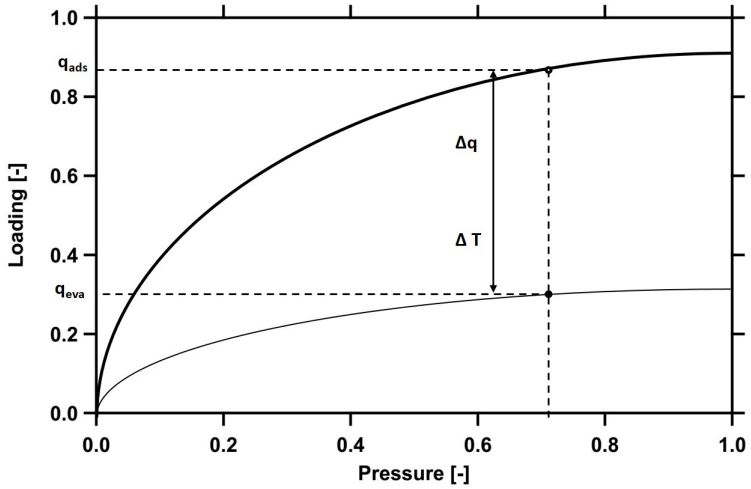

Fig. 1.5: Temperature Swing Adsorption (TSA) description [8]

Pressure Swing Adsorption

Figure 1.6 illustrates the PVSA process by showing an idealized pressure swing adsorption (PSA) process for post-combustion CO_2 capture [23]. A flue gas stream consisting of CO_2 and N_2 is introduced to a bed filled with an adsorbent that has an affinity for CO_2 over N_2. At the end of the first step, a certain amount of CO_2 has adsorbed on the surface of the adsorbent, following which the pressure of the bed is reduced to cause the excess N_2 in the bed to be released. The pressure of the bed is reduced further till Δq of CO_2 is removed from the bed. This is followed by the increase of the bed pressure back to the initial flue gas pressure. The rapid change of pressure using a vacuum pump, results in shorter cycle times and higher throughput per unit of adsorbent volume, compared to a TSA process. On the other hand, PSA process faces disadvantages, when the heavy component is too strongly adsorbed, low vacuum pressures would be needed to regenerate the adsorbent and hence, the process thus becomes economically unfeasible [10].

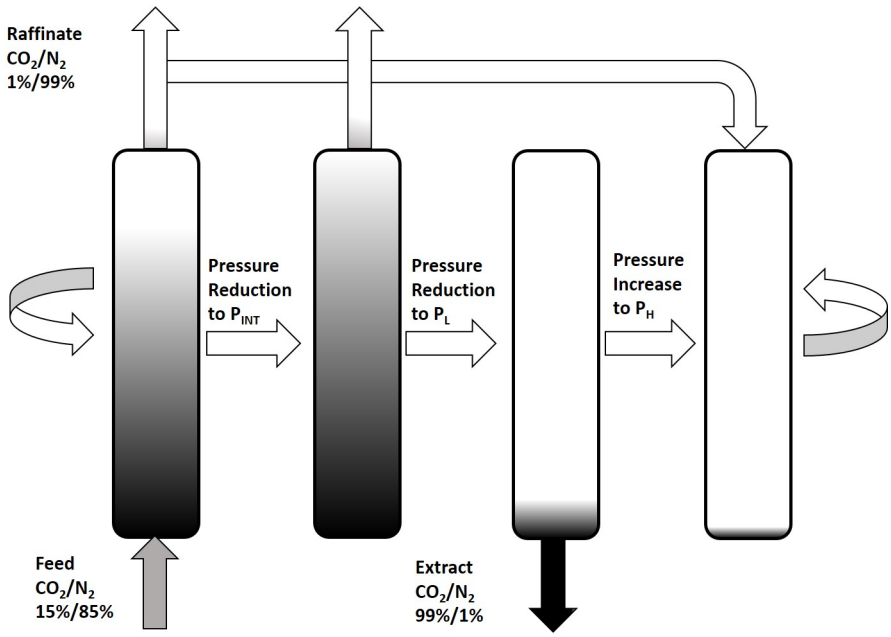

Fig. 1.6: A basic schematic for pressure swing adsorption cycle for carbon capture [8, 9]

1.4 Objectives and Outline of the Thesis

The main aim of this thesis is to study different adsorbent materials for application in both pre and post combustion CO_2 capture. The main emphasis in this work is to understand the complex dynamics of pressure vacuum swing adsorption based CO_2 separation. The thesis is divided into two main projects, the first study deals with the potential of MOF materials with non-classical adsorption equilibrium behavior for post combustion CO_2 capture. The second is a process design study for a pre-combustion based CO_2 separation technology. Both projects are analyzed and simulated based on a rigorous finite volume based code to describe the cycle steps. This will be highlighted in chapter 2 along with and multi-objective optimization scheme that is used for the optimize the various materials and processes in this thesis.

The main objectives of this thesis are described below:

- Chapter 2: Description of the mathematical modeling technique and design steps of a PSA process would be provided.
- Chapter 3: S-Shape MOFs were investigated for their potential use in PSA in CO_2 capture. The competitiveness of the CO_2 and N_2 was verified using Ideal Adsorbed Solution Theory (IAST) [35]. A detailed optimization study was carried out for a range operating condition and materials, the results are compared against the benchmark: Zeolite 13X.
- Chapter 4: PSA cycles were designed for pre-combustion capture of CO_2 from a mixture of CO_2 and H_2. This is accomplished by configuring different steps in varied sequences to find

the best performing cycle for TDA-AMS-19. The cycles and operating conditions were then scheduled using a graphical approach for implementation in an 8-bed pilot scale plant.

- Chapter 5: A brief summary of the main learning and conclusions drawn in chapter 3 and chapter 4 will be highlighted and an outlook for future work.

Chapter 2

Process Modeling and Optimization

2.1 Introduction

Designing an adsorption process requires a reliable model to describe the key transport phenomenon that occurs in the column. In this chapter, a detailed modeling strategy used to simulate the adsorption process will be described. The chapter begins with the description of various isotherm models used to model the equilibrium behavior of the gases on the adsorbent. This is followed by a brief explanation of competitive adsorption of gas species. A description of the mathematical model used to simulate the heat and mass transfer effects on the adsorption in the packed bed is presented. This is followed by the boundary conditions for the various steps used in the design of a PSA cycle. The solution strategy used to solve the model shall be discussed with a validation of the model based on mass balances. In the second part of this chapter, a brief description of the optimization strategy used for the purity/recovery and energy/ productivity optimization is given. A summary of the graphical scheduling strategy used to implement the operating conditions is also provided.

2.2 Modeling of Adsorption Equilibrium

The cornerstone for an accurate simulation and design of an adsorption process is the precise description of adsorption equilibrium data. This involves describing an equilibrium model that fits the experimental equilibrium measurements for a given adsorbent, over a range of temperature and pressure. An accurate model of adsorption equilibria would give us the adsorption capacities of different components in a gas mixture on the given adsorbent. Many models, empirical and theoretical have been proposed in the literature over the years to describe the equilibrium measurements and explained in the literature [8, 36].

2.2.1 Single Site Langmuir (SSL) Isotherm Model

One of the simplest models used to describe adsorption equilibria is Single Site Langmuir (SSL) isotherm model [37]. The model assumes that the molecules have a fixed number of sites with identical energies to adsorb on. The assumption is also made that each site accommodates only a single molecule and the interaction between molecules adsorbed on neighboring sites are absent. The SSL isotherm model is given as follows:

$$q_i^* = \frac{q_{\mathrm{s},i} b_i P_i}{1 + b_i P_i} \tag{2.1}$$

$$b_i = b_{0,i} e^{-\Delta H_{\mathrm{b},i}/RT} \tag{2.2}$$

q_i^* is the equilibrium solid phase concentration at a given temperature and pressure, $q_{\mathrm{s},i}$ is the solid phase concentration at saturation of the given component i. b_i is the adsorption equilibrium constant, which follows an Arrhenius type temperature dependence. The parameter $-\Delta H_{\mathrm{b},i}$ is the heat of adsorption, which is independent of the coverage in the adsorbent as the model assumes an adsorbent with identical sites without interactions between neighboring sites.

2.2.2 Dual Site Langmuir (DSL) Isotherm Model

Often, in many practical cases, the SSL model fails to accurately describe the equilibria, especially when adsorbents are structurally/energetically heterogeneous. In these cases, a dual-site Langmuir (DSL), which is an extension of the SSL isotherm equation is used.

$$q_i^* = \frac{q_{\mathrm{sb},i} b_i P_i}{1 + b_i P_i} + \frac{q_{\mathrm{sd},i} d_i P_i}{1 + d_i P_i} \tag{2.3}$$

where $q_{\mathrm{sd},i}$ and d_i are respectively the saturation capacity and affinity parameter for the second site. In both the single-site and dual-site models, the temperature dependence is described by the following relationships:

$$b_i = b_{0,i} e^{-\Delta H_{\mathrm{b},i}/RT} \tag{2.4}$$

$$d_i = d_{0,i} e^{-\Delta H_{\mathrm{d},i}/RT} \tag{2.5}$$

where $b_{0,i}$ and $d_{0,i}$ are the pre-exponential factors while $\Delta H_{\mathrm{b},i}$ and $\Delta H_{\mathrm{d},i}$ are the heats of adsorption. DSL isotherm model has 6 parameters, namely, $b_{0,i}$, $d_{0,i}$, $\Delta H_{\mathrm{b},i}$, $\Delta H_{\mathrm{d},i}$, $q_{\mathrm{sd},i}$, and $q_{\mathrm{sb},i}$.

2.2.3 Weighted Dual Site Langmuir (wDSL) Isotherm Model

In Chapter 3, a unique adsorption equilibria material is studied with non-classical S-Shape behavior. This shape makes it very challenging to model the process accurately [12, 38, 39]. To accurately describe the S-Shape, the authors, Hefti *et al.* [12] describe a continuous isotherm equation for CO_2 adsorption equilibrium on the diamine appended MOFs based on a variation of the classic Langmuir isotherm. The adsorption is described as a combination of two adsorption mechanisms, i.e. chemisorption and physisorption on the adsorption molecule. The inflection in the data is described using a weighting function which was based on the position of the step pressure and is described as follows:

$$w_{P,T} = \left(\frac{exp^{\frac{ln(P_i)-ln(P_{step})}{\sigma_{P_i,T}}}}{1 + exp^{\frac{ln(P_i)-ln(P_{step})}{\sigma_{P_i,T}}}} \right) \tag{2.6}$$

The CO_2 adsorption is modeled as a weighted contribution of the two sites described by

$$q_{\mathrm{L}} = \frac{q_{\mathrm{Ls}} b_{\mathrm{L}} P}{1 + b_{\mathrm{L}} P} \tag{2.7}$$

In this study, the site responsible for the physical adsorption is described using a dual site Langmuir equation Eq. 2.8

$$q_{\mathrm{U}} = \frac{q_{\mathrm{Us}} b_{\mathrm{U}} P}{1 + b_{\mathrm{U}} P} \tag{2.8}$$

The full expression is given by the equation Eq. 2.9

$$q_{\mathrm{T}} = q_{\mathrm{U}} * (w) + q_{\mathrm{L}} * (1 - w) \tag{2.9}$$

2.2.4 Sip's Isotherm Model

One of the other frequently used model used to help describe the adsorption equilibria is the Freundlich isotherm model [36]. The Freundlich isotherm model is:

$$q_i^* = K P^n \tag{2.10}$$

K and n are parameters which are temperature dependent. The parameter n is used to quantify the sharpness of the isotherm sharpness. The Freundlich isotherm model can be modified to account for the saturation of the adsorbent at high pressures such that the equilibrium loading tends to the saturation loading, $q_{\mathrm{s},i}$. In Chapter 4, the adsorption equilibria are described using one such

modified version of the Freundlich isotherm model referred to as the Langmuir-Freundlich or Sips isotherm model [40]. In this isotherm an assumption is made, that surface is heterogeneous, i.e. the sites with identical energies form an area. The entire surface of the adsorbent is an accumulation of these areas with different energy. It is assumed that there is no interaction between the different areas. In this model, the local equilibria at each of the areas are described using a Langmuir model.

$$q_i^* = \frac{q_{\mathrm{s,i}}(k_i P_i)^{s_i}}{1 + (k_i P_i)^{s_i}} \tag{2.11}$$

$$q_{\mathrm{s},i} = \omega_i e^{-\psi_i / RT} \tag{2.12}$$

$$k_i = \theta_i e^{-\phi_i / RT} \tag{2.13}$$

$$s_i = s_{1,i} atan(s_{1,i}(T - T_{\mathrm{ref}})) + s_{\mathrm{ref},i} \tag{2.14}$$

$q_{\mathrm{s},i}$ is the saturation solid phase concentration and is temperature dependent, k_i is the adsorption equilibrium constant, and s_i describes the homogeneity of the surface. s_i takes values between 0 and 1. And as s_i approaches unity, the Sips isotherm model becomes a simple Langmuir isotherm model [11].

2.2.5 Description of Competitive Isotherms

The description of competitive behavior of different gases on the adsorbent is very important to accurately describe the multi species adsorption simulations. The accurate description of multi-component behavior is tricky. However, the competition between species for adsorption is well documented in the literature. Generally, extended models and Ideal Adsorbed Solution Theory (IAST) are used to describe them. Of these, extended models are the fastest and easiest way to model competition, this system has to, however, be validated; using experiments such as break-through studies [41] or binary isotherm measurements, a general form of the extended Single Site Langmuir isotherm model is given below:

$$q_i^* = \frac{q_{\mathrm{s},i} b_i c_i}{1 + \sum_{i=1}^{n_{comp}} b_i c_i} \tag{2.15}$$

The competition of the gas species is captured by the summation of the product of the b_i and c_i, in the denominator, where i represents the components in the system.

The second approach is the usage of the competitive data calculated through the use of the IAST [35]. In this approach, the adsorbed phase is considered as ideal and the loading of the various components are calculated. In process simulations, there is a need to calculate equilibrium loading in both space and time. This makes this approach computationally tedious.

2.3 Process Design of a Pressure Swing Adsorption (PSA) Cycle

2.3.1 Model Equations

A one-dimensional dynamic mathematical model is used to best describe the dynamic variation of the heat and mass through the column, the following assumptions are made:

- An axially dispersed plug flow model is used to represent the bulk fluid flow in the system.
- The gas phase was assumed to obey the ideal gas law.
- Mass transfer kinetics within the solid phase is described by the linear driving force (LDF) model.
- Darcy's law is used to describe the pressure drop in the axial direction.
- Bed voidage and particle size were assumed to be uniform across the column.
- The fluid and adsorbent are assumed to be in thermal equilibrium.
- Temperature, pressure, and concentration gradients in the radial direction were neglected.
- Outer column wall is in equilibrium with ambient temperature.

These are general assumptions made to model adsorption [9]. Under these assumptions, mass, energy and transport equations can be derived and are shown in Table. 2.1 [9]. The description of the dimensionless quantities are shown in Table 2.2. The meaning of the symbols are provided in the nomenclature section of this work.

Model equations		
Overall mass balance	$\frac{\partial \bar{P}}{\partial \tau} = \frac{\bar{P}}{\bar{T}}\frac{\partial \bar{T}}{\partial \tau} - \bar{T}\frac{\partial}{\partial Z}\left(\frac{\bar{P}}{\bar{T}}\bar{v}\right) - \Psi\bar{T}\sum_{i=1}^{n_{\text{comp}}}\frac{\partial x_i}{\partial \tau}$	(2.16)
Component mass balance	$\frac{\partial y_i}{\partial \tau} = \frac{1}{Pe}\frac{\bar{T}}{\bar{P}}\frac{\partial}{\partial Z}\left(\frac{\bar{P}}{\bar{T}}\frac{\partial y_i}{\partial Z}\right) - \frac{\bar{T}}{\bar{P}}\frac{\partial}{\partial Z}\left(\frac{y_i\bar{P}}{\bar{T}}\bar{v}\right) - \frac{y_i}{\bar{P}}\frac{\partial \bar{P}}{\partial \tau} + \frac{y_i}{\bar{T}}\frac{\partial \bar{T}}{\partial \tau} - \Psi\frac{\bar{T}}{\bar{P}}\frac{\partial x_i}{\partial \tau}$	(2.17)
Mass transfer rate	$\frac{\partial x_i}{\partial \tau} = \alpha_i(x_i^* - x_i)$	(2.18)
Local velocity	$\bar{v} = \frac{4}{150}\left(\frac{\varepsilon}{1-\varepsilon}\right)^2 r_p^2 \frac{P_0}{\mu v_0 L}\left(-\frac{\partial \bar{P}}{\partial Z}\right)$	(2.19)
Column energy balance	$\frac{\partial \bar{T}}{\partial \tau} = \Omega_1\frac{\partial^2 \bar{T}}{\partial Z^2} - \Omega_2\frac{\partial}{\partial Z}(\bar{v}\bar{P}) - \Omega_3\bar{T}\sum_{i=1}^{n_{\text{comp}}}\frac{\partial x_i}{\partial \tau} + \sum_{i=1}^{n_{\text{comp}}}\left(\sigma_i\frac{\partial x_i}{\partial \tau}\right) - \Omega_4(\bar{T} - \bar{T_w}) - \Omega_2\frac{\partial \bar{P}}{\partial \tau}$	(2.20)
Wall energy balance	$\frac{\partial \bar{T_w}}{\partial \tau} = \Pi_1\frac{\partial^2 \bar{T_w}}{\partial Z^2} + \Pi_2(\bar{T} - \bar{T_w}) - \Pi_3(\bar{T_w} - \bar{T_a})$	(2.21)

Table 2.1: Model equations for modeling adsorption column dynamics.

$\bar{T} = \frac{T}{T_0};\ \bar{P} = \frac{P}{P_0};\ \bar{T_w} = \frac{T_w}{T_0};\ x_i^* = \frac{q_i^*}{q_s}$	$x_i = \frac{q_i}{q_s};\ \bar{v} = \frac{v}{v_0};\ Z = \frac{z}{L};\ \tau = \frac{tv_0}{L}$
$Pe = \frac{v_0 L}{D_L};\ Pe_H = \frac{\varepsilon_b v_0 L \rho_g C_{pg}}{K_z}$	$\Psi = \frac{1-\varepsilon_b}{\varepsilon_b}\frac{RT_0 q_s}{P_0}$
$\Pi_1 = \frac{K_w}{\rho_w C_{pw} v_0 L}$	$\Pi_2 = \frac{2r_{\text{in}}h_{\text{in}}L}{\rho_{\text{w}} C_{pw} v_0 (r_{\text{out}}^2 - r_{\text{in}}^2)}$
$\Pi_3 = \frac{2r_{\text{out}}h_{\text{out}}L}{\rho_w C_{pw} v_0 (r_{\text{out}}^2 - r_{\text{in}}^2)}$	$\sigma_i = \frac{(-\triangle H_i)q_s}{T_0(1-\varepsilon_b)(\rho_s c_{ps} + C_{pa} q_s \sum_{i=1}^n x_i)}$
$\Omega_1 = \frac{K_z}{(\frac{1-\varepsilon_b}{\varepsilon_b})(\rho_s C_{ps} + C_{pa} q_s \sum_{i=1}^n x_i)\varepsilon_b v_0 L}$	$\Omega_2 = \frac{C_{pg}}{(\frac{1-\varepsilon_b}{\varepsilon_b})(\rho_s C_{ps} + C_{pa} q_s \sum_{i=1}^n x_i)}\frac{P_0}{RT_0}$
$\Omega_3 = \frac{(C_{pa} q_s)}{(\rho_s C_{ps} + c_{pa} q_s \sum_{i=1}^n x_i)}$	$\Omega_4 = \frac{2h_{\text{in}}L}{\varepsilon_b r_{\text{in}} v_0 (\frac{1-\varepsilon_b}{\varepsilon_b}(\rho_s C_{ps} + C_{pa} q_s \sum_{i=1}^n x_i))}$

Table 2.2: Dimensionless groups used in model equations

2.3.2 Solution Methodology

In this section, the solution methodology, finite volume method and its implementation will be discussed. In this approach, the column is divided into N cells, each with a volume of ΔV, as shown in Fig.2.1. Any conserved quantity, f, is approximated by a cell average given by Eq. 2.22 [9] :

$$f_{(t)} = \frac{1}{\Delta V} \int V_j f(t)\, dt \tag{2.22}$$

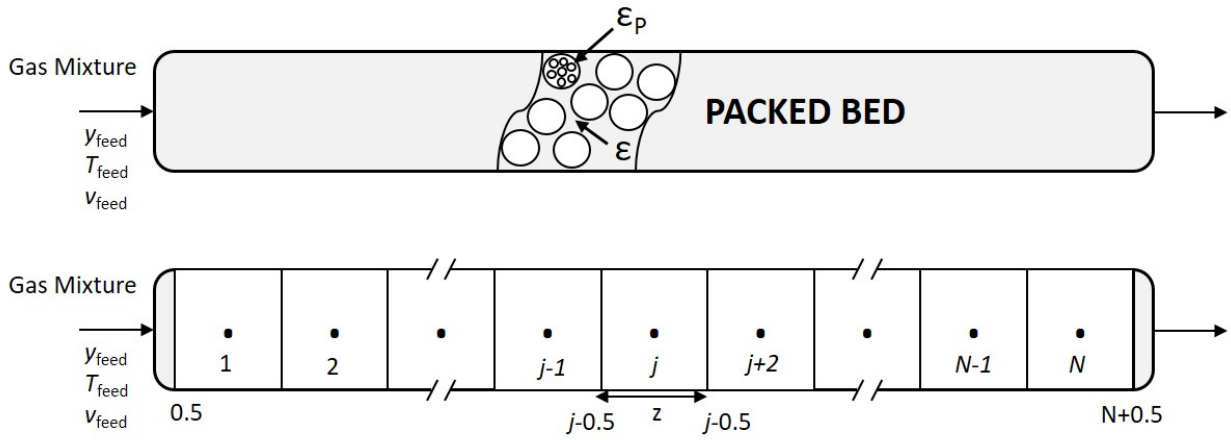

Fig. 2.1: Schematic of a column discretized in finite volume.

j is the index of each cell. The spatial derivatives in the model equations are converted to algebraic expressions by integrating over each cell j with boundaries denoted as $j_{-0.5}$ and $j_{+0.5}$.

A coarse discretization decreases the number of differential equations, thus resulting in shorter computational time but the accuracy is low. The finite volume method is known to be able to handle with sharp discontinuities which are very common in adsorption systems while using lesser volumes when compared with other methods [9]. Hence in the simulations performed in this work a discretization of 30 volumes is used and has been shown to be the best tradeoff for speed and accuracy [9]. Fig. 2.1 shows the discretization of the one-dimensional domain into cells of width Δz. The cell centers(circles) and cell edges (vertical lines); the cell numbers are shown below the filled circles and the numbers outside the column indicate cell edges and j represents the cell index. Above the discretization, an actual PSA bed is displayed for better understanding and visualization. The equations are discretized and are converted to a dimensionless form as shown in the table. The implementation of the equations was carried out in MATLAB using ode23s to solve the system of coupled differential equations.

To accurately solve the PVSA process needs the estimation of the values at the edge of the cell

be accurate. A robust high-order method should be used, here a high-resolution total diminishing (TVD) or weighted essentially non-oscillatory (WENO) method can be used [42]. In this work, a TVD method using Van Leer scheme was used [9,43]. The edge fluxes of the j^{th} cell can be obtained using this approximation. The equations for this scheme are shown as follow:

$$f_{j+0.5} = f_j + \frac{1}{2}\phi(r_{j+0.5})(f_{j+1} - f_j) \tag{2.23}$$

$$r_{j+0.5} = \frac{f_j - f_{j-1} + \delta}{f_{j+1} - f_j + \delta} \tag{2.24}$$

The successive slope ratio ($r_{j+0.5}$) is a measure of the smoothness of the solution whereas δ is constant with a very small value (10×10^{-10}) [9, 44]. Flux limiters ($\phi(r_{j+0.5})$) are used to limit the solution gradient of shocks or discontinuities.

$$\phi(r_{j+0.5}) = \frac{r_{j+0.5} + |r_{j+0.5}|}{1 + |r_{j+0.5}|} \tag{2.25}$$

Finite volume provides stability, robustness, and computational efficiency for the simulation of the adsorption process. Robustness implies that the method is able to provide accurate results even when dealing with problems that have nonlinear systems of hyperbolic equations, which model a realistic problem as the case of the cyclic adsorption [9, 44].

2.3.3 Initial and Boundary Conditions

Danckwerts's boundary conditions for a dispersed plug flow system are used for the component mass balance [9, 45]. Figure 2.2 shows the three boundary conditions used for a typical cyclic adsorption process. For the column energy balance, boundary conditions analogous to the ones used for the component mass balance are implemented for all the steps. The equations are shown in Table 2.1 is solved for the different boundary conditions to model the different steps. A summary of the boundary conditions for a general set of steps is presented in Table 2.3.

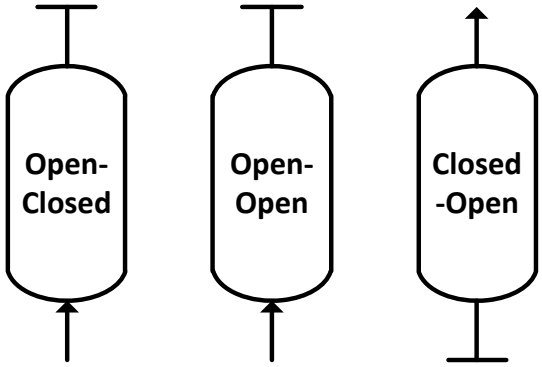

Fig. 2.2: Typical operating configurations of the constituent steps in a PSA cycle

Step	$z = 0$	$z = L$
OPEN-CLOSED	$P\|_{\mathrm{z=0}} = P_2 + (P_1 - P_2)e^{(-\alpha_p t)}$	$\frac{\partial y_i}{\partial z}\Big\|_{\mathrm{z=L}} = 0$
	$D_{\mathrm{L}} \frac{\partial y_i}{\partial z}\Big\|_{\mathrm{z=0}} = -v\|_{\mathrm{z=0}} (y_{i,\mathrm{feed}} - y_i\|_{\mathrm{z=0}})$	$\frac{\partial P}{\partial z}\Big\|_{\mathrm{z=L}} = 0$
	$\frac{\partial \mathrm{T}}{\partial z}\Big\|_{\mathrm{z=0}} = -\epsilon\, v\|_{\mathrm{z=0}}\, \rho_g C_{pg}(T_{\mathrm{feed}} - T\|_{\mathrm{z=0}})$	$\frac{\partial \mathrm{T}}{\partial z}\Big\|_{\mathrm{z=L}} = 0$
	$T_{\mathrm{w}}\|_{\mathrm{z=0}} = T_{\mathrm{a}}$	$T_{\mathrm{w}}\|_{\mathrm{z=L}} = T_{\mathrm{a}}$
OPEN-OPEN	$v\|_{\mathrm{z=0}} = v_{\mathrm{feed}}$	$P\|_{\mathrm{z=L}} = P_2$
	$D_{\mathrm{L}} \frac{\partial y_i}{\partial z}\Big\|_{\mathrm{z=0}} = -v\|_{\mathrm{z=0}} (y_{i,\mathrm{feed}} - y_i\|_{\mathrm{z=0}})$	$\frac{\partial y_i}{\partial z}\Big\|_{\mathrm{z=L}} = 0$
	$\frac{\partial,T}{\partial z}\Big\|_{\mathrm{z=0}} = -\epsilon\, v\|_{\mathrm{z=0}}\, \rho_g C_{p,\mathrm{g}}(T_{feed} - T\|_{\mathrm{z=0}})$	$\frac{\partial T}{\partial z}\Big\|_{\mathrm{z=L}} = 0$
	$T_w\|_{\mathrm{z=0}} = T_a$	$T_w\|_{\mathrm{z=L}} = T_a$
CLOSED-OPEN	$v\|_{\mathrm{z=0}} = 0$	$P\|_{\mathrm{z=L}} = P_1 + (P_2 - P_1)e^{(-\alpha_p t)}$
	$\frac{\partial y_i}{\partial z}\Big\|_{\mathrm{z=0}} = 0$	$\frac{\partial y_i}{\partial z}\Big\|_{\mathrm{z=L}} = 0$
	$\frac{\partial T}{\partial z}\Big\|_{\mathrm{z=0}} = 0$	$\frac{\partial T}{\partial z}\Big\|_{\mathrm{z=L}} = 0$
	$\frac{\partial P}{\partial z}\Big\|_{\mathrm{z=0}} = 0$	$T_w\|_{\mathrm{z=L}} = T_a$

Table 2.3: Boundary conditions for the typical steps in a cyclic adsorption process.

2.4 Pressure Swing Adsorption Steps

In the previous section, the three boundary conditions used for a typical cyclic adsorption process are highlighted. In this section; all possible steps, using in design of a pressure swing adsorption unit will be introduced [10]. The three discussed boundary conditions can be modified to be suitably used in any of the following steps. Figure.2.3 shows the various steps that can be combined in different orders to create process cycles. The design of the process cycle is based on heuristics and depends on the separation target. Any PSA system can be a sequence of the following listed steps and the sequence is decided based on the preferred outcome.

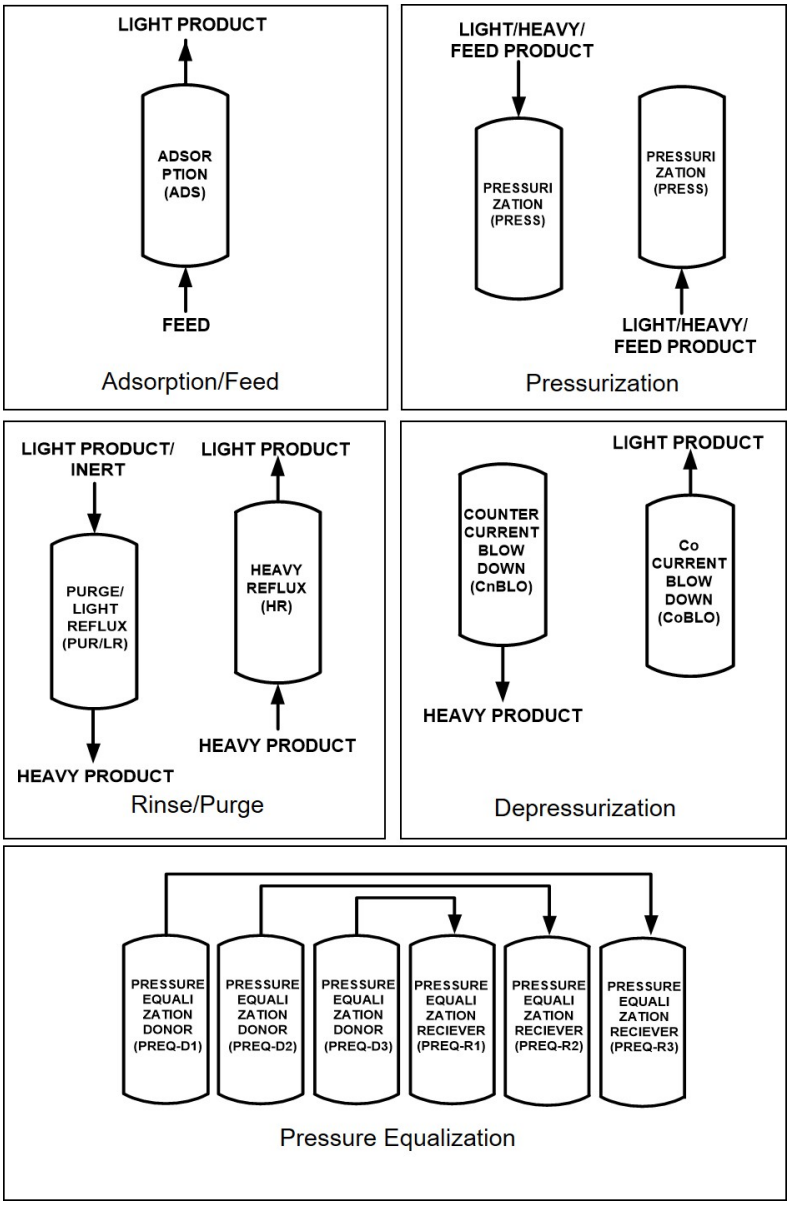

Fig. 2.3: Elementary process steps used for the designing and configuration a PSA cycle unit [10]

The first step in any cyclic adsorption process is generally pressurization, is simulated using an open closed boundary condition. It can be physically implemented at either end, of the column. Pressurization from the feed end; this can be done using the feed or using the heavy/extract product. This is done to enrich the less adsorbed species in the gas phase at the product end. Pressurization can also be done, with the light product, at the product end, this sharpens the concentration from and pushes the heavy product from closer to the feed end, which helps in recovery of the heavy product and increases the purity of the light product.

Feed/adsorption step: This step is simulated using an open-open boundary condition. The gas mixture is fed into the bed at z=0 end of the column, the gas species that preferentially adsorbs in the surface of the adsorbent is left behind. Both ends in the step are kept open and the bed is maintained at feed pressure. The product at the outlet is called light/lean/raffinate product since the heavy component has preferentially adsorbed. The light product is delivered at high pressure to the down stream unit.

Depressurization: It is simulated using, a closed open boundary condition. This step can be carried out in one of two ways. The pressure can be reduced from the z=0 end while the product end, z=L is isolated, this is called counter-current blowdown. It is done when the heavy product is required or if the light product is required with high purity. The pressure can also be reduced from the product end, this is done when the extract product is required at high purity or high recovery is needed for the raffinate product. Depending on the extent of pressure reduction these steps can be used for purification of the subsequent stream or to regenerate the bed, the latter is then referred to as evacuation step.

The rinse/purge steps have similar boundary conditions as the adsorption/ feed step, but they have various different purposes. These can be done using the feed end, z=0, as well as the product end, z=0, using either the light product, heavy product an intermediate stream or an inert stream. These are similar in function to reflux steps in distillation units and are used to increase the purity of light or heavy product. These steps can be performed at feed pressures or at reduced pressures depending on the extent of purity/recovery needed for the separation.

Pressure Equalization: This is simulated using an open-closed boundary condition. These steps are essentially ways to save energy. The basic operation of these steps is to connect the beds two different pressure, at either the feed to feed, feed to product or product to feed end. This creates a driving force to equalize the pressure of the two beds. This reduces the load on the vacuum pumps and compressors, hence saving energy. This can be done multiple times as seen from Fig. 2.3.c, but it has been shown that use of more than three such steps will be met with marginal energy saving and a large loss in productivity.

2.5 Cyclic Steady State and Model Validation

The PVSA process is inherently an unsteady state process and a sequence of dissimilar steps is performed for each cycle. The system pressure bed internal gas and solid composition and temperatures keep changing in space and time. Hence for the purpose of studying the system, a cyclic steady state has to be assumed, at which the system achieves a pseudo steady state. It is assumed that by running the same sequence of steps for a number of cycles with the same operational conditions a pseudo steady state or cyclic steady state is achieved. This condition is said to be reached when there is no change in the column profiles of all the variables in consecutive cycles n_i and n_{i+1}. In the simulations done in this work, the assumption is made that CSS is reached when the mass balance error in each of the components has not changed.

In the beginning of the simulation, it is assumed that the column is completely saturated with N_2. The same bed is cycled through each of the steps explained earlier, the internal state of the column at the end of a step is the initial condition for the subsequent step. The bed parameters for the model simulation can be found in Table 3.2. As explained earlier, a CSS needs to be achieved to analyze the performance of the process. In order to reach this condition, the mass balance constraints need to be met. Considering the adsorption step, the mass balance of the column is obtained:

$$\text{moles in} - \text{moles out} = \text{accumulation} \tag{2.26}$$

$$\text{moles in} = \frac{A\epsilon}{RT_{feed}} \int_0^{t_{ADS}} P_0 y_{feed} v_0 \, dt \tag{2.27}$$

$$\text{moles out} = \frac{A\epsilon}{RT} \int_0^{t_{ADS}} \frac{P_0 y_{(t),out} v_{(t)}}{T_{(t)}} \, dt \tag{2.28}$$

$$\text{accumulation} = \text{accumulation in fluid phase} + \text{accumulation in solid phase} \tag{2.29}$$

$$\text{accumulation in fluid phase} = \frac{LA}{R} \int_0^z \frac{P_0 y_{(z)} \epsilon}{T_{(z)}}\bigg|_{final} dz - \frac{LA}{R} \int_0^L \frac{P_0 y_{(z)} \epsilon}{T_{(z)}}\bigg|_{initial} dz \tag{2.30}$$

$$\text{accumulation solid phase} = LA \int_0^z (1-\epsilon) q_f \bigg|_{final} dz - LA \int_0^z (1-\epsilon)(q_i) \bigg|_{initial} dz \tag{2.31}$$

In the Eq 2.26 to 2.31 A, L and ϵ are the column cross sectional area, column length, and bed void-age, respectively. The mass balance for the full 4-step cycle with LPP, at CSS conditions the

moles fed into the PSA cycle is equal to the moles removed from the PSA cycle. After every cycle, the mass balance error is evaluated to verify if CSS is achieved:

$$\text{mass balance error} = \frac{|mass_{\text{in}} - mass_{\text{out}}|}{mass_{\text{in}}} * 100 \tag{2.32}$$

If the mass balance error is below 0.5% and all profiles for the variables at the end of each step for 5 consecutive cycles are the same, it can be assumed that the process has reached CSS and the simulation is stopped [9].

2.6 Optimization of a PVSA cycle

Due to the complex and transient nature of adsorption process and the complex relationship of operating conditions, optimization of a PVSA is challenging. Rigorous optimization needs to be performed to identify operating conditions to obtain optimum performance targets. For CCS the US, Dept. of Energy (DOE) has set the targeted purity and recovery for CO_2 capture to be 95% and 90%, respectively [46,47]. The optimization of a PVSA process is very complex, due to the complex relationship between the many process variables. This leads to many optimizations encountering local minimums when minimizing the optimization function. In order to avoid being placed into a local minima and to find the global minima, a genetic algorithm is used.

Genetic Algorithms are inspired by Darwin's theory of evolution and is modeled on the process of natural selection. Its search method is based on finding the optimal solution by incorporating the idea of reproduction or genetic recombination of an initial population size. The common aspects of a genetic algorithm is, recombination (or crossover), mutation and fitness.

A non-dominated sorting genetic algorithm (NSGA-II) [48] which is available on MATLAB and allows for easy parallel simulations of multiple runs of a PSA cycle was chosen as the process optimizer. Over a number of generations, the GA moves to an optimal solution but the GA is inherently stochastic in nature but it also has the ability to escape local minima, even though a global optimum is not guaranteed. In this thesis, two classes of optimization are considered: simultaneous maximization of purity and recovery; and maximization of productivity while minimizing energy with a constraint on purity and recovery.

The basic optimization routine is shown in Fig.2.4. A random sample population size of 144 is created for each of the decision variables. It was created using a Latin Hypercube Sampling (LHS), the technique to ensure an even spread in all regions for all the decision variables. This was used as an initial population and the optimization is run for 25 generations. The results of the optimization are represented as a Pareto curve, extensively shown in the next two chapters. It represents the best trade-off between the two objectives that are optimized; maximization of purity and recovery simultaneously; and maximization of productivity while minimizing energy simultaneously with a

constraint on purity and recovery. This puts the total computation time for an optimization at 25 generations ×144 population size× minutes × 12 days. A typical purity recovery optimization takes around 8-16 hours on the 24 core workstation after parallelization. All the simulations reported in this thesis were run on a 24 core computer, consisting of two INTEL Xeon processors rated at 2.5Ghz. Each simulation takes approximately 5 minutes on a single core.

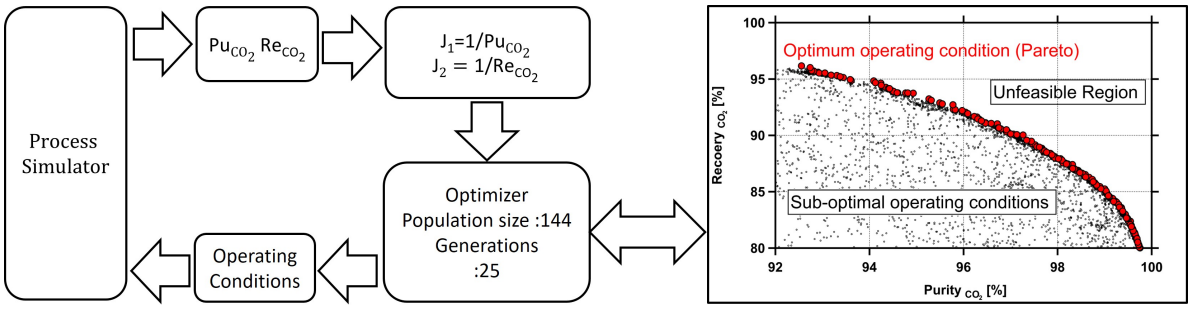

Fig. 2.4: GA based optimization scheme used for to optimize the various PSA cycles configured in this work [11]

2.7 Conclusion

In this chapter, a brief description of the modeling of adsorbents and the process simulation was presented. Different single component isotherms like SSL, DSL, wDSL, SIP's were introduced along with a discussion on competition in multi component systems. The next section dealt with the modeling of an Adsorption column and the initial and boundary condition for each type of step in PSA cycle design was discussed. A finite volume based solution scheme was discussed along with the solution methodology. After which an optimization strategy was discussed for the PSA process with a brief explanation of the genetic algorithm.

Part I

Post-Combustion Carbon Capture

Chapter 3

Post-Combustion CO_2 Capture

3.1 Introduction

Metal-Organic Frameworks(MOFs) are a class of solid crystalline adsorbents, which were first synthesized and published by Yaghi *et al.* [30]. Ever since then, many advancements have been made with regards to the synthesis of these sorbents. For instance, they can be synthesized to have tailor-made properties such as heat of adsorptions, selectivity, capacity etc. [12, 49]. This along with a large capacity of CO_2 at low partial pressures have made MOFs an intriguing material for PSA-based CO_2 capture [1, 50, 51]. Recently, McDonald *et al.* [1, 2] have published a group of diamine-appended MOFs. These show a previously unknown and unusual S-Shape uptake of CO_2. When compared to a typical type 1 adsorbent, the presence of a step change in the CO_2 isotherm can be theorized to provide larger working capacity even at high flue gas temperatures, highlighted in Fig. 3.1. The first type of these adsorbents reported was Mg_2(dobpdc), functionalized with N,N'-dimethylethylenediamine(mmen). The authors, McDonald *et al.* have also, by replacing the Mg_2 ions with other divalent metal ions, such as Mn, Fe, Co, Ni, and Zn, managed to change the strength of the MOF structure [2]. Thus, creating a new group of MOFs with adsorbent properties very different from the known convention.

The adsorption mechanism for the S-Shape CO_2 isotherm is referred to as a cooperative insertion [1]. The adsorption of a small number of CO_2 atoms reportedly destabilizes the metal-amine bonds. The destabilization of M-N bonds facilitates the adsorption of a larger number of CO_2 molecules onto the structure. This results in the sharp increase in the adsorption capacity of CO_2. This change in capacity of CO_2 gives rise to a characteristic S-Shape. These materials do not show hysteresis in CO_2 desorption when compared to other breathable MOFs with similar characteristics. They have also been reported to have a high working capacity and high CO_2/N_2 selectivity. These materials are reportedly stable under moist conditions [2, 12]. There is a lack of process based understanding in the literature; on how these novel materials would behave in a real world pressure swing adsorption

(PSA) process. The potential of these materials to achieve the US. Dept of Energy (DOE) targets for adsorption based post combustion CO_2 capture is still unknown.

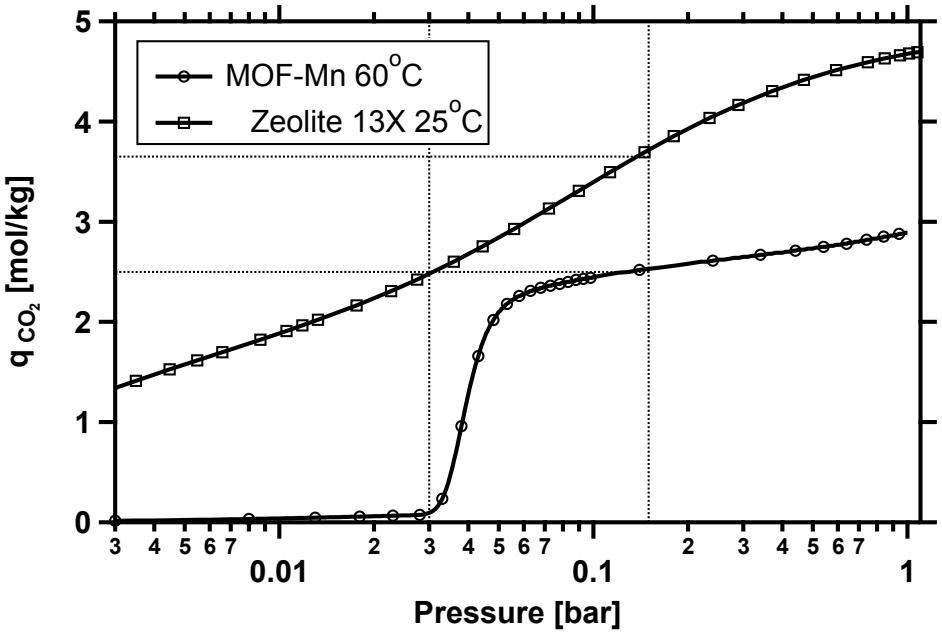

Fig. 3.1: Comparison of Zeolite 13X (squares) at 25°C and diamine appended MOF(Mn) (circles) isotherm at 60°C, showing a possible working capacity advantage for the diamine appended MOF(Mn)

In this work, the potential of these materials in a PSA based process for CO_2 capture will be investigated. The material isotherms are fitted to a wDSL isotherm to accurately capture the inflections at various different temperatures and pressures. The competition between CO_2 and N_2 is predicted using an extended form of the wDSL, the use of which is validated using IAS theory. All of the S-Shape MOFs show an inflection in CO_2 adsorption isotherm in the operating range of pressures, for vastly different temperatures. The process simulation studies are carried out primarily on; MOF-Mn, since the inflection on this material is in the range of flue gas temperatures; i.e. 50 to 70°C. Numerous optimization studies will be carried out to understand the potential of these materials. Based on which, the potential of these materials would be compared to Zeolite 13X, the benchmark for post combustion CO_2.

3.2 Modeling of Isotherm Data

3.2.1 Adsorption Equilibrium

The authors, have synthesized several variants of the diamine appended MOF structures, by replacing the Mg^{2+} ions with other divalent metal ions, specifically Mn^{2+}, Fe^{2+}, Co^{2+}, Ni^{2+} and

Zn^{2+} [2]. The structures are abbreviated henceforth in this study as MOF-X, where X stands for the relevant coordination metal. Of these MOF-Mn, MOF-Fe, MOF-Co, MOF-Zn, MOF-Mg show S-Shape CO_2 uptakes. McDonald *et al.* [2] also provided a mathematical model for the description of the adsorption isotherms of the S-Shape MOF materials. However, due to the presence of a discontinuity, this cannot be used in process simulation [12, 39]. Also due to the presence of the S-Shape it is not possible to run process simulations using standard equilibrium isotherm models such as the ones used describe type 1 materials [39].

Hefti *et al.* [12], described an alternative isotherm model called the Weighted Dual Site Langmuir isotherm (wDSL) Eq. 3.2, in which the adsorption is described as a combination of two adsorption mechanisms; chemisorption, which occurs on the terminal amines of the framework; physisorption, which occurs on the CO_2 inserted framework. The description of the S-Shape was realized using a weighting function which was based on the concentration of CO_2 and is described as follows:

$$w_{\mathrm{p,T}} = \left(\frac{exp^{\frac{(ln(C)-ln(C_{\mathrm{step}})}{\sigma_{\mathrm{C,T}}}}}{1 + exp^{\frac{(ln(C)-ln(C_{\mathrm{step}})}{\sigma_{\mathrm{C,T}}}}} \right) \tag{3.1}$$

$$q = q_{\mathrm{U}} * (w) + q_{\mathrm{L}} * (1 - w) \tag{3.2}$$

The CO_2 adsorption is modeled as, a weighted contribution of the two separate adsorption sites. In this work, we considered the site responsible for the physical adsorption is a Dual Site Langmuir (DSL), and the chemisorption is described using a Single Site Langmuir (SSL) model, both of which are described by Eq. 3.3 to 3.4

$$q_{\mathrm{L}} = \frac{q_{\mathrm{Lsat}} b_{\mathrm{L}} C}{1 + b_{\mathrm{L}} C} \tag{3.3}$$

$$q_{\mathrm{U}} = \frac{q_{\mathrm{U1sat}} b_{\mathrm{U1}} C}{1 + b_{\mathrm{U1}} C} + \frac{q_{\mathrm{U2sat}} b_{\mathrm{U2}} C}{1 + b_{\mathrm{U2}} C} \tag{3.4}$$

In this work, the wSDL model parameters had to be refitted to a concentration based isotherm to run in our in-house code. The isotherm fitting and the parameters are given in the Table.3.1.

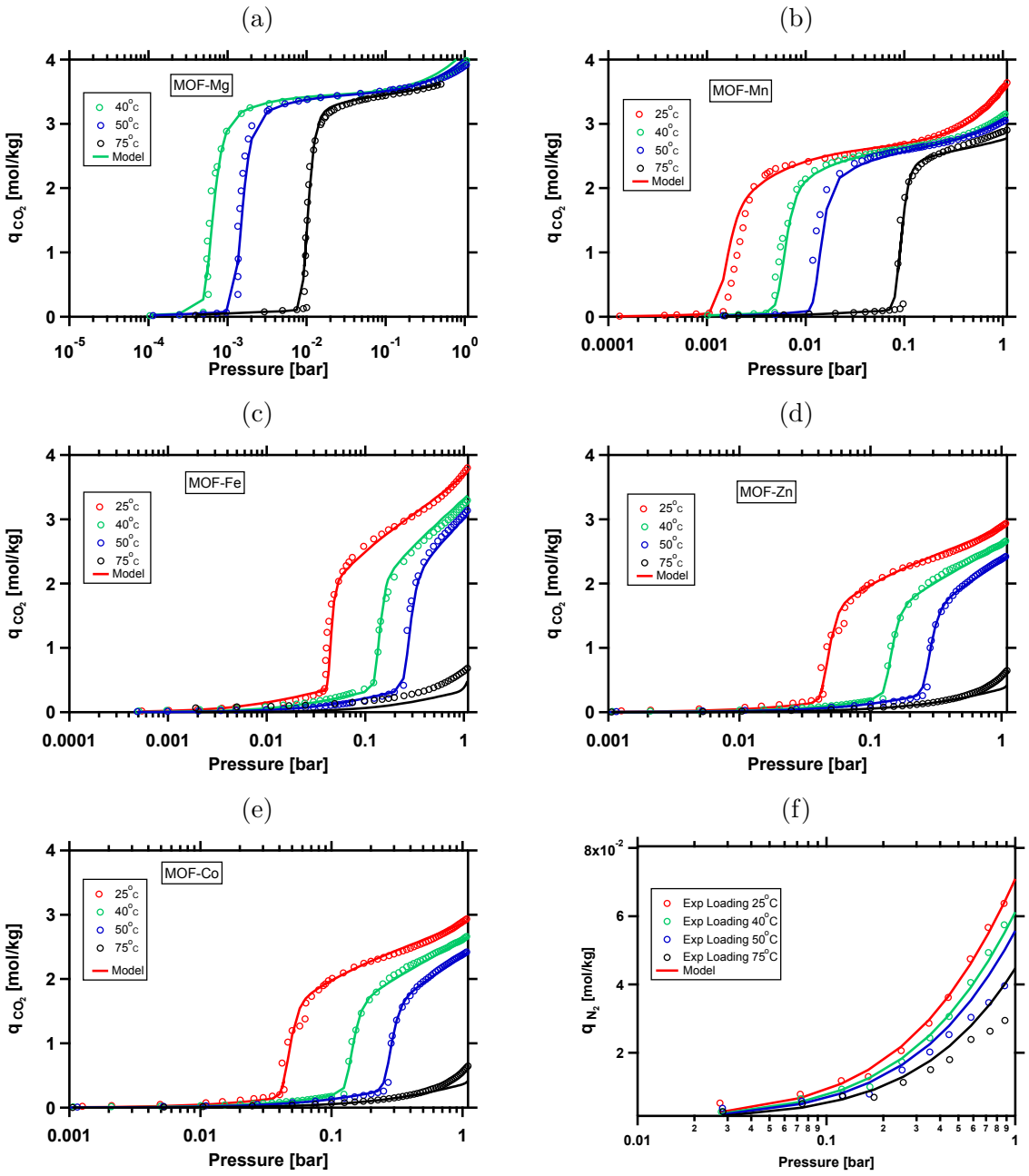

Fig. 3.2: Adsorption isotherms of the diamine appended MOF structures; MOF-X; X=Metal center, CO_2 loading for (a) MOF-Mg (b) MOF-Mn (c) MOF-Fe (d) MOF-Zn (e) MOF-Co and (f) N_2 loading used for all the MOF-X structures; markers show equilibrium loadings from McDonald *et al.* [2] at four different temperatures 25, 40, 50, 75°C and fitted adsorption isotherms (lines).

	q_{L} $[\frac{mol}{m^3}]$	q_{U1} $[\frac{mol}{m^3}]$	q_{U2} $[\frac{mol}{m^3}]$	b_{L} $[\frac{m^3}{mol}]$	b_{U1} $[\frac{m^3}{mol}]$	b_{U2} $[\frac{m^3}{mol}]$	$\delta \mathrm{H_L}$ $[\frac{kJ}{mol}]$	$\delta \mathrm{H_{U1}}$ $[\frac{kJ}{mol}]$	$\delta \mathrm{H_{U2}}$ $[\frac{kJ}{mol}]$	X_1 $[-]$	X_2 $[-]$	$P_{\mathrm{step,o}}$ [pa]	$\delta \mathrm{H_{ADS}}$ $[\frac{kJ}{mol}]$
MOF-Co	3620	3620	3620	2.5×10^{-10}	3.2×10^{-09}	3.5×10^{-07}	47.3	45.8	25.0	0.009	0	45596.25	53.5
MOF-Mn	155.94	2970.77	2938	1.2×10^{-07}	3.2×10^{-07}	7.8×10^{-08}	44.8	45.0	29.9	0.13	-900	506625	72.0
MOF-Mg	1130	3898.5	4520	2.5×10^{-05}	2.9×10^{-08}	5.6×10^{-06}	29.0	59.0	17.5	0.17	-1000	4964925	74.1
MOF-Zn	1096.1	2757.2	1582	5.4×10^{-08}	3.5×10^{-11}	4.5×10^{-06}	36.0	59.6	20.0	0.09	0	12868.28	57.3
MOF-Fe	678	3390	2599	2.4×10^{-10}	1.2×10^{-10}	1.4×10^{-06}	54.4	56.5	22.5	0.08	2500	12600	56.0
MOF-N2	226	226	226	0.0003	0.0002	0.0005	9.6	9.6	4.0	0.08	1000	12600	12.0

Table 3.1: Estimated CO_2 and N_2 adsorption isotherm parameters for the six MOF materials, fitting of the parameters is done similar to the method stated by Hefti *et al.* [12].

3.2.2 Nitrogen Isotherm and Extended wDSL model

The N_2 adsorption data was provided to us by the authors of [1,2] for only one MOF, via MOF-Mg. In this study, it was assumed that N_2 loading is the same for the other MOFs. Since the loading of CO_2 was highest for MOF-Mg and we assume that N_2 capacity would be at most similar, if not even lower for the other MOF structures. In keeping with rest of the data, the N_2 loading was fitted to the above described wDSL isotherm model and the parameters are given in Table.3.1. This was done primarily so that the isotherm could predict competition between CO_2 and N_2 accurately for all adsorption sites. The competition between the two components was described as an extended Langmuir model on each of the sites as seen in Eq.3.5 and Eq.3.6, assuming the N_2 effects each of the sites equally.

$$q_{\mathrm{L},i} = \frac{q_{\mathrm{Lsat},i} b_{\mathrm{L},i} pi}{1 + \sum_{i=1}^{n_{\mathrm{comp}}} b_{\mathrm{L},i} pi} \tag{3.5}$$

$$q_{\mathrm{U},i} = \frac{q_{\mathrm{U1sat},i} b_{\mathrm{U1},i} pi}{1 + \sum_{i=1}^{n_{\mathrm{comp}}} b_{\mathrm{U1},i} pi} + \frac{q_{\mathrm{U2sat}i} b_{\mathrm{U2},i} pi}{1 + \sum_{i=1}^{n_{\mathrm{comp}}} b_{\mathrm{U2},i} pi} \tag{3.6}$$

3.2.3 IAST Calculations

Determination of competition between gas species on the surface of an adsorbent is critical in accurately modeling a process. This can be done experimentally using binary gas mixtures using various techniques such as breakthrough experiments and gravimetric analysis. With a lack of such experimental data, validation of predicted competitive data can be validated using ideal adsorbed solution theory. It is analogous to Raoult's law for vapor-liquid equilibrium given by:

$$P_i = P_i^{\circ}(\pi_i) x_i \tag{3.7}$$

π_i and x_i are the spreading pressure and mole fraction of component i in the adsorbed phase, respectively. The mole fraction of component i in the adsorbed phase is given by:

$$x_i = \frac{q_i}{\sum_{i=1}^{n_{comp}} q_i} \tag{3.8}$$

It was proposed by Myers and Prausnitz [35], the method specifies a set of equations with the help of which multi-component adsorption equilibria can be calculated. The only input required is single component loading for each of the competing species in the mixture. In the absence of

experimental data, the IAS theory is widely used for the prediction of multi-component adsorption data [39, 52, 53]. The spreading pressure for each component is described as follows:

$$\pi_i^* = \frac{\pi_i}{RT} = \frac{n_i^0(P)}{P} dP \tag{3.9}$$

n_i^o is the equilibrium adsorption capacity for the pure component and P_i^o is the equilibrium gas-phase spreading pressure that corresponds to the spreading pressure of the mixture. The flowchart.3.4 shows the sequence of steps involved in the calculation of the IAS loading. The calculation is done by assuming a total pressure, P and y_i, mole fractions of the components are specified. A solid phase concentration fraction x_i is assumed. The spreading pressure $P^o_{\mathrm{N_2},i}$ and $P^o_{\mathrm{CO_2},i}$ are calculated, and the appropriate equilibrium loading for CO_2 and N_2 are calculated for those pressures using the isotherm model. This is followed by the calculation of the integral of the the Eq.3.9 over the spreading pressures. The integral values for CO_2 and N_2 obtained from Eq.3.9, area A and area B, they are compared, if they fall in the tolerance range the algorithm is stopped and followed for a different total pressure. Else another solid phase concentration fraction is assumed, the sequence is followed till the two integrals are equal.

Fig. 3.3 shows the loading predicted by the extended wDSL isotherm for a binary mixture CO_2/N_2 of 15% and 85%. The same parameters were used as inputs in the IAST based calculation of competitive loading. The predicted extended model and Ideal Adsorbed Solution Theory (IAST) loading are in good agreement with each other. This result validates the use of the extended model to predict competition in the binary CO_2/N_2 system. The compared results are shown for MOF-Fe at 50°C for both IAST as well as extended wDSL isotherm in the Fig.3.3.

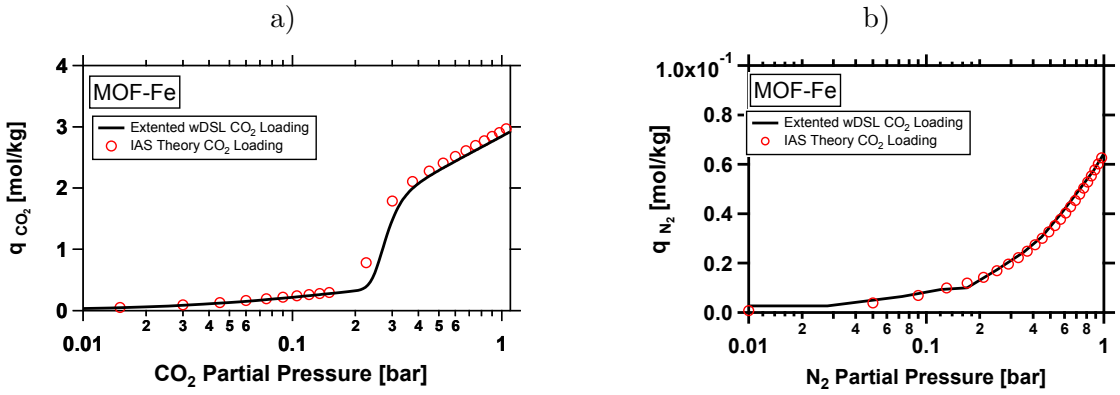

Fig. 3.3: Comparison of the competition a)CO_2 loading and b) N_2 loading obtained from IAS (symbols) and competitive model (line), run for MOF-Fe at 50°C

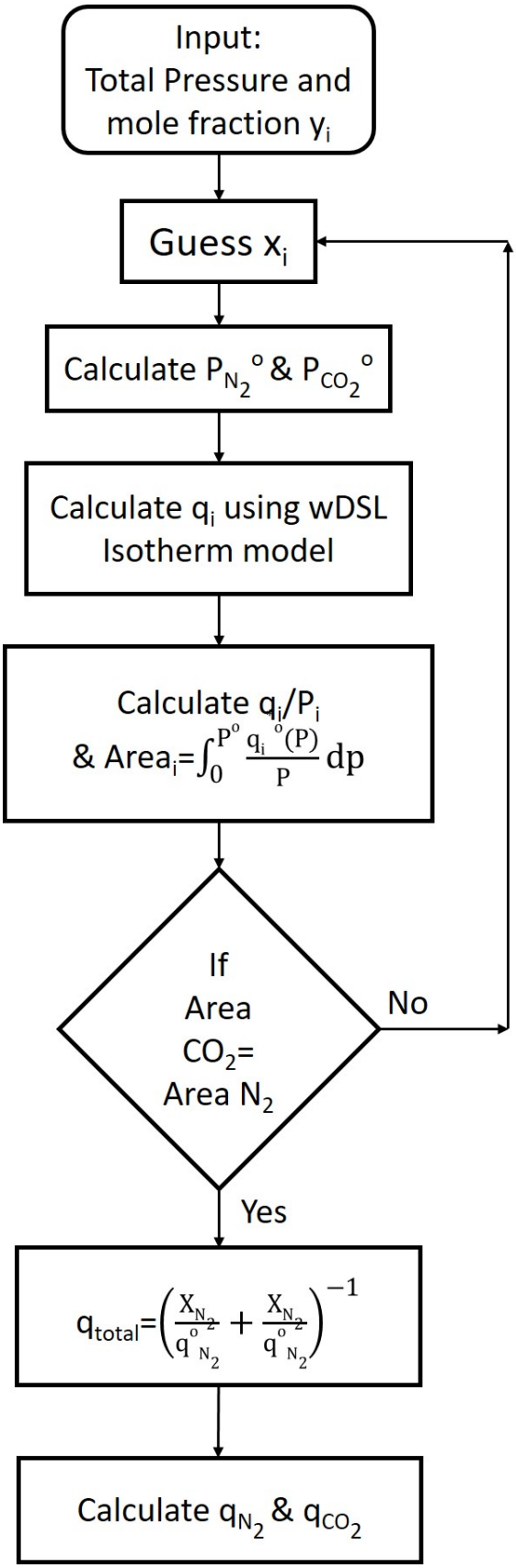

Fig. 3.4: The sequence of steps followed to calculate IAST loading for the various MOF structures

3.3 Process Design and Configuration

3.3.1 Cycle Configuration

The Zeolite 13X used in the simulations are crystals, that were pelletized using a binder. These were experimentally characterized [23]. The MOF structures used in this work are assumed to be binder-less particles, and hence the equilibrium loading in [1, 2] are that of a pure crystal. The density of a pelletized adsorbent would be much lower in the presence of a binder, hence the density of these crystals was assumed to be the same as that of the Zeolite 13X particle. No mass transfer information was available for the MOF materials, and thus the mass transfer was assumed to be macropore controlled. In the absence of certain material properties, the properties of the Zeolite 13X was used for cycle simulations.

In this work, a four step PSA cycle with a light product pressurization (LPP), shown in Fig. 3.5 was chosen for process simulation. This cycle has been shown to have superior performance in separations that deal with the recovery of the heavy product, such as the separation of CO_2 from flue gas [23]. Previous studies have shown that this cycle configuration meets the performance targets for CO_2 purity and recovery, while also having low energy consumption [9].

The cycle configuration consists of the following step:

- Feed/Adsorption (ADS): In this step, the flue gas is fed into the column at feed conditions; feed pressure, P_{H} of 1 bar and feed concentration, 0.15% CO_2. CO_2 has the greater affinity for adsorption on the adsorbent over N_2 which is the weaker component. The light product end, z=L is kept open and N_2 rich product removed at this end at P_{H}.
- Co-current Blowdown (BLO): The feed end of the column is closed and the column is depressurized from feed pressure, P_{H}, to an intermediate pressure, P_{INT}, from the product end. This step removes the N_2 from the column, thereby increasing the purity of CO_2 in the column. Due to depressurization, CO_2 would be lost from the N_2 product end.
- Evacuation (EVAC): Concentrated CO_2 at feed end is removed by reducing the column pressure from intermediate pressure, P_{INT}, to a low pressure, P_{L}. This step also helps reactivate the bed for the next adsorption step.
- Light product pressurization (LPP): In this step, the feed end is closed and the column pressurized in the reverse direction using the light product collected from the adsorption step. At the end of the LPP step, the pressure in the bed brought back up to high pressure, P_{H}. In this step, the CO_2 front that is formed during the preceding step is compressed/ sharpened and pushed to the z=0 end, this improves CO_2 recovery [23]
- Feed pressurization (FP): If the stream from the adsorption step is not sufficient to pressurize the column to the feed pressure, P_{H} in the LPP step, an additional feed pressurization step is introduced to bring the pressure back up to, P_{H}.

The performance indicators for PSA cycles are CO_2 purity, CO_2 recovery, energy consumption of the process, and process productivity. These are given by Eq. 3.10 to 3.13. Purity is the ratio of the moles of CO_2 coming out of the evacuation step to the total number of moles coming out of the evacuation step. Recovery is defined as the ratio of moles of CO_2 in recovered in from the evacuation step to the total number of moles of CO_2 fed into the column, for one cycle. Energy consumption; which is analogous to the operational expense, is defined as the electrical energy equivalent required to capture one tonne of CO_2 from a power plant. A costing analysis would be a complicated undertaking and is avoided in this work since the MOF structures are not commercialized. Productivity which is analogous to the capital expense, is defined as the moles of CO_2 captured by using one m^3 of adsorbent per second, is used as a metric for comparison as it is widely cited in the literature.

$$\text{Purity, Pu}_{\text{CO}_2}[\%] = \frac{\text{Total moles of CO}_2\text{ in extract product in one cycle}}{\text{Total moles of gas in extract product in one cycle}} * 100 \tag{3.10}$$

$$\text{Recovery, Re}_{\text{CO}_2}[\%] = \frac{\text{Total moles of CO}_2\text{ in extract product in one cycle}}{\text{Total moles of CO}_2\text{ fed into the column in one cycle}} * 100 \tag{3.11}$$

$$\text{Energy, En } [\frac{\text{kW} - \text{hr}}{\text{tonne CO}_2\text{ captured}}] = \frac{\text{E}_{\text{ADS}} + \text{E}_{\text{BLO}} + \text{E}_{\text{EVAC}} + \text{E}_{\text{FP}}}{\text{Mass of CO}_2\text{ in the extract product per cycle}} \tag{3.12}$$

$$\text{Productivity, Pr } [\frac{\text{mol}_{\text{CO}_2}}{\text{m}^3\text{ adsorbent s}}] = \frac{\text{Total moles of CO}_2\text{ in the extract product}}{(\text{ Total volume of adsorbent }) (\text{Cycle time })} \tag{3.13}$$

The energy consumption of the different steps of the cycle are calculated as a basis of their initial and final pressure. A detailed physical description is given below:

- Adsorption step: If $P_{\text{H}} = P_{\text{feed}}$, then energy is required only to overcome the frictional pressure drop in the column. If $P_{\text{H}} > P_{\text{feed}}$, then energy is required to compress the feed gas from P_{feed} to P_{H}. In the case of a VSA process, $\text{P}_{\text{feed}} = \text{P}_{\text{H}}$, which is equal to 1 bar.
- Co-Blowdown step: Co-Blowdown step may be performed at any pressure between P_{H} and P_{L}. The pressure decreases from P_{H} to P_{INT} in this step. If $\text{P}_{\text{INT}} > 1$ bar, then the Co-blowdown step does not require any energy. However, if $\text{P}_{\text{INT}} < 1$ bar, then energy is required only to evacuate from 1 bar to P_{INT} using a vacuum pump.
- Evacuation step: If $\text{P}_{\text{INT}} > 1$ bar, then energy is required only to evacuate from 1 bar to P_{L}. If $\text{P}_{\text{INT}} < 1$ bar, then energy is required to evacuate fromP_{INT} and P_{L} using a vacuum pump.

$$\text{E}_{\text{Step}} = \frac{1}{\eta}\epsilon\pi r_{\text{in}}^2 \frac{\gamma}{\gamma - 1} \int_{t=0}^{t=t_{Step}} (vP_{out}) \left[(\frac{1}{P_{out}})^{\frac{\gamma - 1}{\gamma}} - 1 \right] dt \tag{3.14}$$

The energy consumption of the cycle is taken as the ratio of the sum of the energy for all of the steps to the mass of CO_2 extracted from the evacuation step per cycle, this is given in Eq. 3.12. This is done as a way to visualize the energy penalty incurred due to the capture process. In order to convert the mass unit to tons, the appropriate conversion factors are applied. In these equations, η represents the efficiency of the vacuum pumps, which is assumed to be 74%. The symbol γ represents the adiabatic constant and is assumed to have a value of 1.4.

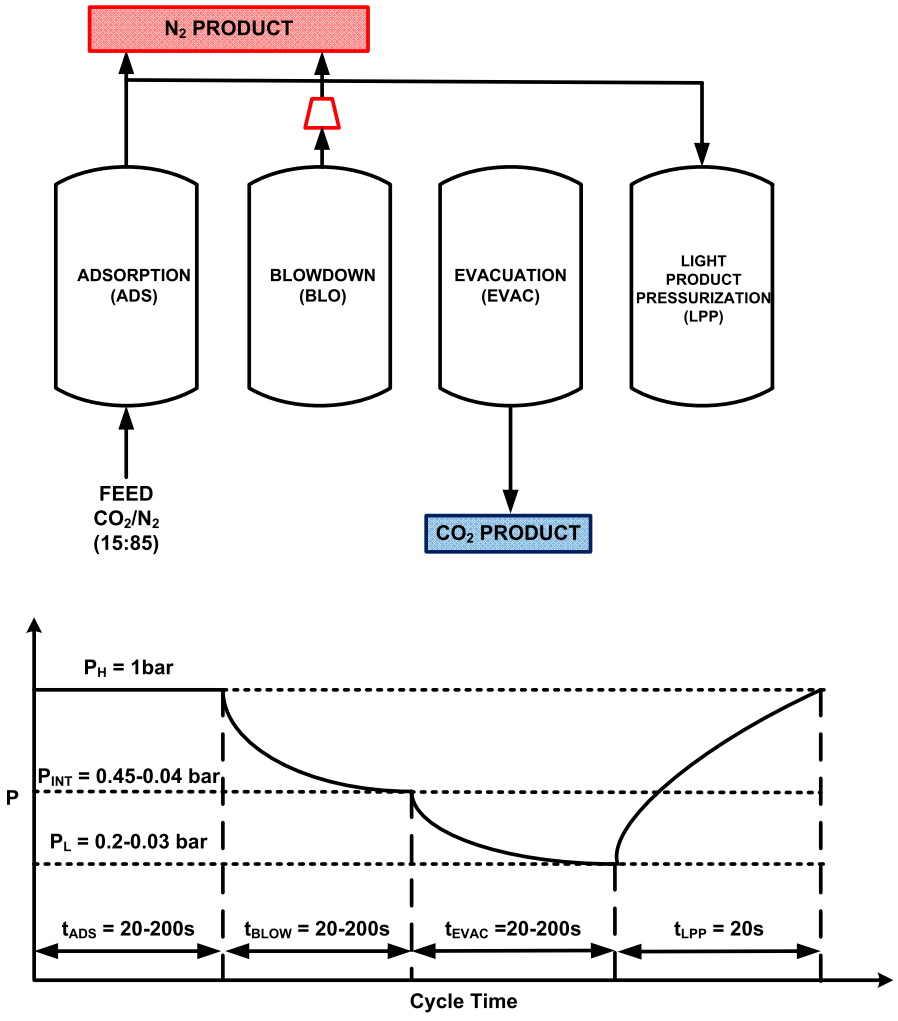

Fig. 3.5: Four step Vacuum Swing Adsorption (VSA) cycle with adsorption (ADS), co-current blowdown (BLO) and counter-current evacuation (EVAC) and light product pressurization (LPP) steps

Parameter		Value	
Column Length	L	1	[m]
Inner column radius	r_{in}	0.1445	[m]
Outer column radius	r_{out}	0.1620	[m]
Column void fraction	ε	0.39	[-]
Particle voidage	ε_{p}	0.35	[-]
Particle radius	r_{p}	1.50×10^{-03}	[m]
Tortuosity	τ'	3	[-]
Column wall density	ρ_{s}	7800	[kg/m^3]
Specific heat capacity of gas phase	$C_{\text{p,g}}$	41.66	[$\text{J mol}^{-1}\,\text{K}^{-1}$]
Specific heat capacity of adsorbed phase	$C_{\text{p,a}}$	40.02	[$\text{J mol}^{-1}\,\text{K}^{-1}$]
Specific heat capacity of adsorbent phase	$C_{\text{p,s}}$	1070	[$\text{J kg}^{-1}\,\text{K}^{-1}$]
Specific heat capacity of column wall	$C_{\text{p,w}}$	502	[$\text{J kg}^{-1}\,\text{K}^{-1}$]
Fluid viscosity	μ	1.317×10^{-05}	[$\text{kg m}^{-1}\,\text{s}^{-1}$]
Molecular diffusivity	D_{m}	1.53×10^{-05}	[$\text{m}^2\,\text{s}^{-1}$]
Adiabatic constant	γ	1.4	[-]
Effective gas thermal conductivity	K_{z}	4.38×10^{-02}	[$\text{J m}^{-1}\,\text{K}^{-1}\,\text{s}^{-1}$]
Thermal conductivity of column wall	K_{w}	16	[$\text{J m}^{-1}\,\text{K}^{-1}\,\text{s}^{-1}$]
Inside heat transfer coefficient	h_{in}	8.6	[$\text{J m}^{-2}\,\text{K}^{-1}\,\text{s}^{-1}$]
Outside heat transfer coefficient	h_{out}	2.5	[$\text{J m}^{-2}\,\text{K}^{-1}\,\text{s}^{-1}$]
Universal gas constant	R	8.314	[$\text{m}^3\,\text{Pa mol}^{-1}\,\text{K}^{-1}$]
Ambient Temperature	T_{a}	298.15	[K]

Table 3.2: Parameters used in the process simulation

3.4 Results and Discussion

3.4.1 Process Simulations

It has been shown in previous studies, that for adsorption-based post-combustion CO_2 capture process, pressurization of the feed pressure, P_{feed}, to values greater than a high pressure, P_{H} of 1 bar is detrimental to the energy consumed [9]. This reduces the Pressure Vacuum Swing Adsorption (PVSA) process to a Vacuum Swing Adsorption (VSA) process. The low pressure of 0.03 bar is fixed, due to the inability of large vacuum pumps to achieve lower pressure in large scale industrial

conditions. The VSA process thus operates between the pressure range 0.03 bar to 1 bar. Therefore a CO_2 partial pressure at feed conditions is 0.15 bar.

All the MOF structures show capacity for CO_2 in this range of operating conditions, at vastly different temperature range. The isotherms in the Fig. 3.2 shows, all of the MOFs have the inflection point occurring at a partial pressure of 0.15 bar while still having a large capacity for CO_2, at feed temperature in the range of 20-120°C. However, the flue gas temperatures in a typical coal based power plant are in the range of 50 to 70°C. A material that shows inflection in this range should be chosen for process simulations. From the set of MOF structures available, MOF-Mn shows these properties, thus it was chosen for process simulation.

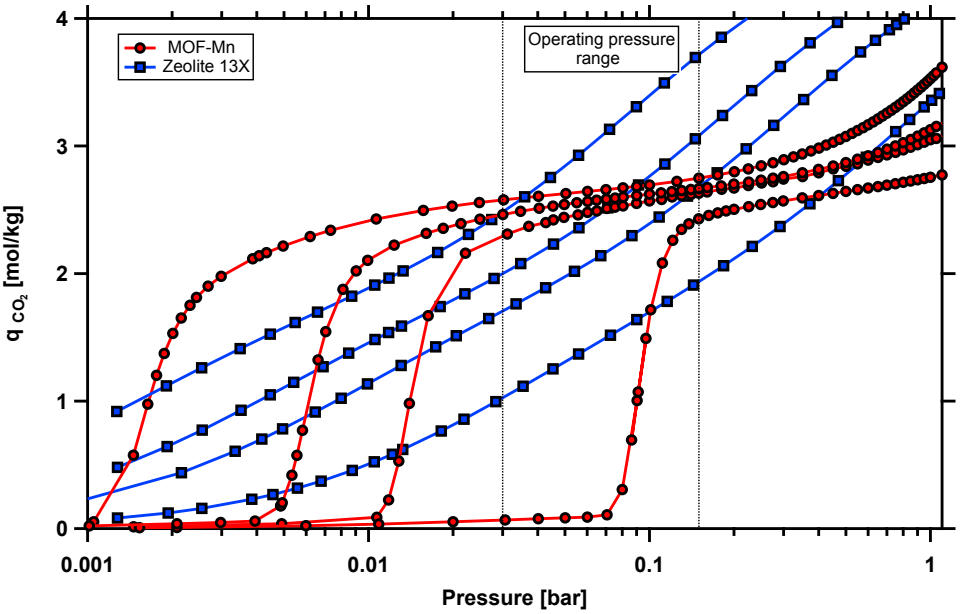

Fig. 3.6: Comparison of Zeolite 13X (squares) at 25°C and MOF-Mn (circles) isotherm at 25, 40, 50, 75°C.

A comparison of CO_2 isotherms of MOF-Mn and Zeolite 13X is shown in the Fig. 3.6. As seen above, Zeolite 13X has a higher CO_2 capacity then MOF-Mn, which is approximately 3.5 mol/kg to 2.5 mol/kg. One feature of the isotherm clearly stands out is, the inflection on the CO_2 isotherm. The MOF-Mn isotherm appears as if it's moving up the axis towards higher pressures as temperature increases. This would affect its performance in a process, since the temperature inside a VSA bed changes dynamically. The best temperature to operate the process is, therefore, an unknown. To understand the effect of feed temperature on the performance of the two adsorbents, a parametric analysis was carried out by varying T_{feed}, from 25°C to 75°C in intervals of 5°C. The other main operating conditions are given in Table 3.3.

t_{ADS} [s]	t_{BLO} [s]	t_{EVAC} [s]	P_{INT} [bar]	P_L [bar]	T_{feed} [$^\circ C$]	v_{feed} [m/s]
30	30	30	0.1	0.03	25-75	1

Table 3.3: Operating conditions for the four-step VSA process with T_{feed} varying from 25°C to 75°C in intervals of 5°C

Figure 3.7 shows the variation of purity and recovery values for the two adsorbents being studied for different feed temperatures, T_{feed}, while the other operating conditions are kept constant. It can be seen that Zeolite 13X is not affected by the change in temperature of the feed. But the MOF-Mn performance is deeply impacted by the change is feed temperature. An important observation can made, regarding the performance of the MOF-Mn: the purity of CO_2 decreases with increase in temperature and has a minima occur in between 60 to 70°C. An opposite trend can be seen for recovery, as the temperature of the feed increases the recovery of CO_2 increases and reaches a maxima in-between the temperatures of 60 to 70°C.

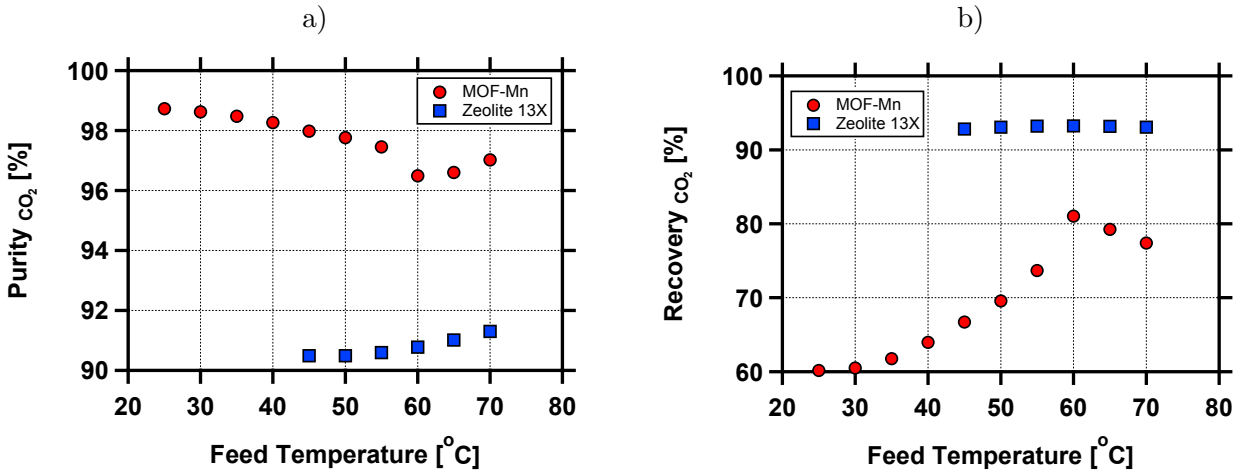

Fig. 3.7: Effect of the feed temperature on a) CO_2 purity and b)CO_2 recovery a)Shows the variation of purity as a function of T_{feed}, MOF-Mn (circles) and Zeolite 13X (squares) b)Shows the variation of recovery as a function of T_{feed}, MOF-Mn (circles) and Zeolite 13X (squares)

To understand this variation in purity and recovery for the different temperatures and pressures, the gas phase concentrations of CO_2 and N_2 was investigated. Fig.3.8 shows the variation of the gas phase concentrations of a) CO_2 and b) N_2 for the different feed temperatures studied. This was obtained from plotting the gas phase concentration profiles, from the above-mentioned points, at CSS for the end of the adsorption step. As we can observe, there is an unusual front that occurs in the concentration profile of CO_2 at a feed temperature around of 60°C. This effect continues to reduce till 70°C. It was seen from Fig. 3.7, the corresponding CO_2 recoveries also increase and then

start decreasing in a similar fashion. This is due to the presence of the inflection point on the CO_2 isotherm that occurs at 0.03 bar low pressure. The presence of which increases the CO_2 capacity and forms an unusual CO_2 front. Hence there is less CO_2 lost in the adsorption step. This explains the increase in CO_2 recovery.

The CO_2 purity decrease can be similarly explained by Fig.3.8 b), where the N_2 concentration is plotted at CSS at the end of the adsorption step. As the N_2 concentration moves closer towards the z=0 end, the purity of the CO_2 product reduces. At lower temperatures, the N_2 front is pushed out of the column by the CO_2 front. But as the capacity of CO_2 increases with the presence of the inflection point, the CO_2 front sharpens and is now closer to z=0 end. The corresponding N_2 front also moves closer to the z=0 end. The fact that the N_2 front has not been pushed out of the bed completely in the adsorption step causes a decrease in purity of CO_2 product, at the temperature range of 65°C to 75°C. This is an interesting observation, as this does not occur in the case of Zeolite 13X. In a type 1 isotherm, the adsorption is generally a shock front and the desorption is a simple wave.

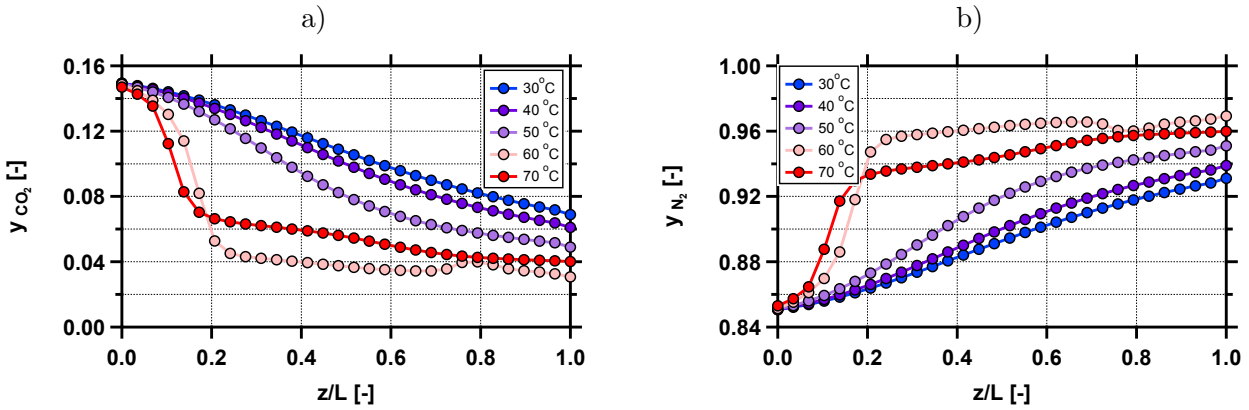

Fig. 3.8: The axial profile of a) CO_2 gas phase composition and b) gas phase composition of N_2 for various feed temperatures, operating conditions are given in Table 3.3

The concentration in the bed varies unusually with feed temperature for the MOF-Mn. This is due to the shape of the CO_2 isotherm. To understand the variation of profiles as they do at varying temperatures inside the column, we must look at the fundamentals of the adsorption. Between temperatures 55 to 70 °C, a distinct inflection point occurs. This leads to the formation of a "multipart transition", which is nothing but a combination of shock and wave fronts [54, 55] inside the bed. This effect can be highlighted by looking at the variation of concentration at the outlet of the column. In Fig.3.9 the variation of the outlet concentration is shown for a general type 1 case along with an S-Shape case. There is a distinct difference in the two profiles. The shape of this plot can have five different transitions.

- a shock transition (S)

- a wave transition (W)
- a shock-wave transition (SW)
- a wave-shock transition (WS)
- a shock-wave-shock transition (SWS)

Let us consider two isotherms, a type 1 isotherm, and an S-Shape isotherm. The Fig. 3.9 shows, a step transition between the initial and the feed state and then back to the initial state, i.e. adsorption and desorption. Figure. 3.9 shows this transition for a type 1 isotherm, as traveling from point i to point f, the corresponding outlet concentration is generally a shock transition. The time taken for the shock to propagate through the column is the breakthrough time. But in the presence of an inflection point, as is the case with the S-Shape isotherm, there are two points a and b. These points corresponding to the inflection point on the isotherm. The single shock form is replaced by a shock-wave-shock transition, as seen in the Fig. 3.9 b). The translation of this can be seen as a shock that corresponds to transition between point i to inflection point a, and a wave that corresponds to a concentration change from a to b. Followed by a shock transition from point b to point f. When the concentrations are lowered in the bed, i.e. desorption, an opposite trend can be seen. For a type 1 isotherm, the concentration change is a simple wave. But for an S-Shape isotherm, a combination of two shorter waves with a shock transition in between is seen. This multipart transition is what causes the unusual fronts in the bed at between 50°C to 70°C. The formation of these plateaus can pose a challenge with regards to cycle design and optimization.

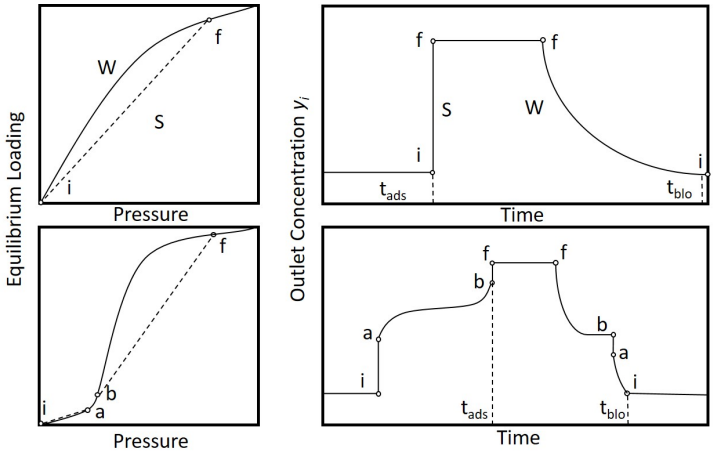

Fig. 3.9: Illustrative breakthrough profiles for initial and feed concentrations resulting in the formation of a shock transition (top) and in the formation of a shock-wave-shock transition (bottom). The duration of the adsorption step is indicated by t_{ADS}, i.e., the time required for the column to be fully saturated. (adapted from Hefti *et.al.* [12])

3.4.2 Maximization of Purity and Recovery

In a post combustion CO_2, the inlet stream to the capture process consists of only 15 mol% CO_2, with the rest, assumed to be N_2. The US. Dept of Energy (DOE) has set the purity and recovery targets for CO_2 capture to be >95% and >90%, respectively [46, 47]. To increase the concentration of the stream to 95%, while capturing >90% of the CO_2 feed, is a very challenging task. Optimization of these performance indicators are thus necessary, due to the many degrees of freedom in a VSA unit, optimization of the process becomes non-trivial and very challenging. The optimization is multi-objective optimization performed with a set multi-variable, where the objectives are minimized simultaneously.In the optimization, the presence of local minima is a very real possibility and avoiding these during optimization is important to obtain the best process conditions. In this study, the Non-Sorting Genetic Algorithm (NSGA) from the MATLAB global optimization toolbox was chosen. This was used because the GA has been shown to be very adept at avoiding local minima. Since GA based optimization is stochastic in nature, a global minimum is not always guaranteed. A brief introduction of the GA; the optimization algorithm, used in this work are provided in chapter 2. To maximize the purity and recovery of the CO_2 product, two functions J_1 and J_2 were defined as shown below. These values are the reciprocal of the purity and recovery of CO_2 and counter each other. The GA minimizes the two functions for a range of decision variables and thus a Pareto curve of the best purity and recovery points are generated. The minimizing functions for each of the optimization cases are stated as Eqs. 3.15 to 3.16. A random sample population size of 144 was created for each of the decision variables. It was created using a latin hypercube sampling technique to ensure an even spread in all regions for all the decision variables. This was used as an initial population and the optimization was run for 25 generations.

$$J_1 = \frac{1}{Pu_{\mathrm{CO_2}}} \tag{3.15}$$

$$J_2 = \frac{1}{Re_{\mathrm{CO_2}}} \tag{3.16}$$

In the earlier section, the results showed the variation of purity and recovery of the CO_2 for a set of operating parameters. In order to best gauge the performance of the MOF-Mn and Zeolite 13X, a set of purity recovery optimization simulations were performed. The four step cycle with LPP has seven operating parameters, namely, the duration of the four steps, t_{ADS}, t_{BLO}, t_{EVAC}, t_{LPP}, the two operating pressures, P_{INT}, P_{L}, and the inlet feed velocity, $\mathrm{v_{FEED}}$ in the adsorption step. Of these, the duration of the LPP step is determined by the time taken for the light product stream to bring the pressure up to P_{H}, hence is not a decision variable. The remaining six parameters are used as the main decision variables for optimization of the cycle under study.

Effect of Variation of T_{feed} on the Purity and Recovery of CO_2

Unlike in the case of Zeolite 13X, the feed temperature has an enormous impact in the performance of the MOF-Mn. The best performance in the parametric study was for temperatures ranging from 50°C to 70°C, with high purity values obtained at a temperature closer to 50°C and high recovery values obtained at a temperature closer to 70°C. To determine the best feed temperature to operate the process, a multi-objective optimization to maximize of purity and recovery was performed. This was done for three different inlet feed temperatures, T_{feed} = 50°C, 60°C, 70°C. The purity and recovery values were compiled and the best points were filtered. The resulting Pareto points represent the best trade-off between purity-recovery for the material for the corresponding feed temperatures. The area beyond this curve represents performance that cannot be achieved for the feed temperature. The area below the curve represents sub-optimal points to operate the process. From Fig. 3.10 it is not clear if any one temperature shows better performance over the others.

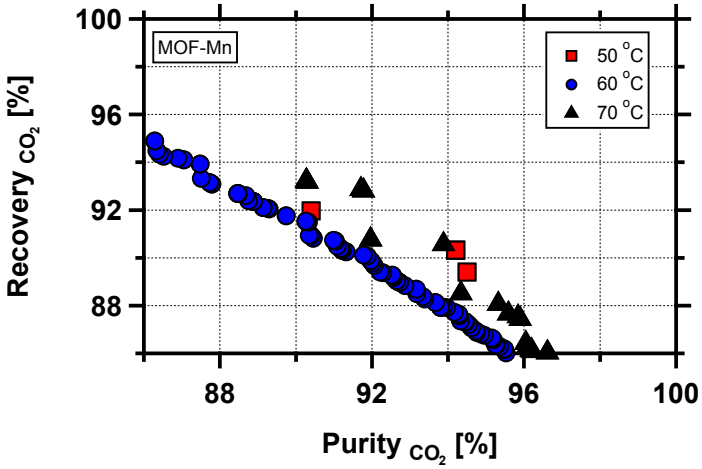

Fig. 3.10: Pareto curves that are the result of process optimization to maximize CO_2 purity and recovery for 4-step cycle with LPP, each case was generated by changing the feed temperature, T_{feed} to the value provided in the legend

Upon analysis of the variation of the decision variables of the Pareto points, it was noticed that as feed temperature increases, from 50°C to 60°C, the decision variable, P_L was around the lower bound of 0.03 bar. This is not unusual as this is a unconstraint optimization. The low pressure P_L, invariably tends to group around its lower bound. This is due to the fact that, the best points tend to occur at the largest pressure swing. Since the low pressure P_L, is bound to a lower limit of 0.03 bar, the P_L would group around that figure. This fact has been highlighted various times in the literature [9, 11, 23]. This can be observed in Fig 3.10, where the variation of the low pressure, P_L, is plotted against the purity of CO_2 for the Pareto points. But when the feed temperature was increased from 60°C to 70°C, there was an increase in the low pressure, and it settled at 0.038 bar. This is unusual and indicates a relation between the P_L, and the feed temperature where inflection

occurs.

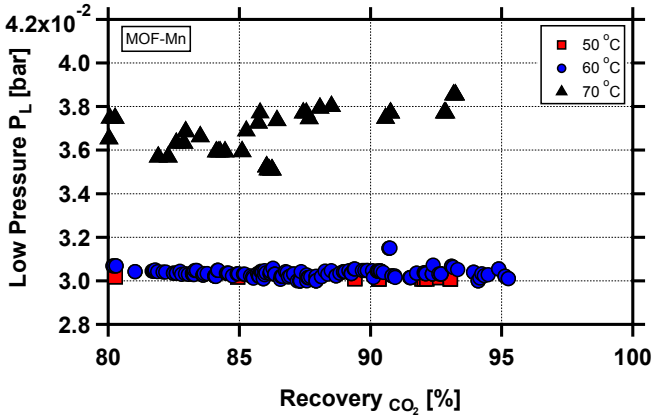

Fig. 3.11: The decision variable, P_{L} for the points corresponding to the Pareto curves from Fig.3.10, that are the result of process optimization to maximize CO_2 purity and recovery for 4-step cycle with LPP, each case was generated by changing the feed temperature, T_{feed} to the value provided in the legend

Effect of Variation of $\mathbf{P_L}$ on the Purity and Recovery of $\mathbf{CO_2}$

The link between the feed temperature, T_{feed}, and the low pressure, P_{L}, due to the inflection point is examined in this section. Another batch of optimizations were run, to maximize the purity and recovery of CO_2. In this the low pressure, P_{L} was set at 0.1 bar, 0.08 bar, 0.05 bar, 0.03 bar. In each of these optimization the inlet feed temperature, T_{feed} was a decision variable in addition to the others. Fig. 3.12 shows the resulting Pareto curves for each of the cases low pressure, P_{L} of varied. As expected the lowest pressure, P_{L} =0.03 bar showed the best the performance. While P_{L} =0.1 bar showed the worst performance.

The decision variables for the Pareto points optimizations were analyzed. Each of the curves represents the best possible purity and recovery that is possible for the set low pressure. The purity values for these points were plotted against feed temperature, T_{feed}. The resulting Fig. 3.13 a) shows the variable, T_{feed}, tends to group in a range of temperatures where the inflection point occurs. This is due to the fact that, for each of the following cases the low pressure is fixed. The relation between the two design parameters are clear. For a set low pressure, the best performance is obtained at a feed temperature at were the inflection corresponds to the same low pressure. This relation can now be exploited to achieve better results at higher pressures of P_{L}. This means the process can be tailored to run at higher low pressures by just operating the process at higher temperatures. It is also worth mentioning that this material achieves a purity-recovery of 90% at P_{L} as high as 0.05 bar, which is higher that Zeolite 13X, shown in the literature [56].

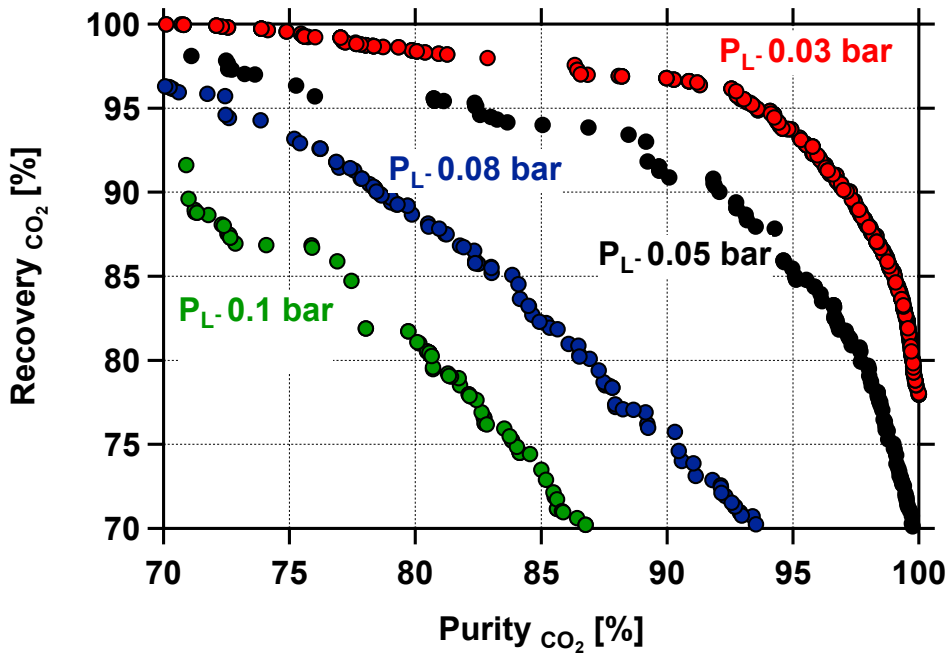

Fig. 3.12: Pareto curves that are the result of process optimization to maximize CO_2 purity and recovery for the 4-step cycle with LPP, each case was generated by changing the P_L to the value provided in the legend

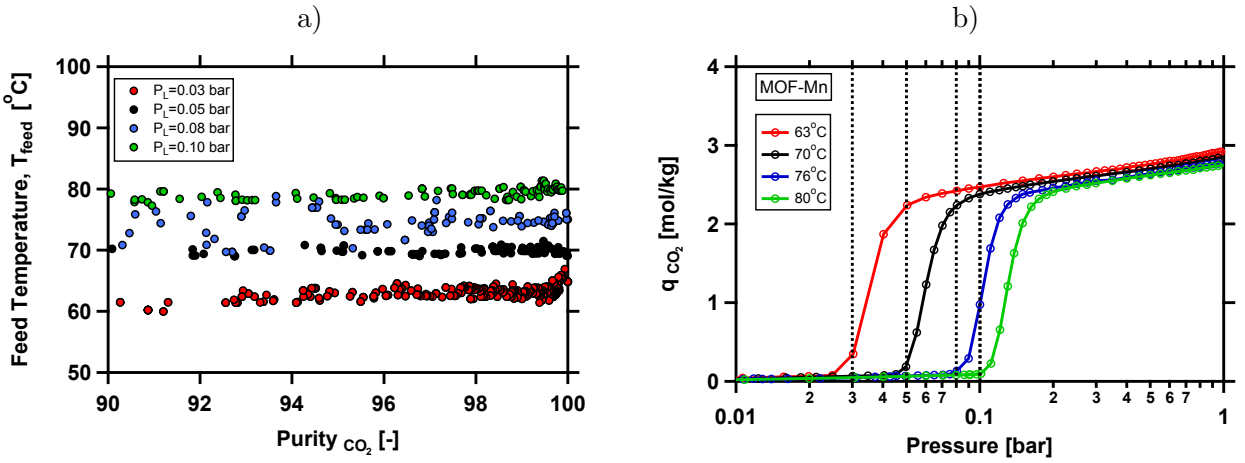

Fig. 3.13: Pareto curve points from Fig.3.12 a) The purity values in each cases of P_L is plotted against T_{feed} b) The optimized temperature of each of the P_L cases on the isotherm plot

Optimization with T_{feed} and P_L as decision variable

It was established in the earlier sections that, T_{feed} and P_L, are inherently linked due to the shape of the MOF-Mn CO_2 isotherm. To find the best performance of the material being optimized, both T_{feed} and P_L, are to be included as optimization variables. An optimization to maximize purity

recovery with the usual six decision variables t_{ADS}, t_{BLO}, t_{EVAC}, P_{INT}, P_{L}, v_{feed} and in addition to this feed temperature T_{feed} was a decision variable, was run. The resulting Pareto front is shown in Fig. 3.14, the region was sub divided into different temperature ranges. This shows an increase in performance from 25°C to 70°C, then reduces from 70°C to 120°C. A conclusion can be made that the best performance is obtained while operating the process at a feed temperature T_{feed} corresponding to the temperature at which the inflection point occurs at the lowest pressure in the process.

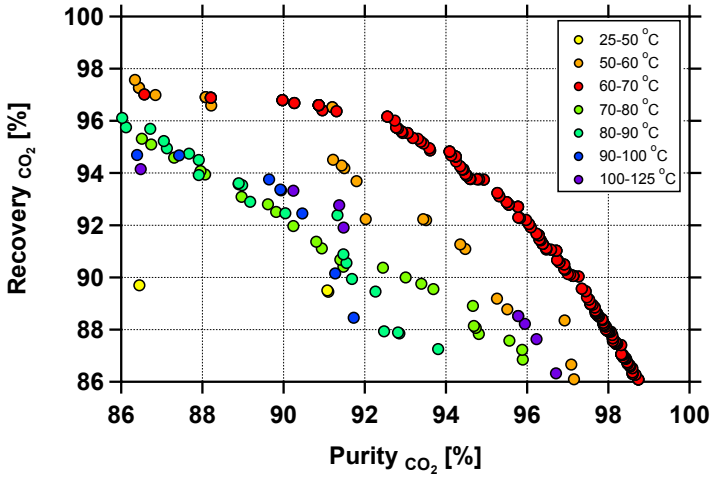

Fig. 3.14: Pareto front for the optimization of purity and recovery of CO_2 for different temperature regions (shown in the legend), with $_{\mathrm{ADS}}$, t_{BLO}, t_{EVAC}, P_{INT}, P_{L}, v_{feed} and T_{feed} as decision variables

Material Ranking Based on Purity-Recovery

The ranking the MOFs on the best purity recovery does not provide information on process advantages but can be used as a filter to weed out the materials that do not satisfy the DOE targets. To rank the MOFs and compare them to Zeolite 13X, an optimization was run with t_{ADS}, t_{BLO}, t_{EVAC}, P_{INT}, P_{L}, v_{feed}, T_{feed} as the decision variables. The range for each of the bounds is given in the Table. 3.4, and the range of T_{feed} is shown in the Fig.3.15. This range of temperatures were picked based on the position of the inflection point, and if it occurs in-between the operating pressure range of 0.03 bar to 0.15 bar. The results of the optimization of the six materials is shown in the Fig.3.16. It is observed that of the five MOFs being compared on their purity-recovery performance MOF-Co was the least favorable, followed by MOF-Zn and MOF-Fe which does not have any discernible difference between the two. Of the three materials that satisfied the 95% purity 90% recovery target MOF-Mg, MOF-Mn, Zeolite 13X, the performance of MOF-Mn and MOF-Mg was better than that of the Zeolite 13X. In the case of MOF-Mn and MOF-Mg their performance was almost identical to each other in terms of the purity recovery of CO_2.

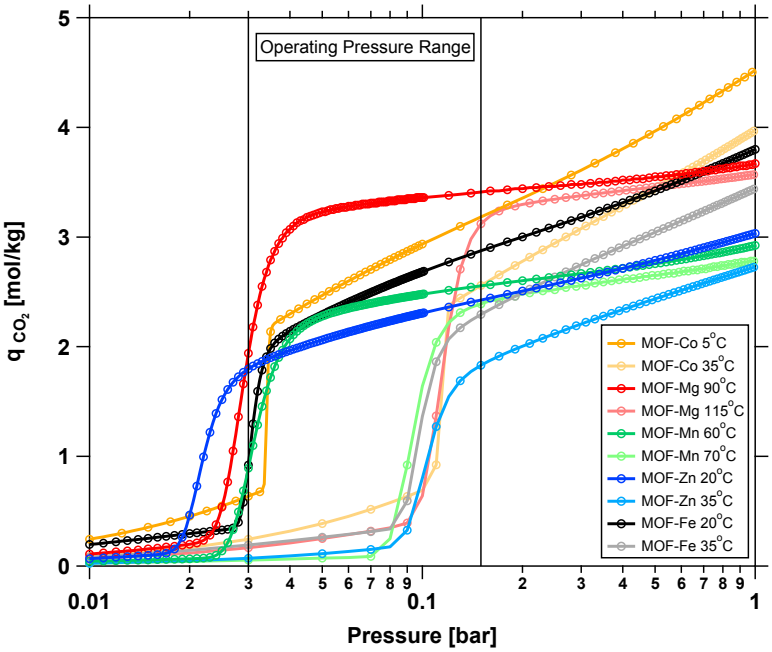

Fig. 3.15: The temperature range for all the MOF materials that fit in the operating range used as a bound for the process optimization decision variable to maximize CO_2 purity and recovery for 4-step cycle with LPP cycle

t_{ADS} [s]	t_{BLO} [s]	t_{EVAC} [s]	P_{INT} [bar]	P_L [bar]	v_{feed} $[m/s]$
20-200	20-200	20-200	0.04-0.45	0.03-0.3	0.1-2

Table 3.4: Lower and upper bounds for decision variables in the optimization problem of four-Step VSA Cycle

Further study is required to say for certain if the shape of the S-Shape has an effect on the performance achieved. The feed temperature being a decision variable for all the MOFs had different values for each of the optimization, MOF-Co, MOF-Zn and MOF-Fe both had an optimized T_{feed} range of 15-25°C. For MOF-Mg the inflection point that corresponds to the evacuation pressure is at a very high temperature of 90-100 °C. MOF-Mn, on the other hand, had an optimized feed temperature of 60-65°C. It was assumed for the sake of simplicity that this difference in feed temperatures needed to be accounted for upstream of the capture unit. The typical flue gas temperature for post combustion CO_2 falls in the range of 55 to 65°C, which is similar to the T_{feed} that was optimized for MOF-Mn.

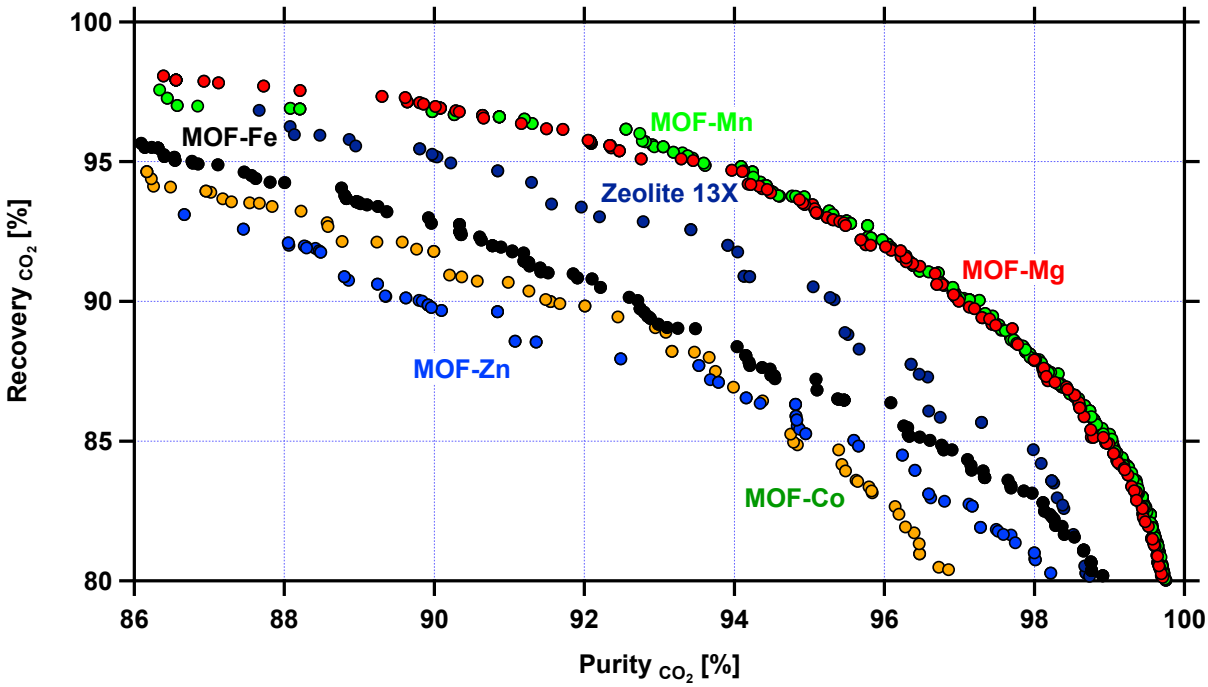

Fig. 3.16: The Pareto points for process optimization to maximize CO_2 purity and recovery for MOF-Xs and Zeolite 13X in the 4 step VSA cycle with LPP, the materials provided in the legend, the optimization was performed with t_{ADS}, t_{BLO}, t_{EVAC}, P_{INT}, P_{L}, v_{feed} and T_{feed} as decision variables

3.4.3 Minimization of Energy and Maximization of Productivity

The previous section dealt with ranking of the MOF structures based on their purity and recovery of CO_2. This ranking while giving us a general ability of the material to achieve a certain performance of purity and recovery. i.e., DOE targets. For the implementation of a PSA based process, it is also important to provide information such as the operation and capital costs involved. In literature this is referred to as productivity and energy consumption, which are analogous to capital and operational cost respectively. The representation of these values as capital and operating expenses is avoided in this work as they involve more complex costing analysis. Accordingly, the following objective functions were chosen:

$$\mathrm{J}_3 = \frac{\mathrm{Energy}}{165} + 10000(\max[0, \mathrm{TolPu} - \mathrm{Pu}])^2 + 10000(\max[0, \mathrm{TolRe} - \mathrm{Re}])^2 \tag{3.17}$$

$$\mathrm{J}_4 = \frac{1}{\mathrm{Productivity}} + 10000(\max[0, \mathrm{TolPu} - \mathrm{Pu}])^2 + 10000(\max[0, \mathrm{TolRe} - \mathrm{Re}])^2 \tag{3.18}$$

The TolPu and TolRe in J_3 and J_4 represent the purity and recovery constraint forced on the optimization. In this system they are 95% and 90%, respectively. It should be understood that

for a given set of materials, the one that provides the best productivity for the lowest energy consumption is considered the better material for the process. This values however only make sense if the purity, as well as recovery target, are met for the points. From Fig.3.16 it is clear that of the MOF structures only MOF-Mg and MOF-Mn make the cut, in terms of purity and recovery targets. The rest of the materials were not considered for the optimization study. The Eq.3.17 to 3.18 are used to minimize the energy of the process whilst maximizing the productivity for a given purity and recovery target for CO_2. Taking the points that satisfy the constraints of 95% Purity and 90% recovery as initial seeds an energy and productivity optimization was carried out. The operating points from the earlier purity and recovery optimization runs were used as initial seed points for the optimization in this section. The decision variables and the ranges used in this optimization are given in Table.3.4.

The optimization performed has a constraint on the purity and recovery achieved by the process. They are set to the DOE targets of 95% purity and 90% recovery of CO_2. The results are tabulated and the best points are plotted on an energy vs productivity plot. The best region is the bottom right corner, were the productivity is high and the energy consumption is low. The results of which are shown in Fig. 3.17, an advantage is seen in the productivity of the MOF-Mn when compared to the Zeolite 13X which has a stronger CO_2 loading. It also outperforms the Zeolite 13X on the energy consumption with an almost 20 percent lower parasitic energy.

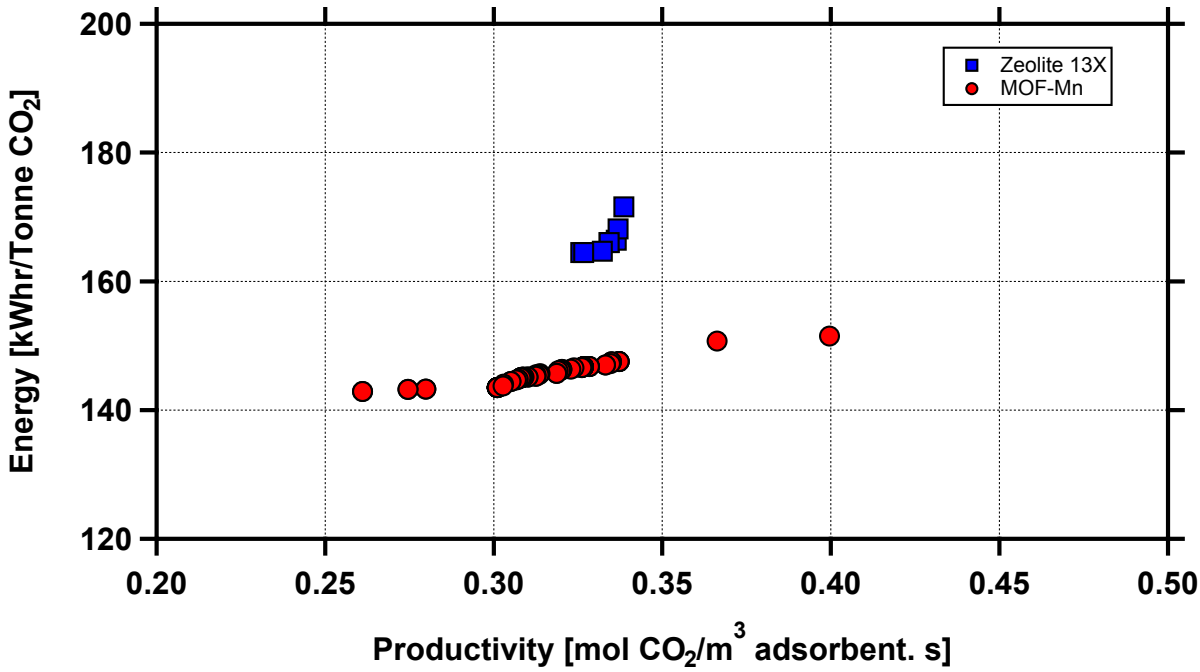

Fig. 3.17: Pareto curve for the maximization of productivity and minimization of Energy. Constraints were imposed on CO_2 purity >95% and recovery >90% run with t_{ADS}, t_{BLO}, t_{EVAC}, P_{INT}, P_L, v_{feed}, T_{feed} as the decision variables

Effect of Decision Variable, P_{INT}, on the Energy Consumption

An advantage for energy consumption can be seen for the MOF-Mn over Zeolite 13X from Fig.3.17. The result of low parasitic energy is not a function of the shape of the isotherm, and it is predominantly due to the low N_2 affinity of the material. To understand this, a plot of the key decision variable, P_{INT} was made as a function of CO_2 purity for the points that satisfy 90% recovery of CO_2. From the Fig. 3.18 it can be seen, that for MOF-Mn high purity of 95% can be achieved at intermediate pressure, P_{INT}, of 0.12 bar. This is much higher than that for Zeolite 13X, which is 0.06 bar. The presence of a smaller amount of adsorbed N_2 leads to the blowdown step pressure P_{INT} to be much higher than in the case of Zeolite 13X. To highlight this phenomenon further, a plot of the energy expenditures of the different steps were plotted for both MOF-Mn and Zeolite 13X in Fig. 3.19. It can be clearly seen that the lower energy is due to the fact that, the energy used in the blowdown step is much lower for the MOF-Mn over that of the Zeolite 13X. The other steps; adsorption and evacuation, have similar comparable energy values. Thus the better performance in the case of the MOF-Mn is possible due to a lower affinity for N_2 on the diamine appended MOFs.

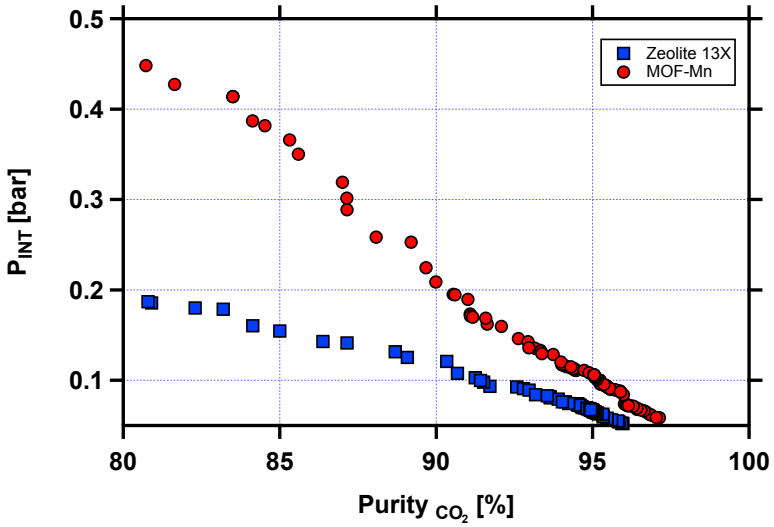

Fig. 3.18: Plot of the variation in P_{INT} as a function of CO_2 purity for the points that satisfy 90% recovery for Zeolite 13X (squares) and MOF-Mn (circles), the points are from the optimization performed to minimize energy and maximize productivity

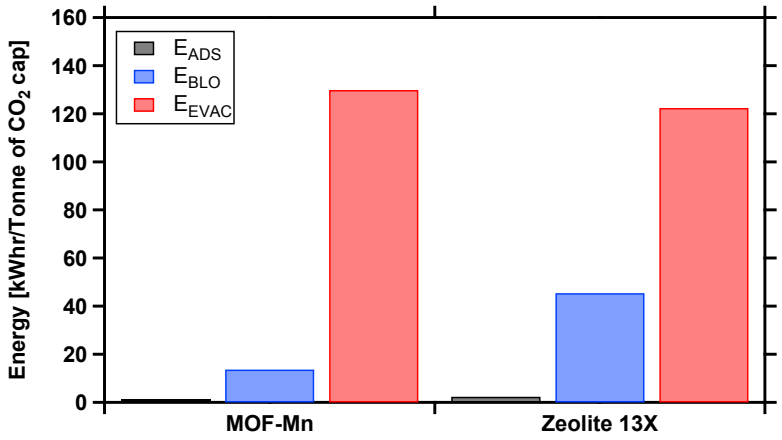

Fig. 3.19: Plot of the energy expenditure in the different steps for the lowest energy point for Zeolite 13X and MOF-Mn, the points are from the optimization performed to minimize energy and maximize productivity

3.5 Conclusion

The adsorption equilibria of the S-Shape diamine appended MOFs were fitted to a concentration based wDSL isotherm. Since this isotherm model was a function of temperature and pressure, it allowed for the simulation of the process to be performed in non-isothermal conditions. The process was simulated with the wDSL model in an in-house process simulation code. A four step cycle with LPP, was used for simulation studies. In the study, a key relation was found between the P_{L} and T_{feed}. This feature investigated using various optimization, which were performed using a genetic algorithm based optimization technique. It was determined, the best performance of the S-Shape materials was obtained when the feed temperature, which aligned with the inflection point at the P_{L}. The performance of the diamine-appended metal-organic framework adsorbents, MOF-Xs, were also compared to that of Zeolite 13X. It was found that in terms of purity and recovery, both Zeolite 13X performed better then MOF-Fe, Co, Zn but MOF-Mn and MOF-Mg performed the best. In order to draw a fair comparison between the MOF structures and Zeolite 13X in a full scale process, an optimization was performed to minimize energy and maximize productivity. This analysis revealed that MOF-Mn could achieve 95% purity and 90% recovery at a minimum energy of 140 kWhr/tonneCO_2cap, compared to Zeolite 13X at 170 kWhr/tonneCO_2cap. This was because the blowdown pressure of MOF-Mn settled at 0.11 bar, compared to 13X at 0.06 bar. This was found to be due to the lower capacity for N_2 in MOFs when compared to Zeolite 13X. The productivity values for both the materials were comparable, with the MOF-Mn=0.4mol CO_2 m^3 adsorbent s^{-1}slightly outperforming the Zeolite 13X=0.35mol CO_2 m^3 adsorbent s^{-1}. This study shows that some of the diamine-appended MOFs can achieve the DOE post-combustion CO_2 capture targets, with noticeably less energy consumption when compared to Zeolite 13X.

Part II

Pre-Combustion Carbon Capture

Chapter 4

Design of Novel PSA Cycles for Pre-Combustion CO_2 Capture

4.1 Introduction

Post-combustion CO_2 capture technology is used to separate CO_2 from conventional coal-fired power plants, after combustion of the fuel. Pre-combustion CO_2 capture on the other-hand is different, here the capture of CO_2 happens before combustion. The pre-combustion CO_2 capture technology is usually implemented in an integrated gasification combined cycle (IGCC) power plant. In a typical IGCC power plant, the coal is gasified to produce syngas; which is primarily made up of carbon monoxide CO and hydrogen H_2. The carbon monoxide, CO, is then converted to CO_2 by the water-gas shift (WGS) reaction. At this stage, before the syngas is sent to the gas turbine for combustion, the CO_2 is captured. Since the syngas is at a pressure >20 bar, it may be favorable to use PSA based separation process.

TDA Research Inc. has patented a new mesoporous carbon modified with surface functional groups that adsorbs CO_2 by strong physical adsorption. The CO_2 surface interactions for the adsorbent is strong enough to allow operation at elevated temperatures, and since the CO_2 is not bonded via a covalent bond, the energy input thus for regeneration is low. Heat of CO_2 adsorption is 21 kJ/mol for the sorbent, this is comparable to that of the net energy loss in sorbent regeneration in the Selexol process. The pore size of the adsorbent is finely tuned in the 10 to 100 Å range. This also eliminates diffusion based limitations and allows for rapid mass transfer. In this chapter, the objective is to develop novel pressure swing adsorbent cycles for the adsorbent; TDA AMS-19. The main target of this project is to show that the material can achieve the targets set by US Dept. of Energy (DOE) for CO_2 purity and recovery is 95% and 90%, respectively. In order to evaluate the materials, a detailed model was used to simulate a three component system of CO_2 H_2 and H_2O using an in-house finite volume code. Novel cycles were configured based on heuristics and

analysis of the predicted solid phase concentration profiles. A graphic scheduling approach was used to schedule the cycles in a pilot scale plant. The basic project scope is shown in the Fig.4.1, the dotted box demarcates the scope of this work.

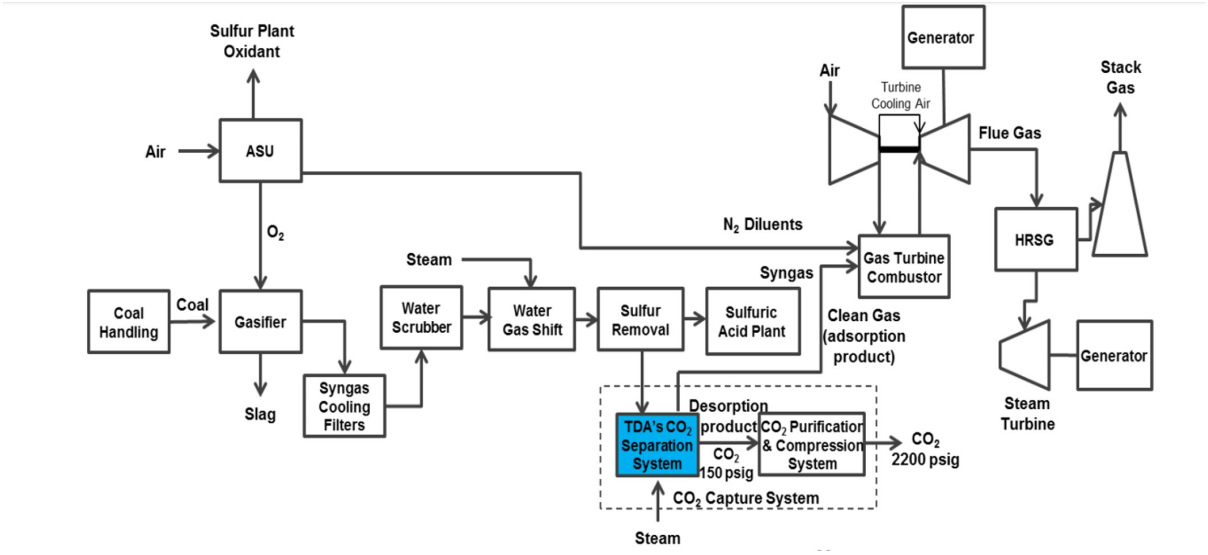

Fig. 4.1: IGCC power plant with CO_2 capture system (the dotted box indicates current project scope) [11]

4.2 Adsorption Equilibria

Adsorption equilibrium data is an important input parameter to accurately simulate a PSA process. In continuation of the previous work on TDA AMS-19; the Sip′s isotherm was used in describing the single and multi-component adsorption equilibrium data. This was done because the Sip′s isotherm provides a better fit at low pressure regions. The Sip′s isotherm was introduced briefly in chapter 2 and the form used in the simulations is given by the following equation:

$$q_i^* = \frac{q_{\mathrm{s,i}}(k_i p_i)^{s_i}}{1 + (k_i p_i)^{s_i}} \tag{4.1}$$

- $q_{\mathrm{s,i}}$ is the adsorbent saturation capacity
- k_{i} is the adsorption equilibrium constant
- s_{i} is a parameter describing the homogeneity of the surface

The Sip′s isotherm consists of eight parameters ψ_{i}, ω_{i}, θ_{i}, $s_{1,\mathrm{i}}$, $s_{2,\mathrm{i}}$, $T_{\mathrm{ref,i}}$, T_{ref}. The H_2 isotherm data is not available on TDA AMS-19, hence needs to be assumed. The Sip′s isotherm parameters for H_2 for this study is obtained from the literature. It is obtained for an activated carbon similar to the TDA AMS-19 and is same as that used in the previous work [11, 34]. The H_2 isotherm is not

measured for TDA AMS-19, therefore the results must be taken with caution. Fig. 4.2 shows the single component isotherm for CO_2, and Table 4.1 lists the corresponding isotherm parameters for the two components. It is also assumed that the third component H_2O is non adsorbing on the material. The process simulations in the section involve the simulation of a multiple component system. Description the competition between the gas species was assumed to reliably predict by an extended Sip′s model for the given conditions.

	ω_i [mol/kg]	ψ_i [kJ/mol]	θ_i [1/pa]	ϕ_i [kJ/mol]	$s_{1,i}$ [−]	$s_{2,i}$ [−]	$s_{ref,i}$ [−]	T_{ref} [K]
CO_2	3.74	-7.87	26.9×10^{-09}	-2.05	0.136	0.110	0.760	281
H_2	6.6	0.0	0.7×10^{-09}	-9.83	0	0	0.93	273

Table 4.1: Single component Sip′s isotherm parameters [11].

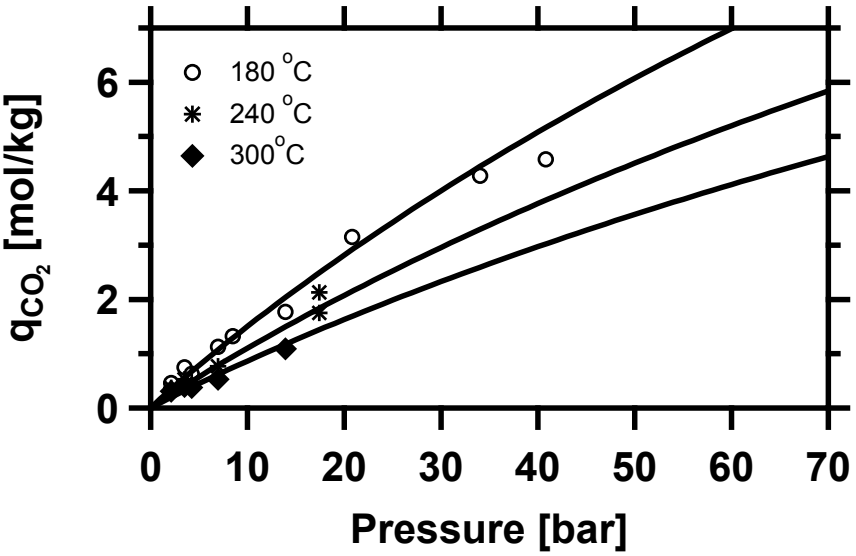

Fig. 4.2: Single component Sip′s isotherms for CO_2 (fitted to TDA′s equilibrium data), the markers represent the equilibrium loading experiments and the lines are the fitted Sip′s isotherm model [11]

4.3 PSA cycle modeling

As discussed in the introductory chapters, pre-combustion based carbon capture technologies operate at different conditions to post combustion processes. In pre-combustion, the inlet stream to the PSA is the outlet of a gasifier. This means the feed composition of this stream is different from post combustion, consisting of CO_2 and H_2 at a mol% of 40% and 60%, respectively. The inlet pressure and temperature of the stream are different from post combustion PSA process. For this work; TDA Research Inc. constraint the operating pressure and temperature range. The PSA

cycles were operated between a high pressure, P_{H} and low pressure, P_{L} of 34.45 bars and 10.00 bar, respectively. 240°C was assumed for the feed gas and 200°C for Low Pressure (LP) steam. Since both CO_2 and H_2 are important products, the performance indicators should include H_2 separation performance. The performance of the PSA cycles discussed in this section is given by the following key performance metrics:

$$\text{Purity, } (\text{Pu}_{\text{CO}_2}) = \frac{\text{Total moles of CO}_2 \text{ in extract product in one cycle}}{\text{Total moles of gas in extract product in one cycle}} * 100 \tag{4.2}$$

$$\text{Recovery, } (\text{Re}_{\text{CO}_2}) = \frac{\text{Total moles of CO}_2 \text{ in extract product in one cycle}}{\text{Total moles of CO}_2 \text{ fed into the column in one cycle}} * 100 \tag{4.3}$$

$$\text{Purity, } (\text{Pu}_{\text{H}_2}) = \frac{\text{Total moles of H}_2 \text{ in product in one cycle}}{\text{Total moles of gas in raffinate product in one cycle}} * 100 \tag{4.4}$$

$$\text{Recovery, } (\text{Re}_{\text{H}_2}) = \frac{\text{Total moles of H}_2 \text{ in extract product in one cycle}}{\text{Total moles of H}_2 \text{ fed into the column in one cycle}} * 100 \tag{4.5}$$

Parameter		Value	
Column Length	L	0.61	[m]
Inner column radius	r_{in}	5.12×10^{-2}	[m]
Column void fraction	ε	0.4	[-]
Particle voidage	ε_p	0.57	[-]
Particle radius	$\mathrm{r_p}$	3.00×10^{-04}	[m]
Tortuosity	τ'	3	[-]
Column wall density	ρ_{s}	7800	[$\mathrm{kg/m^3}$]
Specific heat capacity of gas phase	$\mathrm{C_{p,g}}$	1010	[$\mathrm{J\,kg^{-1}\,K^{-1}}$]
Specific heat capacity of adsorbent phase	$\mathrm{C_{p,a}}$	1877	[$\mathrm{J\,kg^{-1}\,K^{-1}}$]
Fluid viscosity	μ	2.15×10^{-05}	[$\mathrm{kg\,m^{-1}\,s^{-1}}$]
Molecular diffusivity	$\mathrm{D_m}$	4.81×10^{-08}	[$\mathrm{m^2\,s^{-1}}$]
Effective gas thermal conductivity	K_z	0.09	[$\mathrm{J\,m^{-1}\,K^{-1}\,s^{-1}}$]
Inside heat transfer coefficient	h_{in}	0	[$\mathrm{J\,m^{-2}\,K^{-1}\,s^{-1}}$]
Universal gas constant	R	8.314	[$\mathrm{m^3\,Pa\,mol^{-1}\,K^{-1}}$]

Table 4.2: Parameters used in the pre-combustion process simulation

4.3.1 Previous work

In previous studies, TDA AMS-19 was characterized with the help of single component breakthrough experiments and the data was used to fit simulations [11]. Numerous cycles were configured, the performance of each of the cycles are tabulated in Table 4.3, the plot of the CO_2 purity and recovery is shown in Fig 4.3. PSA cycles configuration in the previous work are given below and are shown in Fig 4.4:

- Configuration A: Basic 4-step PSA cycle
- Configuration B: 4-step PSA cycle with light product pressurization (LPP)
- Configuration C: 6-step PSA cycle with steam purge, pressure equalization (PE) and light product pressurization (LPP)
- Configuration D: 8-step PSA cycle with steam purge, two pressure equalizations (PE) and light product pressurization (LPP)
- Configuration E: 6-step PSA with steam purge, pressure equalization (PE) and co-current blowdown with light product pressurization (LPP)

PSA cycle configuration	CO_2 Purity [%]	CO_2 Recovery [%]	H_2 Purity [%]	H_2 Recovery [%]
A	84.8	10.2	62.3	98.7
B	84.9	13.4	63	98.3
C	75.2	99.9	99.9	77.7
D	93.3	99.3	99.6	95.1
E	80.5	99.9	99.9	83.6

Table 4.3: Summary of purity/recovery for CO_2/H_2 for the different PSA cycle configuration reported above. Performance indicators for cycles C, D and E are reported on dry basis [11]

Although fairly complex cycles were formulated, the DOE targets for purity and recovery of CO_2 were not met. This leaves room for improvement, via modifications and new configurations. It should be noted that these cycles are not optimized, so the performance of each of these cycles is expected to improve after optimization.

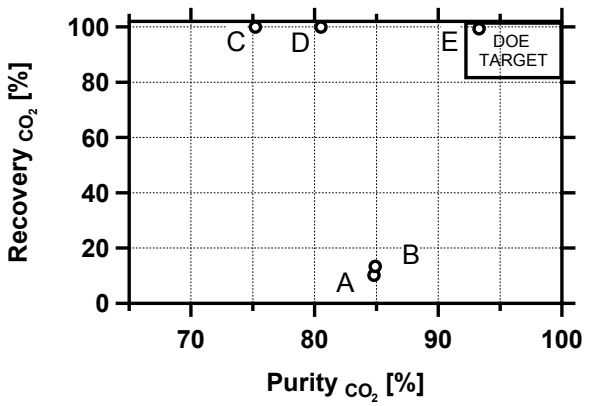

Fig. 4.3: Cycle performance for CO_2 for the different PSA cycles reported in the previous work [11] (Markers corresponds to cycle configurations reported in Table. 4.3

4.4 Results and Discussions

4.4.1 Cycle Configuration

In this study, in order to improve the performance of the cycles, modifications to the old cycle configurations were looked into. In congruence with the previous work, the six step cycle with LPP (configuration C) was used as a base case for improvement. It had shown a performance of CO_2 purity and recovery of 75.2% and 99.9%, respectively. The following cycles were configured and their performances are highlighted in this section. The schematics of the cycles studied in the chapter are given in the Fig.4.5.

- Configuration F: Six-Step cycle with one Pressure Equalization, Purge and LPP
- Configuration G: Eight-Step cycle with two-Pressure Equalization, Purge and LPP
- Configuration H: Ten-Step cycle with purge, three- Pressure Equalization and LPP
- Configuration I: Seven-Step with one-Pressure Equalization, Purge, Depressurization, and LPP
- Configuration J: Nine-step with two-Pressure Equalization, Purge, Depressurization, and LPP
- Configuration K: 4-step with Purge and LPP

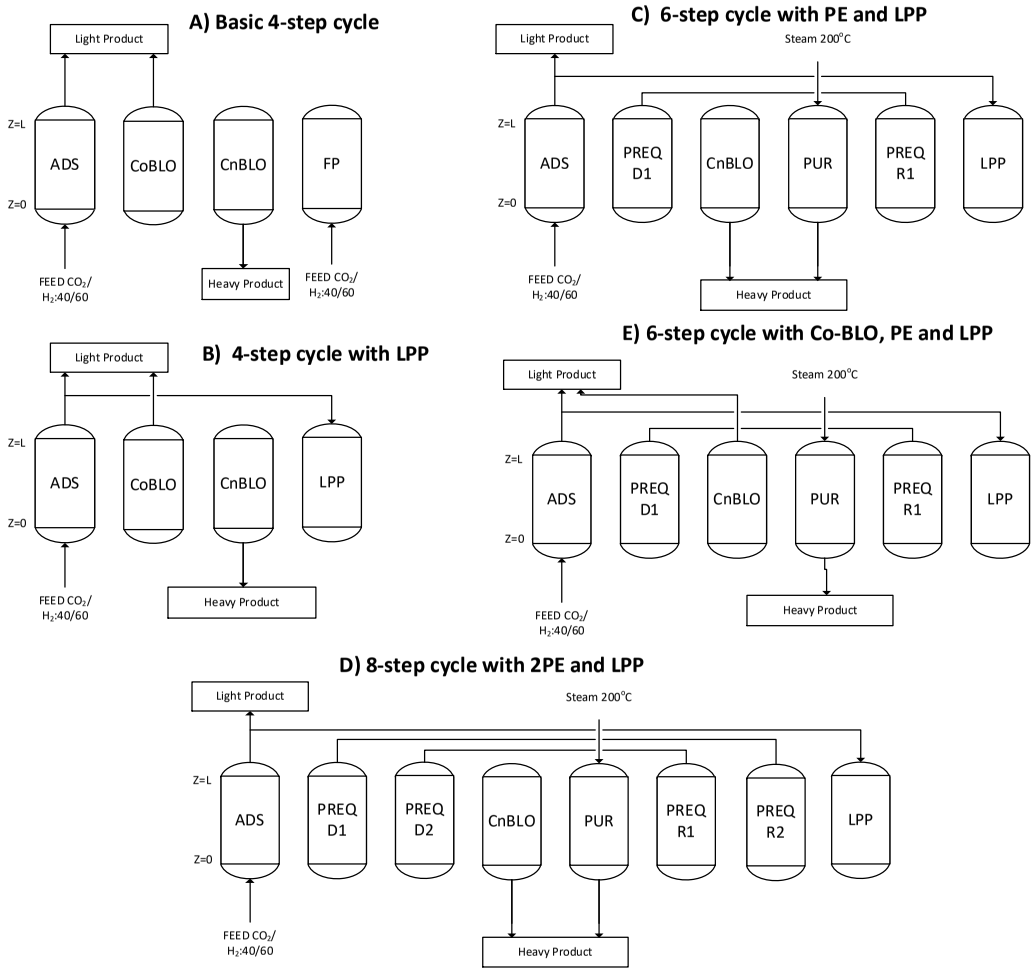

Fig. 4.4: Process schematics for different PSA cycle configurations studied in the work a) Basic 4-step PSA cycle b)4-step PSA cycle with light product pressurization (LPP) c) 6-step PSA cycle with steam purge, pressure equalization (PE) and light product pressurization (LPP) d) 8-step PSA cycle with steam purge, two pressure equalizations (PE) and light product pressurization (LPP) e) 6-step PSA with steam purge, pressure equalization (PE) and co-current blowdown with light product pressurization (LPP)

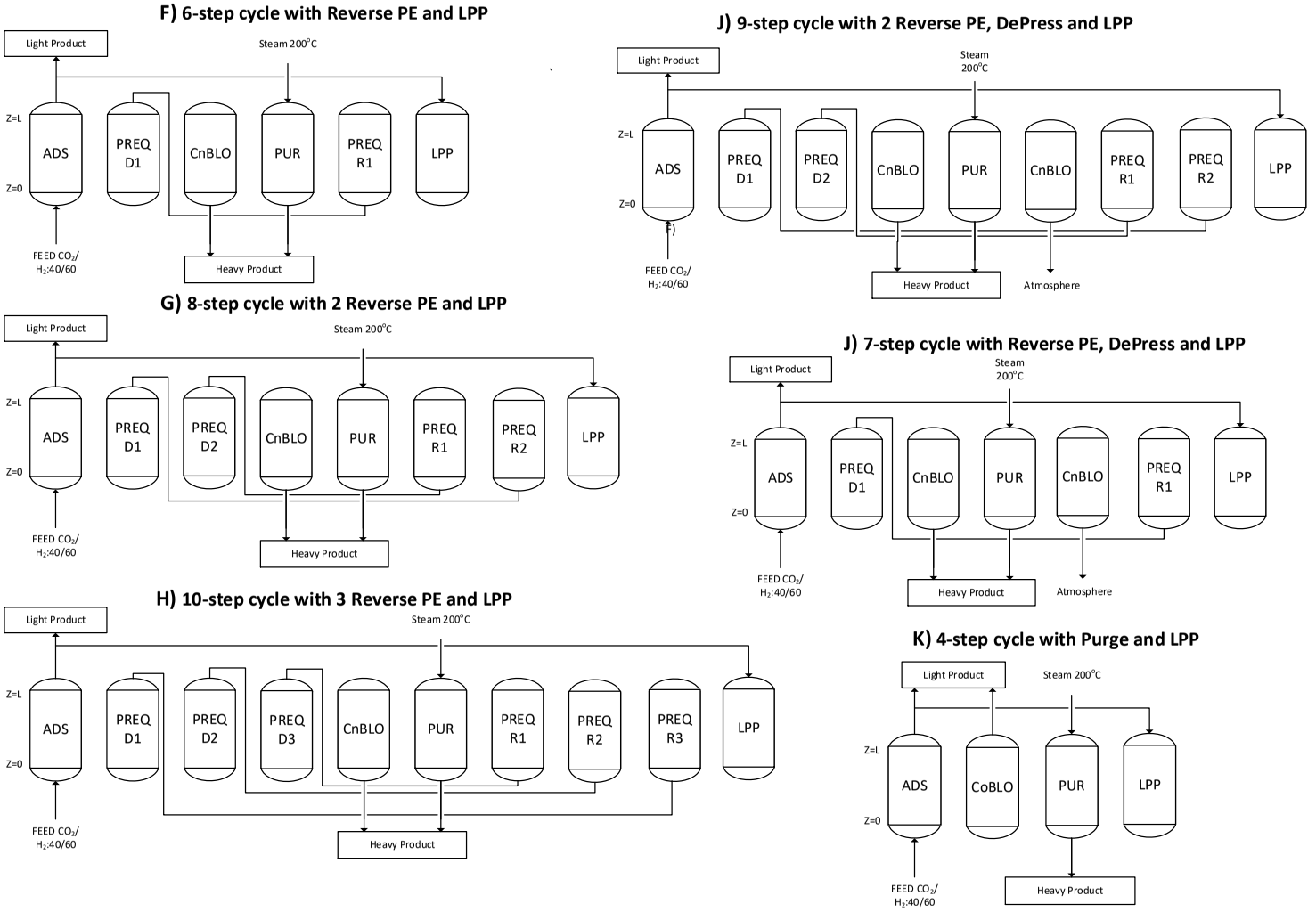

Fig. 4.5: Process schematics for different PSA cycle configurations studied in the work F) 6-Step with 1-PE, Purge and LPP G) 8-step with 2-PE, Purge and LPP H) 10-step with 3-PE, Purge and LPP I) 9-step with 2-PE, Purge, Depressurization, and LPP J) 7-step with 1-PE, Purge, Depressurization, and LPP K) 4-step with Purge and LPP

Let us consider the six-step cycle with LPP from the previous work, it consists of a high pressure adsorption, in this step the CO_2 is preferentially adsorbed. This is followed by a pressure equalization step; here the H_2 is removed from the system and stored in a tank. This is followed by a combination of an evacuation and steam purge to reactivate the bed. The stored H_2 from the second step is now introduced into the bed in a step called pressure equalization. This is then followed by a pressurization with the light product. This PSA cycle includes a low pressure steam purge steam and single pressure equalization (PE) over the basic 4-step with LPP.

The pressure equalization step helps in improving the purity of the raffinate product, while not adding to the energy costs. Even though energy consumption is not calculated in this work for these cycles, it is an important aspect of process design to reduce capital costs and energy costs. This is achieved by the addition of pressure equalization steps, reduction of the energy consumed in the cycle the co-current blowdown step is substituted with a pressure equalization step along with the need for having a H_2 compressor. The product from this step is fed back into a receiver column at a later stage in the cycle. Also, this gives us an opportunity to increase the mass transfer zone in adsorption step because the CO_2 that would have been lost in the raffinate product is now recycled back in the cycle. From a simulation perspective, the implementation of this step has challenges in that the intermediate pressure now cannot be fixed. This has to be determined by trial and error. This approach delays the time required to perform the process simulation.

In order to avoid lengthy computations, the implementation of this step is carried out using an optimized expression. The approach has been described in our previous work [11]. The PE step is implemented using a donor, tank and a receiver. The donor is depressurized from a state of high pressure to the intermediate pressure the is dictated by the optimized expression. The receiver is pressurized by the product collected from the depressurization step and the pressure of the receiver column would be an intermediate pressure. For this step to be satisfactory the moles desorbed from the donor should be equal to the moles adsorbed in the receiver step. It was done by performing a series of such calculations, using a simple algebraic expression that relates the intermediate pressure to the high and low pressure is estimated. This expression is used in the subsequent simulations for the calculation of intermediate pressure.

Due to the availability of LP Steam at the IGCC power plant, a low pressure purge step was used after a co-current blowdown step. The steam has no affinity for this material and this helps as a sweep gas that helps remove all the residual CO_2 from the bed after the evacuation step and is collected and removed in the compression phase of the CO_2. This step enhances the CO_2 recovery by removing all the residual CO_2 in the solid state on the adsorbent. And also helps in homogenization of the bed concentration. The extract product from this step and the earlier co-current blowdown is used to account for the amount of CO_2 recovered in each cycle. The purge outlet stream is a wet product stream and the performance metrics reported are on dry basis where the steam is removed from the system after compression.

A parametric study on the various time variables revealed that running the cycle at operating

conditions as given in table.4.4, gives a base performance of CO_2 purity of 86.5% and a CO_2 recovery of 98.2%. To improve on the performance the modifications were made in the direction of pressure equalization.

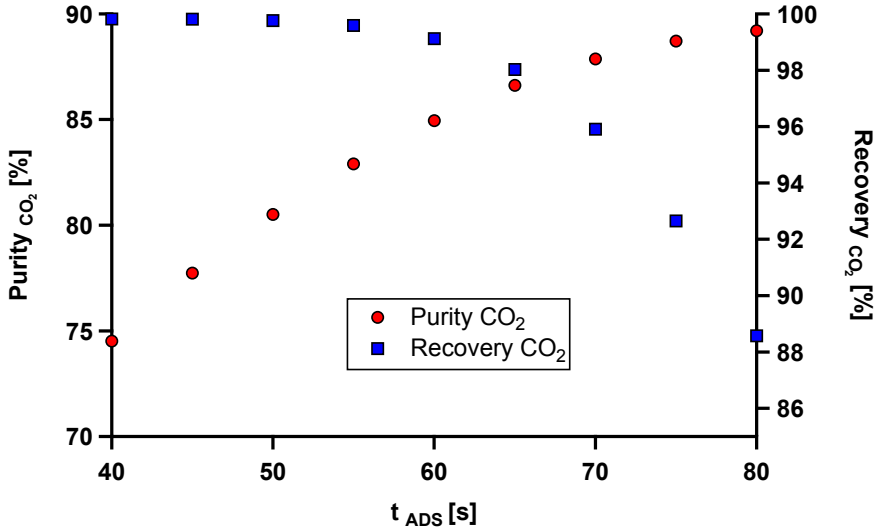

Fig. 4.6: The variation of purity and recovery as a function of cycle time for configuration C, CO_2 purity (red) CO_2 recovery (blue) for t_{ADS} varying from 40 [s] to 70 [s] at CSS

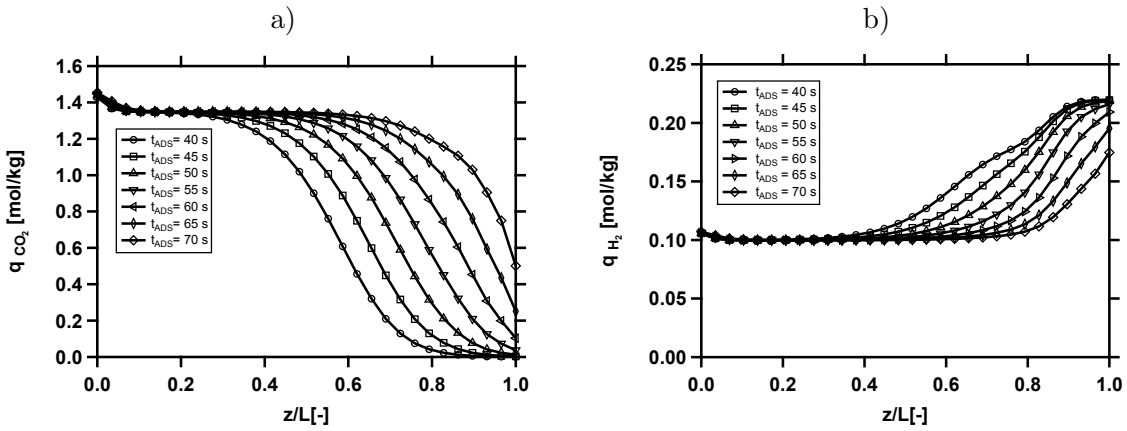

Fig. 4.7: The solid state concentration profiles for a) CO_2 and b) H_2 plotted along the bed for increasing t_{ADS} at CSS at the end of the Adsorption step.

To understand the effect of increasing the adsorption step time, t_{ADS} on the performance indicators, a parametric study was conducted. The adsorption time, t_{ADS} was varied from 40 [s] to 70 [s] in increments of 5 seconds, while the other parameters are kept constant. The effect on the purity and recovery of CO_2 is shown in the Fig 4.6. The recovery of CO_2 decreases from 99.9% to 88%, but the effect on CO_2 purity is profound. The CO_2 purity increases from 75.2% to 89%, by simply increasing adsorption time. This effect can be explained by observing the propagation of the solid

phase concentration profile of CO_2 at cyclic steady state. In Fig.4.7, as the adsorption time is increased, the H_2 solid state profile is pushed towards the z=L. This reduces the H_2 in the extract product in the latter stage of the cycle. But this effect encounters a maxima, i.e. the recovery of CO_2 drops sharply after 70 secs. The reason being, the CO_2 has will breakthrough to the z=L if the adsorption time is any longer, thus contaminating the raffinate product.

The operating conditions with, t_{ADS} equal to 60 s was chosen as a base case for further improvement. The feed rate v_{feed} and purge feed v_{PUR} was kept at 0.1 and 0.1 $\frac{m}{s}$, the other operating conditions for this case and the ones used for the other configurations is listed in Table.4.4. The performance of each of the configurations from Fig.4.5 for the operating conditions in Table. 4.4 are shown in Fig. 4.8

	t_{ADS} [s]	t_{CnBLO} [s]	t_{PUR} [s]	t_{PREQD1} [s]	t_{PREQD2} [s]	t_{PREQD3} [s]	P_{INT1} [bar]	P_{INT2} [bar]	P_{INT3} [bar]
F	60	90	40	45	-	-	21.8	-	-
G	60	90	40	15	30	-	25.8	17.5	-
H	60	90	40	15	15	15	27.4	21.4	15.5
I	60	90	40	45	-	-	18.81	-	-
J	60	90	40	15	30	-	23.7	14.1	-

Table 4.4: Operating conditions (step times and intermediate pressures) for the different PSA cycle configurations are shown in Fig. 4.5

PSA cycle configuration	CO_2 Purity [%]	CO_2 Recovery [%]	H_2 Purity [%]	H_2 Recovery [%]
F	85.2	99.05	99.34	88.47
G	89.52	99.72	98.49	92.20
H	92.04	99.71	99.83	94.04
I	90.03	97.94	98.57	92.76
J	96.96	95.82	96.95	98.09

Table 4.5: Summary of purity/recovery for CO_2/H_2 for the different PSA cycle configuration reported above. Performance indicators for the cycles are reported on dry basis

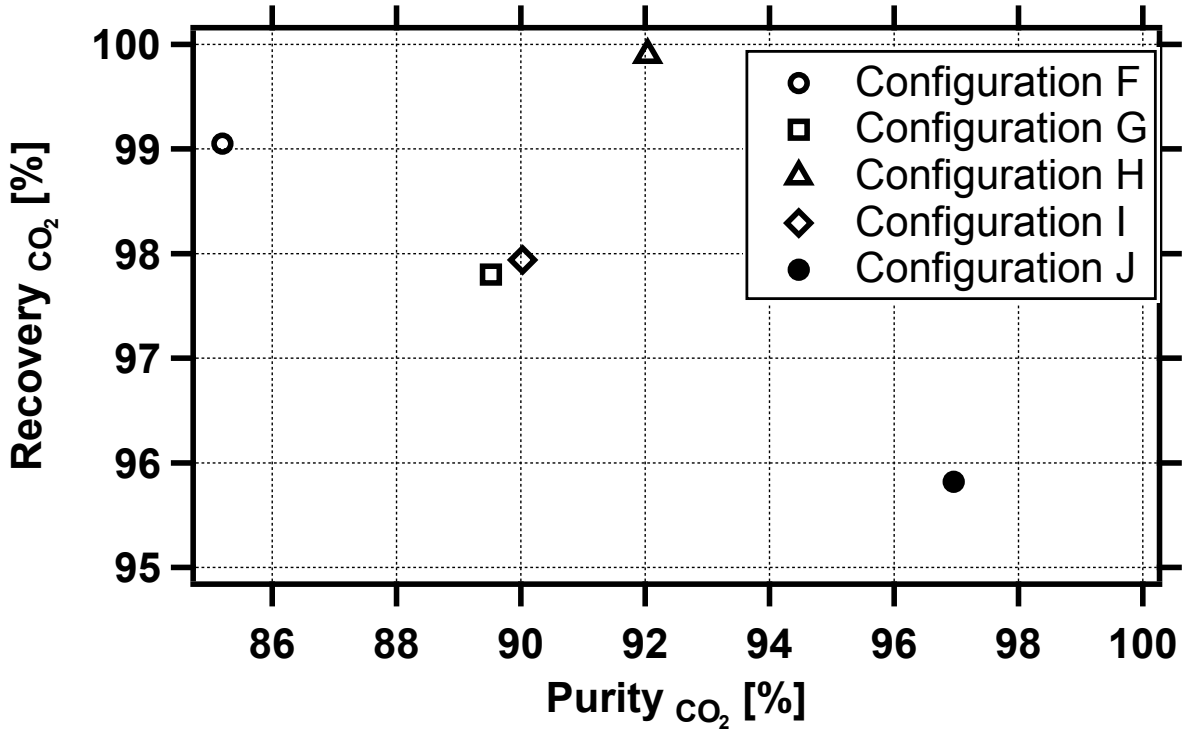

Fig. 4.8: Cycle performance for CO_2 for the different PSA cycles reported in this work

4.4.2 Effect of Feed End Equalization

In order to improve the performance of the cycle, it would be helpful to consider the profiles in the column. For example, let's consider the solid phase CO_2 profiles for the operating conditions [t_{ADS} =60 s, $t_{\mathrm{PREQ-D}}$ =45 s, t_{CnBLO} =90 s, P_{INT} =21.8 bar, P_{L} =10 bar, v_{feed} =0.1 m/s and v_{PUR} =0.1 m/s], the results are shown in Fig.4.9.b) The shaded region represents the amount of CO_2 that will be lost in the subsequent adsorption step. This translates into a loss in the recovery of CO_2. One of the approaches to reduce this loss could be to introduce the gas from pressure equalization step at z=0; Fig.4.9(c) shows the change in configuration. In order to analyze the effectiveness of the change, the simulation was repeated by merely changing the direction of the gas receiver, while maintaining the other operating conditions. Making this change, improved the purity from 86% to 87% and recovery improves from 97.4% to 99%. The performance improvement can be visualized by looking at the solid state concentration profiles for CO_2 and N_2 in Fig.4.9(e,f). This change also leads to a reduction in CO_2 contaminating the bed at z=L end. Although the purity and recovery of CO_2 and H_2 increases, the change is not very significant. Further optimization of the two configurations would show a clear improvement in this configuration.

This modification is implemented in the simulation by collecting the product from the pressure equalization donor step into a tank, at the intermediate pressure P_{INT}. It is then reintroduced into the feed end of the pressure equalization receiver. This not only allows for a larger portion of the

bed to be used without any loss of CO_2 in the in the raffinate product, but also helps in expelling more H_2. Thus improving the CO_2 purity. This also allows for less contamination in the product end with CO_2 as the product fed into the LPP step is leaner in CO_2 then before.

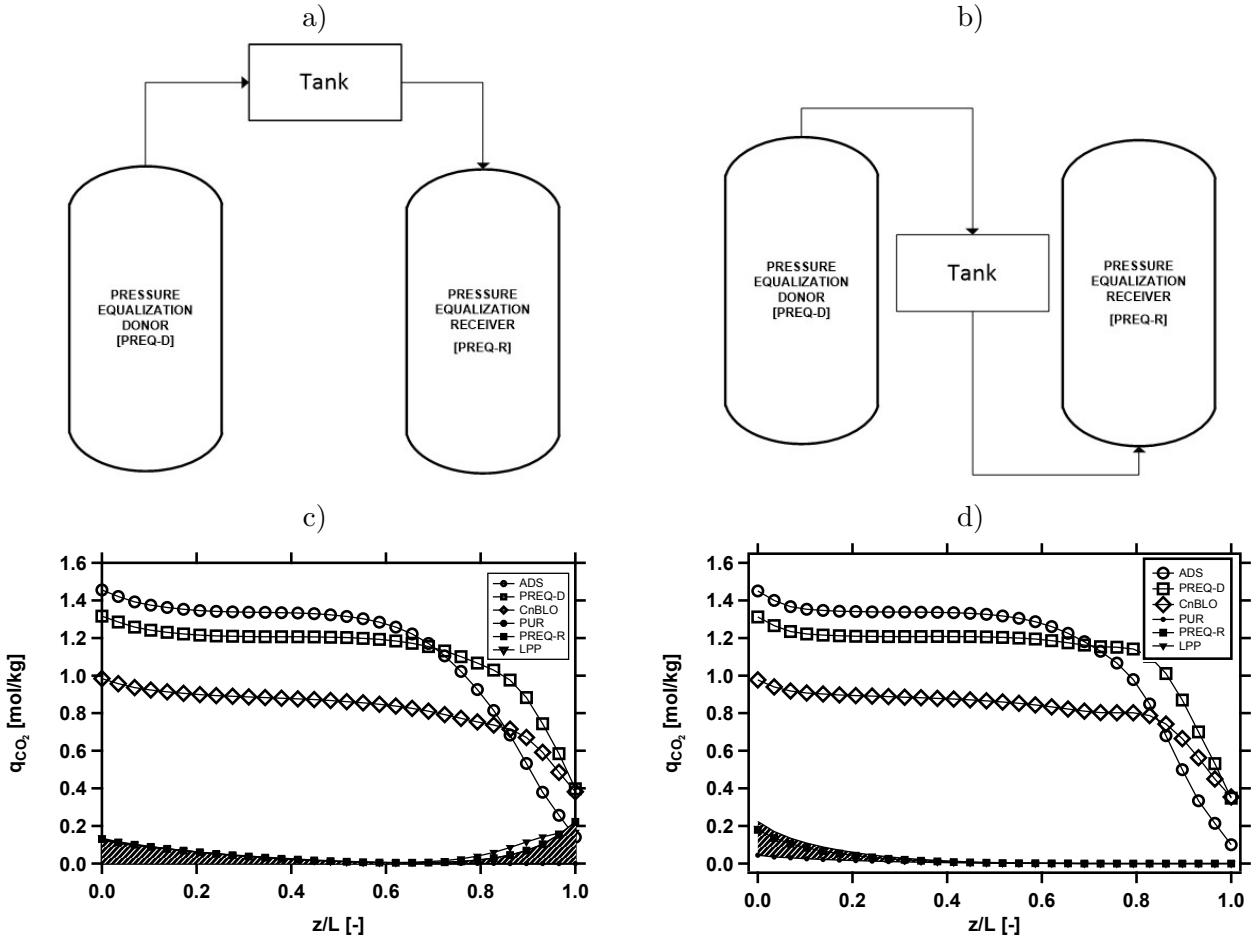

Fig. 4.9: The effect of switching the direction of pressure equalization in configuration C; on recovery of CO_2 a) shows the schematic of the direction change b) the solid state CO_2 concentration profile for the configurations for the operating condition in Table.4.4. The shaded region in c) and d) represents the amount of CO_2 that is lost in raffinate product, for each cycle

4.4.3 Effect of Additional Pressure Equalization Steps

In the previous work, the effect of 2 pressure equalization steps on the performance of the cycle was studied. The maximum purity achieved for the 2 pressure equalization configuration was 80%. This was a 5% points increase in CO_2 purity when compared to one pressure equalization. A similar trend was seen when the new modified 8-step cycle was simulated, a CO_2 purity of 89% was achieved. This was a 4% increase in CO_2 purity. It can be clearly stated that the CO_2 purity has a direct relation to the intermediate pressure at which the process is operated. To improve on the purity of

the extract product, lower intermediate pressures need to be reached. This would help desorb the H_2 in the bed before CO_2 is collected. Since equalizing pressures using a donor-receiver, we have no control over the intermediate pressure. Thus achieving higher purity values would mean addition of more pressure equalization steps. In this section, we simulate and analyze the impact of adding an extra pressure equalization step as a way to achieve product purity.

The 8-Step PSA cycle with two pressure equalizations will have two intermediate pressures, they are determined similar to the 6 step PSA cycle. The pressure of the first pressure equalization donor is reduced from high pressure P_{H} to an intermediate pressure intermediate pressure $\mathrm{P_{INT1}}$ and the second pressure equalization donor pressure is reduced from that intermediate pressure to a second intermediate pressure $\mathrm{P_{INT2}}$. The desorbed moles are collected in a tank and are used to pressurize the first and second pressure equalization receivers respectively from a low pressure of P_{L} to intermediate pressure $\mathrm{P_{INT2}}$. The intermediate pressure $\mathrm{P_{INT1}}$ to the second intermediate pressure $\mathrm{P_{INT2}}$. The optimization was done in the previous study was used to calculate these intermediate pressures. A linearized expression was created to find the value of P_{INT}. The difference in the moles flowing in to the moles flowing out are calculated to check the validity of the simulation.

The 8-step PSA cycle was able to improve the CO_2 purity to =89% by removing more H_2 in the pressure equalization steps. The 10-step PSA cycle is able to further improve on CO_2 purity to 92.3% by the removal of higher amount of H_2 from the bed before pressure equalization. As show in the Fig.4.10, the lower intermediate pressures end up removing a higher amount of H_2 when compared to the 6-step cycle. The intermediate pressures given in Table 4.4 show the change in the intermediate pressures. This directly correlates to an increase in CO_2 purity. The intermediate pressure achieved in the 6 step PSA cycle was 21.8 bar, the intermediate pressures achieved in the 8-step and 10-step cycles are 17.5 and 15.51 bar, respectively. A lower intermediate pressure in the 2 and 3 pressure equalization allow for a smaller amount of H_2 present on the bed before extract is collected. Figure.4.10 shows the solid state concentration of H_2 in the bed for two pressure equalization in a) and three pressure equalization in b). The amount of H_2 removed in the three pressure equalization steps is more than the amount removed in the cycle with two pressure equalization steps. This was done using identical process conditions and step times, the 10-step cycle which was better than the 8-step cycle.

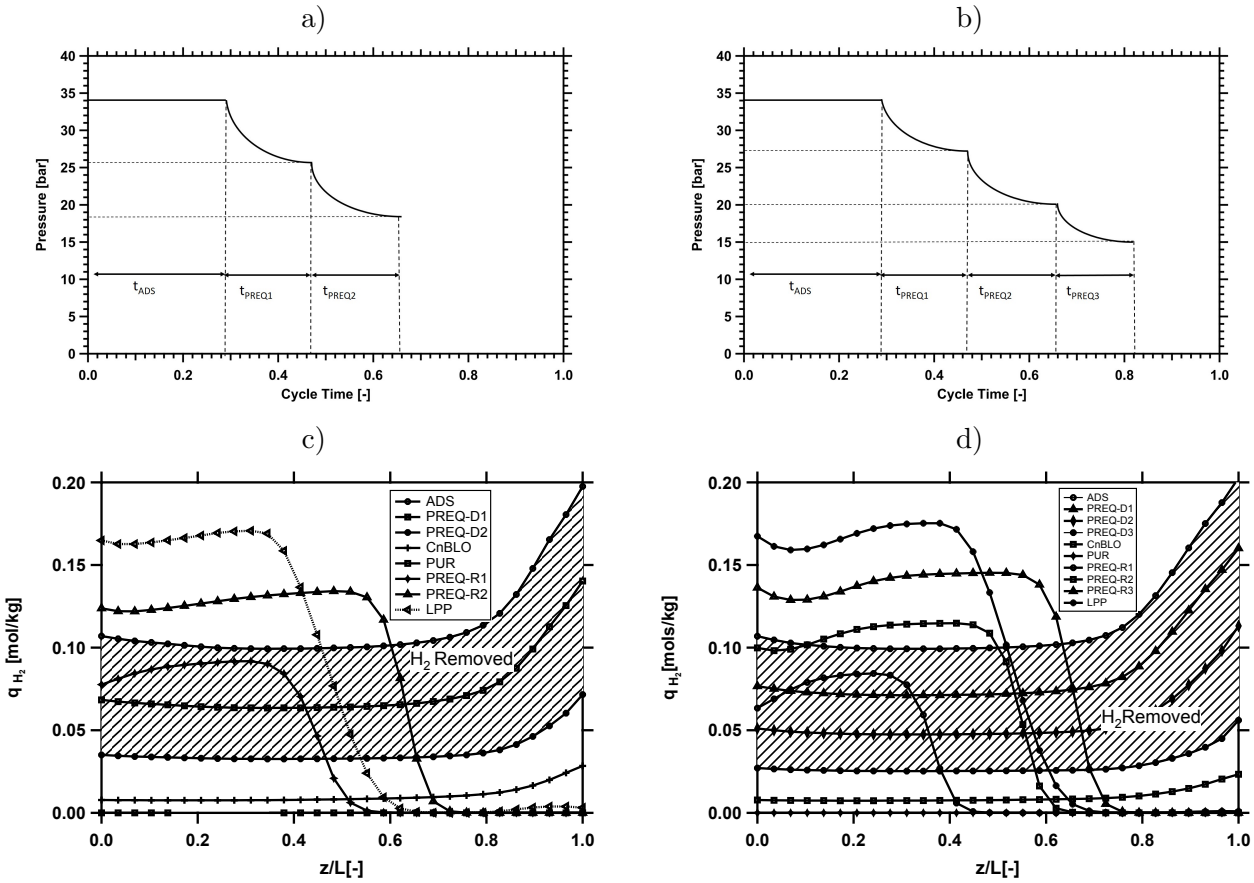

Fig. 4.10: Process schematics and H_2 solid phase profiles for (a) 8-step PSA cycle with one pressure equalization steps and (b) 10-Step PSA cycle with two pressure equalization steps. The shaded area in c) and d) represents the H_2 collected in the extract stream

4.4.4 Effect of Low Pressure and Depressurization step

As we have seen from the earlier section, additional pressure equalization steps led to an increase in CO_2 purity. The CO_2 purity achieved by three pressure equalizations was 92%. This is not high enough to meet the DOE target for CO_2 purity. The purity of the extract is controlled by the intermediate pressure used in the cycle. This is in-turn, dictated by the low pressure at which the extract is collected, which in this case is 10 bar. Since low pressure is a prior constraint on the system it has to be maintained at 10 bar. By reducing the pressure of the system after the extract product is collected, before the pressure equalization step in the cycle can be a way to reduce the intermediate pressure, P_{INT}. This led to the addition of a novel depressurization step, the vessel is reduced to 1 bar. This causes the initial pressure of the pressure equalization receiver to be at 1 bar. This leads to a lower intermediate pressure.

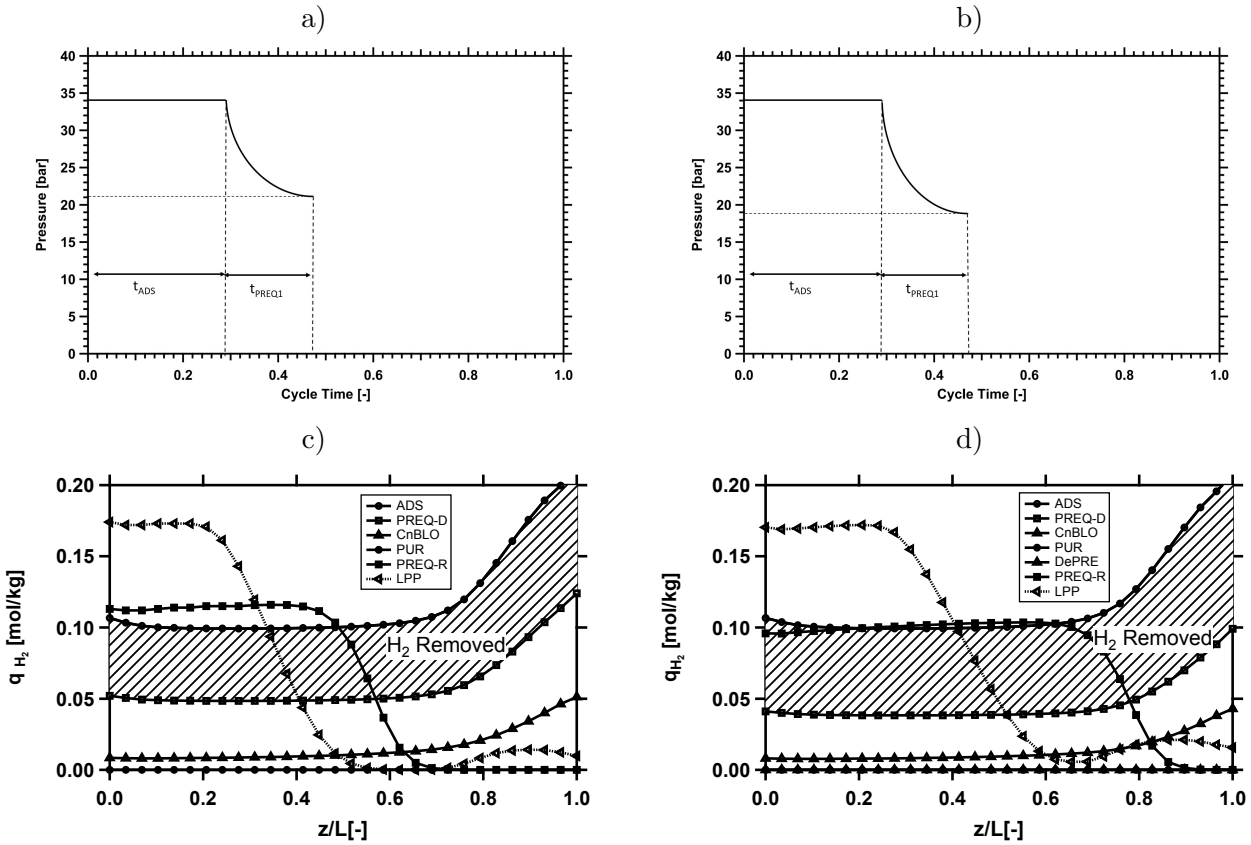

Fig. 4.11: Process schematics and H_2 solid phase profiles for (a) 6-step PSA cycle base case and (b) 7-Step PSA cycle with depressurization step. The shaded area in c)and d) represents the H_2 collected in the extract stream

This is implemented by reducing the pressure of the system to atmospheric pressure. This is lower than the pressure of the extract product, which is still maintained at 10 bar. The primary composition of this depressurization is the LP steam from the column after the purge step. The loss of LP steam was found to not be a significant quantity, when compared to the total amount used in the purge step. The intermediate pressure, P_{INT}, achieved due to one pressure equalization was 21.8 bar. The addition of the depressurization step allowed for an intermediate pressure, P_{INT}, of 18.8 bar. This is a significant reduction of intermediate pressure without sacrificing much on CO_2 recovery. This significantly increases the CO_2 purity (as seen in Fig. 4.8), and allows the cycle to reach closer to DOE targets for CO_2 purity when compared to a 6-Step cycle. Also, since the CO_2 is completely removed from the bed in the purge step, there is no effect on the CO_2 recovery.

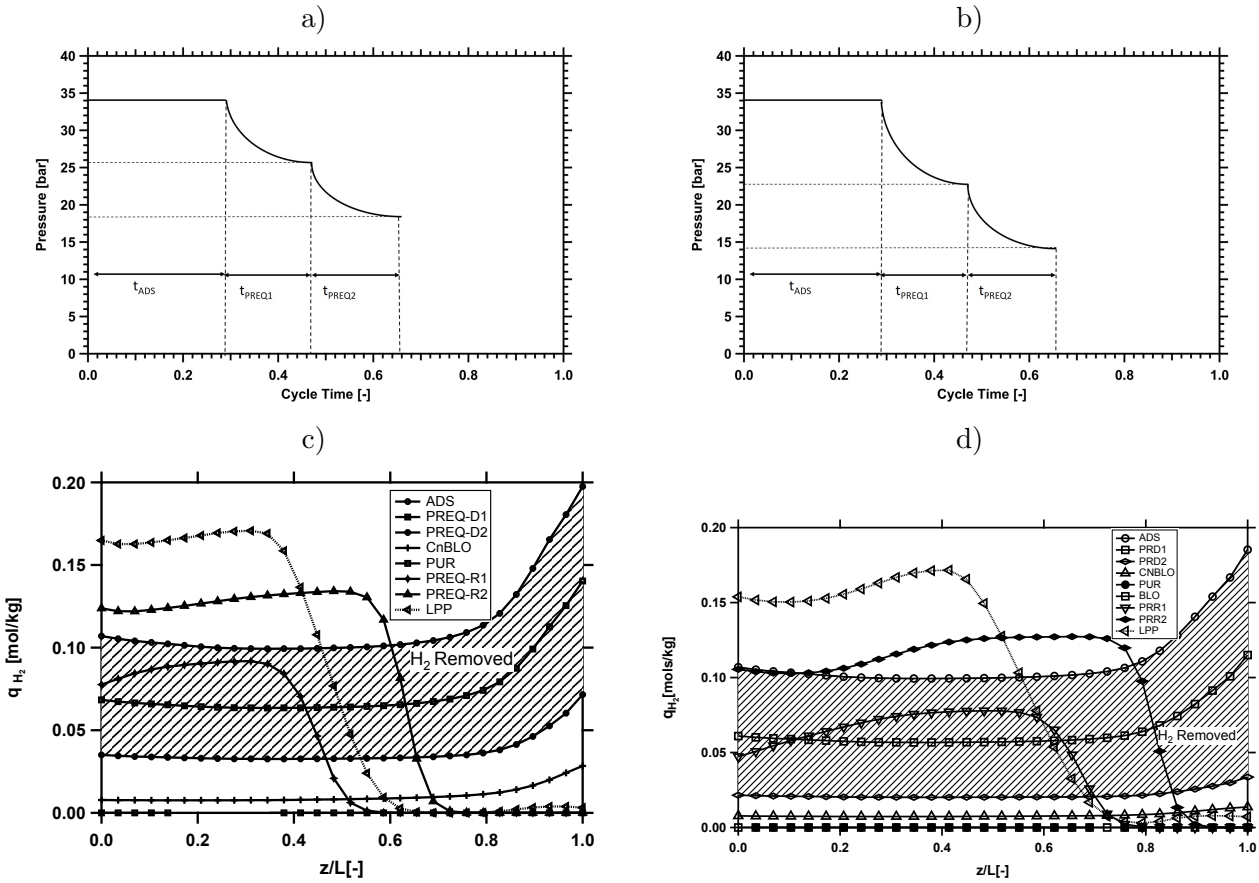

Fig. 4.12: Process schematics and H_2 solid phase profiles for (a) 8-step PSA cycle base case and (b) 9-Step PSA cycle with depressurization step. The shaded area in c)and d) represents the H_2 collected in the extract stream

The additional depressurization step although does bring the CO_2 purity figures to 90 % it still would not be sufficient to satisfy the DOE targets for CO_2 purity. This lead to implementing the same depressurization step on an 8 step with two Pressure equalization cycle. This change would allow for a much lower intermediate pressure and would thus bring the extract purity higher by removal of more H_2 from the bed. The CO_2 purity achieved in this cycle was 96.7%, this was due to the fact that the intermediate pressure P_{INT1} and P_{INT2} in this cycle were 23.7 and 14.1 bar, respectively. These cycles show better performance when compared the 6 and 8 step cycles can be understood by observing Fig. 4.11 and 4.12. In both figures, the pressure profiles are shown for the cycle configurations, along with this the H_2 concentration profiles are shown. The H_2 solid state concentration profiles represent the H_2 in the bed at the end of each step at CSS. It can be observed that due to the lower intermediate pressures, more amount of H_2 is removed from the bed. This amount can be visualized in the shaded region in Fig. 4.11 and 4.12 b). This is the reason for a higher CO_2 purity, at the same operating conditions.

4.4.5 Configuration K: 4-step PSA cycle with Purge and LPP

Even though some of the above cycles have crossed the DOE targets for 95% purity and 90% recovery upon optimization of the operating conditions. It was found that the amount of CO_2 being collected in the CO_2 evacuation step was dis-proportionally small when compared to that recovered in the purge step. This can be observed by looking at Fig.4.13, which shows the solid phase concentration profiles for CO_2 in the cycle configuration (F). The shaded areas represent the CO_2 removed in the counter current blowdown step and LP steam purge step. This means that the cycle could be operated without an evacuation step and still provide high recoveries of CO_2. The purge step would be the only step responsible for reactivation of the bed. The main advantage of this cycle is the pressure at which the CO_2 product was collected could be at a higher pressure. This would translate to lesser compression costs at the CO_2 compression and storage unit. The cycle when run with the operating conditions from Table.4.4, a CO_2 purity of 98% was obtained, but the CO_2 recovery was 86%.

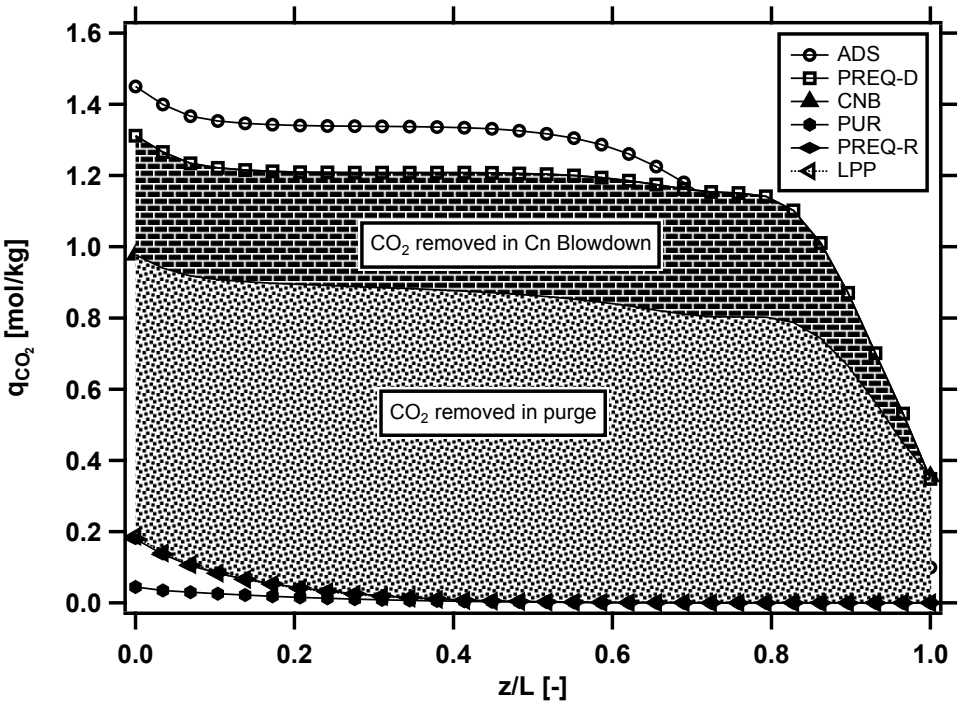

Fig. 4.13: The CO_2 solid phase concentration at CSS, for configuration (F) at the operating conditions specified in Table 4.4. The two shaded areas represent the CO_2 removed in the two reactivation steps.

Optimization of the cycle

Since this cycle configuration is different in its working when compared to the other cycles, it would not be fair to judge the performance of this cycle with the operating conditions used for the

comparison of the other cycles. There is no intermediate pressure, or an evacuation time. Hence to understand the full potential of this cycle an optimization was performed. This cycle was optimized using a GA based optimization to maximize the purity and recovery of CO_2 with the following as decision variable ranges:

t_{ADS} [s]	t_{BLO} [s]	t_{PUR} [s]	P_L [bar]	v_{feed} $[m/s]$	v_{PUR} $[m/s]$
20-200	20-200	20-200	10-17.5	0.1-2	0.1-2

Table 4.6: Process conditions for optimization of the 4-step PSA process

The objective functions used were Eq 4.6 and 4.7, where the CO_2 purity and recovery were sanctimoniously optimized by minimizing the following equations. The lower bound of purge step pressure P_L was fixed to be 10 bar. The resulting CO_2 purity-recovery Pareto is shown in Fig.4.14. As seen from the figure, a maximum purity of 97.6% for a CO_2 recovery of 90% was achieved.

$$J_1 = \frac{1}{\mathrm{Pu}_{CO_2}} \tag{4.6}$$

$$J_2 = \frac{1}{\mathrm{Re}_{CO_2}} \tag{4.7}$$

To understand the effect of purge pressure, P_L, for a minimum CO_2 recovery of 90%, the best purity points were plotted against their corresponding P_L. The extremities of this curve are shown in Fig.4.15. From this plot, it can be seen that this process cycle can achieve the CO_2 purity as high as 98% for a low pressure, $P_L = 10$ bar. From Fig. 4.15, we can also observe that for a minimum purity of 95% the minimum low pressure, P_L, necessary is 14 bar. This would mean that, less energy would be spent in the actual compression of CO_2 for eventual sequestration. Here the CO_2 is generally compressed to 150 bar from P_L bar. This would possibly mean lesser compression cost and hence energy saving. On the other hand, this would also mean addition of an additional compressor that would be used to compress the H_2 removed at the co-current blowdown step, that would then be sent to the gas turbine. This may offset the cost of compression in the ultimate CO_2 compression stage, and a further a full IGCC plant wide energy optimization may help in answering that question. But in the scope of this study, this cycle gives the best trade off between purity and recovery of CO_2 and H_2.

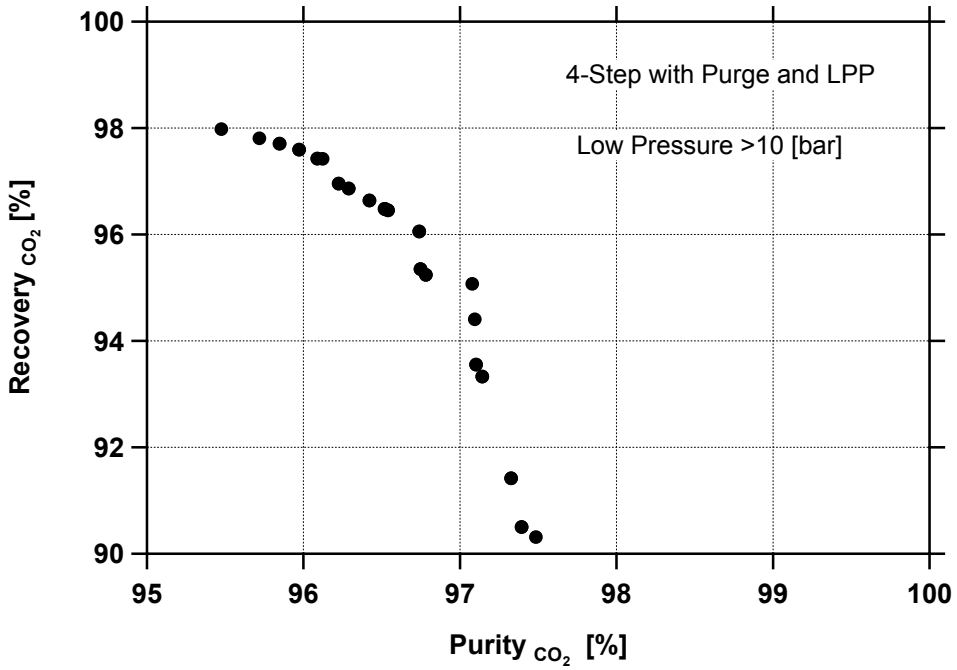

Fig. 4.14: Pareto curve for process optimization to maximize CO_2 purity and recovery for 4-step cycle with Purge and LPP, PSA cycle, generated while fixing the lower bound of P_L to the value 10 bar

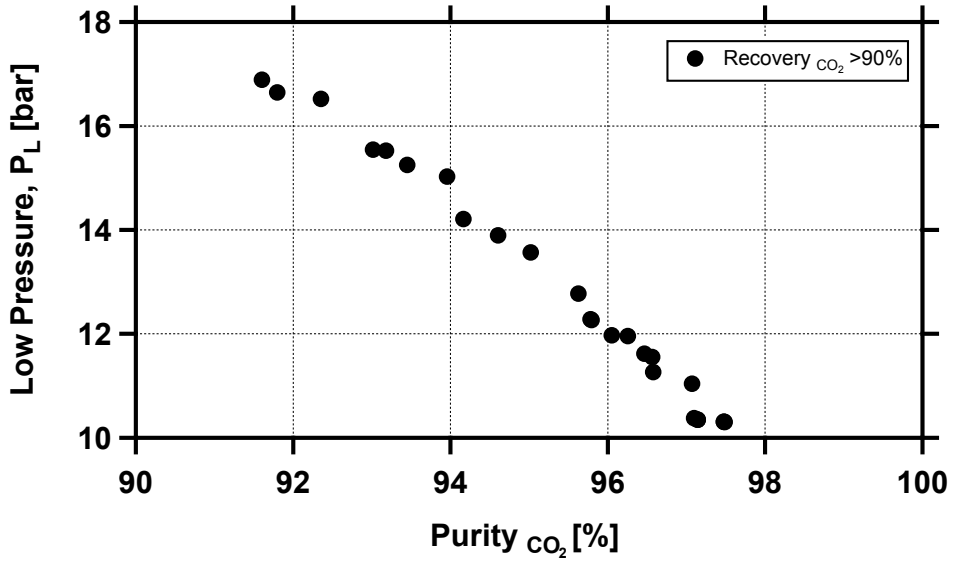

Fig. 4.15: The variation of P_L vs purity of CO_2 in dry basis

4.5 Scheduling of the Cycles and Graphical Representation

Scheduling the time intervals obtained from the optimizations to a PSA unit is an important step towards implementation. However, this is not a straight forward process, because of the complex cycle configurations involved. The interplay between steps, such as the one between pressure equalization; donor and receiver, make it tricky to ensure continuity of the process. To make the process continuous, idle times should be added between various stages. This changes the productivity values calculated by the simulation. There are also cases were the number of columns required to run the set of operating conditions is more than a dozen. This is impractical since there is a limit of using eight beds in the pilot plant. Keeping these problems in mind, scheduling of the times for each of these configurations for many operating conditions should be performed.

Many constraints can be considered for different cycle configurations, depending on which the cycle configuration is scheduled. The most important one is a continuous feed, for practical implementation of any PSA process. Discontinuity would mean usage of large buffer tanks or discontinuous compressors, this would require a higher capital cost and would be impractical. A simple algorithm based on the graphical methodology specified in Ritter *et.al.* was used [57]. The operating conditions with the smallest added idle times are then chosen for the scheduling and is shown in this thesis.

TDA Research Inc. has designed a pilot scale PSA unit, that can evaluate the performance of cycles using syn-gas. The unit is designed to treat 100 scfm of shifted synthesis gas syn-gas flow into the CO_2 separation skid, which is equivalent of 0.1 MW power for syn-gas derived from oxygen blown gasifier. Of the cycles that have been configured, only the 4 step with Purge and LPP and 9 step cycle with depressurization step and LPP met the DOE targets at a low pressure P_L of 10 bar. All the other cycles met the DOE targets when the P_L limit was relaxed to less than 10 bar. Hence for this section, we will schedule the two cycles for the following operating conditions. The test unit consists of two parts:

- The Gas Conditioning Unit (GCU), the primary function of which is to adjust the concentration and purity of the synthesis gas.
- The high temperature pressure swing adsorption (PSA) based CO_2 Separation Unit.

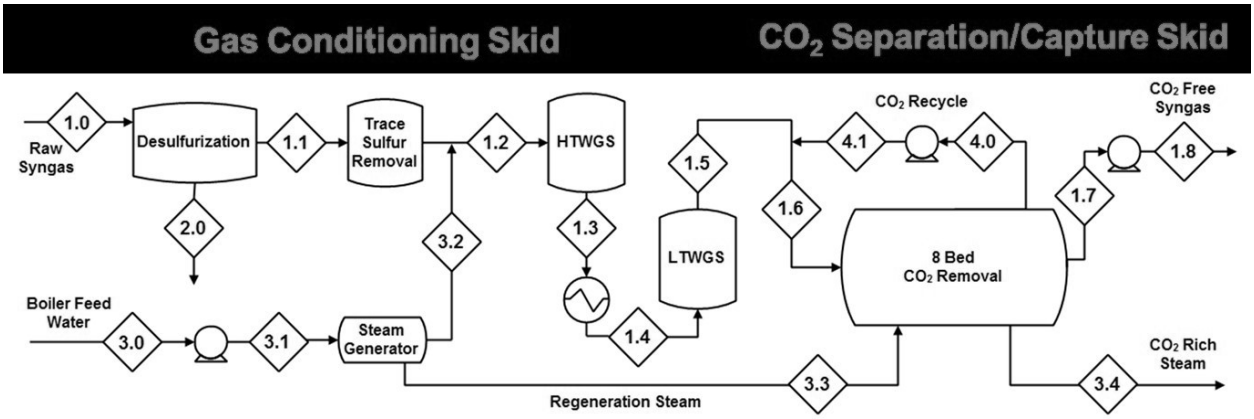

Fig. 4.16: The PFD for the pilot test unit setup by TDA Research Inc.

	t_{ADS} [s]	t_{EVAC} [s]	t_{PUR} [s]	t_{PREQ1} [s]	t_{PREQ2} [s]	$\mathrm{t_{DePre}}$ [s]	v_{feed} $[m/s]$	v_{PUR} $[m/s]$	P_{L} [bar]
A	50	50	20	50	50	30	0.11	0.5	10
B	60	20	20	-	-	-	0.175	0.22	10

Table 4.7: Process conditions for the conceived novel cycle configurations used for scheduling process, The operating conditions are for simulation results that show a target purity and recovery >95% and >90%, respectively

4-Step with Purge and LPP

The four step cycle with LPP and purge is relatively simple cycle to schedule since it has only one step; the LPP step that needs to be aligned with the beginning adsorption step. The scheduling process is done for this cycle by first,non-dimensionalize the step times with the total step time. The total time is now sub divided into equal fractions that are equal to the time of adsorption. The fraction that signifies the adsorption time is taken as the standard step size. Idle time is added at the end of the purge step to make sure the LPP step begins at a time sequence corresponding to the adsorption step. The Fig.4.17 shows one operating condition for the four step cycle; that achieves purity recovery targets, scheduled for use in the eight bed PSA skid.

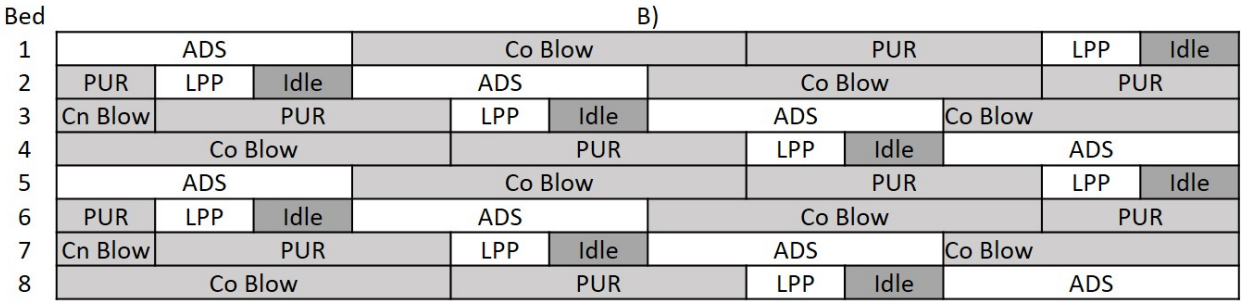

Fig. 4.17: The scheduled 4-step cycle for an 8 bed PSA

9-Step with 2 Pressure Equalization, Depressurization, and LPP

The scheduling of this cycle configuration is not as straight forward as the previous cycle, four step cycle. This is because this cycle has interrelated pressure equalization steps. This cycle has two pressure equalization step, i.e. four; two donor steps, two receiver steps. The constraint is that the first donor step has to align with the second receiver step and visa-verse. The scheduling process is done for this cycle by first, non dimensionalize the step times with the total step time. The total time is now sub divided into equal fractions, equal to the time of adsorption. The fraction that signifies the adsorption time is taken as the standard step size. Idle times are added at the end of the depressurization step to make sure that the pressure equalization step starts at a fresh time division. Thus aligning the four steps. The same process is carried out to align the LPP step. The Fig.4.18 shows one operating condition for the four step cycle; that achieves purity recovery targets, scheduled for use in the eight bed PSA skid.

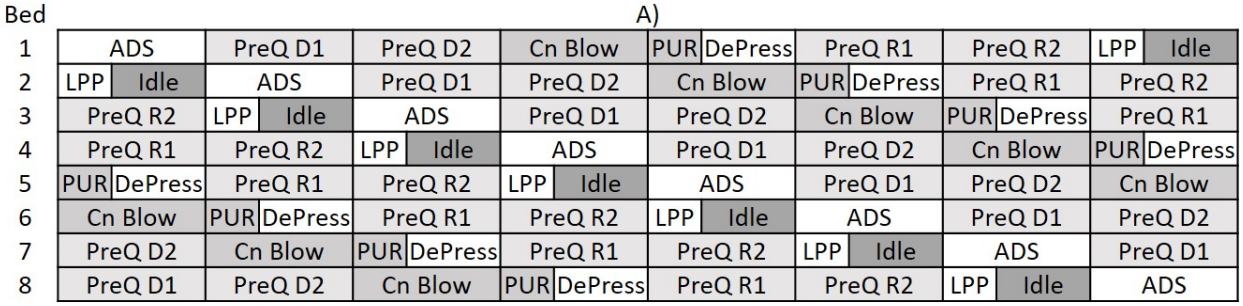

Fig. 4.18: The scheduled 9-step cycle for an 8 bed PSA

4.6 Conclusion

The main aim of this study was to design and schedule PSA cycles for the pre-combustion capture of CO_2 using TDA's AMS-19 adsorbent. The adsorbents equilibrium was described using Sip's

isotherm that was fitted and used in earlier studies conducted on the adsorbent. H_2 isotherm parameters on activated carbon was similarly obtained from the earlier work from the literature to design the PSA cycles. The DOE targets of CO_2 recovery of 90% and CO_2 purity is expected to be 95% and that was the target in this study. A detailed one-dimensional model that was discussed in earlier sections was modified according to the system and solved using an in-house Finite Volume Method (FVM) on MATLAB to best describe the adsorption dynamics in the process. The heat, mass and momentum variables were all solved in space and time for the various steps in a PSA process. Full cycle simulations were performed for the different PSA cycle configurations. The simulations predicted the gas and solid phase column profiles and the temperature profiles, which was then analyzed to improve the performance of the cycles. This also allowed us to make modifications to the cycle configurations to get better performance. The performance indicators, namely the purity and recovery of CO_2 and H_2 were calculated at the cyclic steady state. The PSA cycles were designed to get close to the DOE targets while still being able to run on a lab scale test PSA. A need, therefore, arose to look into newer simpler cycles that could still to achieve the DOE targets. A three pressure equalization cycle was studied along with the role of feed and pressure equalization instead of product end to avoid contamination of the H_2 product. It was noticed that by lower the pressure of the bed after the collection of the extract product, allowed for the intermediate pressure to be reduced. This prompted to the inclusion of a novel depressurization step after the purge step. This addition led to the increase in CO_2 purity but not at a loss of CO_2 Recovery in the overall cycle. A new simple 4 step cycle was simulated without the use of an evacuation step and this cycle was optimized for purity and recovery. It was found to satisfy both the DOE targets and could be scheduled easily into a 8 bed PSA skid based on its simplicity in configuration. This simplistic design also allows the collection of CO_2 at a higher pressure, at the expense of using a H_2 compressor for the Hydrogen collected at lower pressure. The process conditions used for the PSA cycle simulations are not optimized for performance metrics such as purity and recovery, but further cycle optimization studies including energy consumption and productivity will have to be carried out to have a complete picture when it comes to material and process performance. The optimizations of the performance indicators (purity and recovery of CO_2) revealed that a 4 Step PSA cycle with a steam purge and LPP achieves the target purity and recovery targets. The cycles that achieved the DOE targets were scheduled graphically to be run in a 8 bed pilot scale plant.

Chapter 5

Concluding remarks

5.1 Conclusions

This thesis dealt with PSA cycle configuration for adsorption based carbon capture technologies. The two main Capture technologies post and pre combustion technologies were looked into for avenues to implement adsorbent based capture.

In the first part of the thesis, the adsorption equilibria of the various S-Shape MOFs [1, 2] was fitted to a wDSL isotherm to help describe both its temperature and pressure behavior. The model was used in an in-house process simulator and a four step LPP cycle was simulated for each of the materials. A key relation between feed temperature and evacuation pressure was also found. A study relating the performance of the process to the feed temperature was also performed to highlight this relation. To judge their potential in a process the performance indicators, purity and recovery were optimized, with feed temperature as a decision variable. The performance of these diamine-appended metal-organic framework adsorbents was then compared to the performance of Zeolite 13X. It was found that the MOF-Mn and MOF-Mg showed performance advantages over the Zeolite 13X in terms of purity and recovery. The MOF-Mn was found to be energetically better than the Zeolite 13X, but this was found not to be due to the S-Shape. To achieve better performance from these materials, cycles designed to better capture the adsorption dynamics of this material are suggested as a future study. It was shown that the energy advantage shown by the material was due to the low N_2 affinity of the MOF material.

The second part of this thesis concentrated on the pre-combustion carbon capture. Here the main aim was to design and schedule PSA cycles for the pre-combustion capture of CO_2 using TDA AMS-19 adsorbent in an IGCC power plant. The system feed used was syn-gas, which is a mixture of 40/60 of CO_2/H_2 at 35 bar pressure and 240 $\circ$C temperature. LP steam was used as a third inert component and was used in a low pressure purge step to improve CO_2 recovery. The adsorbents equilibrium was described using the same Sips isotherm that was fitted and used in earlier studies

conducted on the adsorbent [11]. H_2 isotherm parameters on activated carbon were similarly obtained from the earlier work from the literature to design the PSA cycles. Cycles were configured in order to achieve the targets for CO_2 purity and CO_2 recovery is 95% and 90%, respectively. Six new cycles were configured and their performance was analyzed. The modifications that were made were systematically analyzed and compared to previously configured cycles to show improvement, with the ultimate aim of achieving DOE targets for CO_2 purity and recovery of 95% and 90%, respectively. The optimized cycle points were scheduled to a pilot scale 8 bed PSA unit for in field testing.

5.2 Outlook

In this work, a detailed one dimensional non-isothermal, nonisobaric model was used to simulate the adsorption process. This along with a Genetic Algorithm based optimization strategy was used to predict the performance of adsorbents in a CO_2 capture plant for both pre and post-combustion CO_2 capture.

In the post combustion part of this work, a detailed optimization study was carried out for MOF structures published by McDonald *et.al.* [1,2]. These materials showed an unusual S-Shape isotherm for CO_2, which may have process advantages over standard type 1 isotherm. The simulation of these materials were performed in non isothermal conditions. The optimized performance of these materials showed an advantage in terms achieving of DOE set purity and recovery for CO_2 capture. They also showed advantage in operational costs over the benchmark adsorbent for CO_2 capture, which is Zeolite 13X. But the simulation of these materials were carried out in a four step cycle with LPP. This configuration was developed for the CO_2 capture using a typical type 1 CO_2 isotherm. Hence to fully understand the potential of the material a more suitable configuration based on its adsorption dynamics needs to be configured. It was also assumed that the N_2 isotherm was common for all the MOF materials. In the future work it would be helpful to have specific N_2 adsorption data. Breakthrough measurements would also help in understanding the adsorption mechanics better, and thus model the process with better accuracy. The competition of the gases in the system were predicted using single component measures and IAST, the availability of binary measurements would help in validating the IAS and model predictions.

In the pre-combustion part of this work, PSA cycle configurations were developed for an activated carbon developed by TDA Research Inc. These cycles were configured assuming a H_2 isotherm from the literature, an accurately measured H_2 would be preferred. Pilot scale experiments being run for the material, using the scheduled cycles would help in validating the results form the study. A future work would also involve the optimization of all the promising PSA cycles, to obtain the best operating conditions. A plant wide energy analysis would also help in understanding the cost of LP steam usage in the PSA process.

Bibliography

[1] T. M. McDonald, F. A. Mason, X. Kong, E. D. Bloch, D. Gygi, A. Dani, V. Crocella, F. Giordanino, S. O. Odoh, W. S. Drisdell, B. Vlaisavljevich, A. L. Dzubak, R. Poloni, S. K. Schnell, N. Planas, K. Lee, T. Pascal, L. F. Wan, D. Prendergast, J. B. Neaton, B. Smit, J. B. Kortright, L. Gagliardi, S. Bordiga, J. A. Reimer, and J. R. Long, "Cooperative insertion of CO_2 in diamine-appended metal-organic frameworks," *Nature*, vol. 14327, 2015.

[2] T. M. McDonald, W. R. Lee, J. A. Mason, B. M. Wiers, C. S. Hong, and J. R. Long, "Capture of carbon dioxide from air and flue gas in the alkylamine-appended metal–organic framework mmen-Mg_2(dobpdc)," *Journal of the American Chemical Society*, vol. 134, pp. 7056–7065, April 2012.

[3] J.-R. Petit, J. Jouzel, D. Raynaud, N. I. Barkov, J.-M. Barnola, I. Basile, M. Bender, J. Chappellaz, M. Davis, G. Delaygue, *et al.*, "Climate and atmospheric history of the past 420,000 years from the vostok ice core, antarctica," *Nature*, vol. 399, no. 6735, pp. 429–436, 1999.

[4] E. Web, "Esrl global monitoring division-global greenhouse gas reference network," 2005.

[5] NASA, "Nasa's goddard institute for space studies (giss) global land-ocean temperature index, avalible online at https://climate.nasa.gov/vital-signs/global-temperature.html," 2017.

[6] IEA, "International energy agency, 20 years of carbon capture and storage, avalible at https://www.iea.org/publications/freepublications/publication/20-years-of-carbon-capture-and-storage.html," 2016.

[7] D. Y. Leung, G. Caramanna, and M. M. Maroto-Valer, "An overview of current status of carbon dioxide capture and storage technologies," *Renewable and Sustainable Energy Reviews*, vol. 39, pp. 426–443, 2014.

[8] D. M. Ruthven, *Principles of Adsorption and Adsorption Processes*. John Wiley & Sons, 1984.

[9] R. Haghpanah, A. Majumder, R. Nilam, A. Rajendran, S. Farooq, I. A. Karimi, and M. Amanullah, "Multiobjective optimization of a four-step adsorption process for postcombustion CO_2 capture via finite volume simulation," *Industrial & Engineering Chemistry Research*, vol. 52, pp. 4249–4265, 2013.

[10] D. M. Ruthven, S. Farooq, and K. S. Knaebel, *Pressure swing adsorption.* New York, N.Y.: VCH Publishers, 1994.

[11] A. K. Rajagopalan, "Material selection and process design for adsorptive CO_2 capture," 2015.

[12] M. Hefti, L. Joss, Z. Bjelobrk, and M. Mazzotti, "On the potential of phase-change adsorbents for CO_2 capture by temperature swing adsorption," *Faraday discussions*, vol. 192, pp. 153–179, 2016.

[13] N. L. B. Lisa V. Alexander, Simon K. Allen, "Climate change 2013 the physical science book."

[14] R. Knutti and J. Sedláček, "Robustness and uncertainties in the new cmip5 climate model projections," *Nature Climate Change*, vol. 3, p. 369–373, 2013.

[15] B. Metz, O. Davidson, H. De Coninck, M. Loos, and L. Meyer, "Ipcc special report on carbon dioxide capture and storage," tech. rep., Intergovernmental Panel on Climate Change, Geneva (Switzerland). Working Group III, 2005.

[16] R. Van Noorden, "Two plants to put 'clean coal'to test," *Nature*, vol. 509, no. 7498, p. 20, 2014.

[17] "National energy board, market snapshot: Canadian carbon capture and storage projects will soon sequester up to 6.4 million tonnes of CO_2 per year, availible online at https://www.neb-one.gc.ca/nrg/ntgrtd/mrkt/snpsht/2016/09-01cndncrbncptr-eng.html," 2016.

[18] M. M. Hossain and H. I. de Lasa, "Chemical-looping combustion (clc) for inherent CO_2 separations , a review," *Chem. Eng. Sci*, vol. 63, no. 18, pp. 4433–4451, 2008.

[19] B. Metz, O. Davidson, H. de Coninck, M. Loos, and L. Meyer, *Carbon Dioxide Capture and Storage.* Cambridge University Press, 2005.

[20] M. Tagliabue, D. Farrusseng, S. Valencia, S. Aguado, U. Ravon, C. Rizzo, A. Corma, and C. Mirodatos, "Natural gas treating by selective adsorption: Material science and chemical engineering interplay," *Chem. Eng. J.*, vol. 155, no. 3, pp. 553 – 566, 2009.

[21] J. Zhang, P. A. Webley, and P. Xiao, "Effect of process parameters on power requirements of vacuum swing adsorption technology for CO_2 capture from flue gas," *Energy Conversion and Management*, vol. 49, no. 2, pp. 346–356, 2008.

[22] J. Zhang and P. A. Webley, "Cycle development and design for CO_2 capture from flue gas by vacuum swing adsorption," *Environmental science & technology*, vol. 42, no. 2, pp. 563–569, 2007.

[23] R. Haghpanah, R. Nilam, A. Rajendran, S. Farooq, and I. A. Karimi, "Cycle synthesis and optimization of a vsa process for postcombustion CO_2 capture," *AIChE Journal*, vol. 59, pp. 4735–4748, August 2013.

[24] D. Marx, L. Joss, M. Hefti, and M. Mazzotti, "Temperature swing adsorption for postcombustion CO_2 capture: single-and multicolumn experiments and simulations," *Industrial & Engineering Chemistry Research*, vol. 55, no. 5, pp. 1401–1412, 2016.

[25] S. Choi, J. H. Drese, and C. W. Jones, "Adsorbent material for carbon dioxide capture from large anthropogenic point sources," *ChemSusChem*, vol. 2, pp. 796 – 854, 2009.

[26] R. V. Siriwardane, M.-S. Shen, E. P. Fisher, and J. A. Poston, "Adsorption of CO_2 on molecular sieves and activated carbon," *Energy & Fuels*, vol. 15, no. 2, pp. 279–284, 2001.

[27] G. Li, P. Xiao, P. A. Webley, J. Zhang, and R. Singh, "Competition of CO_2/H_2O in adsorption based CO_2 capture," *Energy Procedia*, vol. 1, pp. 1123–1130, 2009.

[28] G. Li, P. Xiao, J. Zhang, and P. A. Webley, "The role of water on postcombustion CO_2 capture by vacuum swing adsorption: Bed layering and purge to feed ratio," *AIChE Journal*, vol. 60, pp. 673–689, Feb 2014.

[29] G. Li, P. Xiao, P. Webley, J. Zhang, R. Singh, and M. Marshall, "Capture of co2 from high humidity flue gas by vacuum swing adsorption with zeolite 13x," *Adsorption*, vol. 14, no. 2-3, pp. 415–422, 2008.

[30] H. Li, M. Eddaoudi, M. O'Keeffe, and O. M. Yaghi, "Design and synthesis of an exceptionally stable and highly porous metal-organic framework," *Nature*, vol. 402, no. 6759, pp. 276–279, 1999.

[31] J. R. L. Li, R. J. Kuppler, and H. C. Zhou, "Selective gas adsorption and separation in metal-organic frameworks," *Chemical Society Reviews*, vol. 38, pp. 1477–1504, 2009.

[32] S. Sircar, T. Golden, and M. Rao, "Activated carbon for gas separation and storage," *Carbon*, vol. 34, no. 1, pp. 1–12, 1996.

[33] A. K. Rajagopalan, A. M. Avila, and A. Rajendran, "Do adsorbent screening metrics predict process performance? a process optimisation based study for post-combustion capture of CO_2," *International Journal of Greenhouse Gas Control*, vol. 46, pp. 76–85, 2016.

[34] N. Casas, J. Schell, L. Joss, and M. Mazzotti, "A parametric study of a psa process for pre-combustion CO_2 capture," *Separation and Purification Technology*, vol. 104, pp. 183–192, 2013.

[35] A. L. Myers and J. M. Prausnitz, "Thermodynamics of mixed-gas adsorption.," *AIChE J.*, vol. 11, no. 1, p. 121, 1965.

[36] D. Do, *Adsorption Analysis: Equilibria and Kinetics*. Chemical Engineer Series, Volume 2, Imperial College Press, 1998.

[37] I. Langmuir, "The adsorption of gases on plane surfaces of glass, mica and platinum.," *Journal of the American Chemical society*, vol. 40, no. 9, pp. 1361–1403, 1918.

[38] T. Remy, G. V. Baron, and J. F. Denayer, "Modeling the effect of structural changes during dynamic separation processes on mofs," *Langmuir*, vol. 27, no. 21, pp. 13064–13071, 2011.

[39] J. D. Baboolal, "Evaluation of novel metal-organic framework materials for adsorptive post-combustion CO_2 capture," Master's thesis, University of Alberta, 2015.

[40] R. Sips, "On the structure of a catalyst surface," *The Journal of Chemical Physics*, vol. 16, no. 5, pp. 490–495, 1948.

[41] S. A. Hosseinzadeh Hejazi, A. Rajendran, J. A. Sawada, and S. M. Kuznicki, "Dynamic column breakthrough and process studies of high-purity oxygen production using silver-exchanged titanosilicates," *Industrial & Engineering Chemistry Research*, vol. 55, no. 20, pp. 5993–6005, 2016.

[42] S.-J. Lin, W. C. Chao, Y. C. Sud, and G. K. Walker, "A class of the van leer-type transport schemes and its application to the moisture transport in a general circulation model," *Mon. Wea. Rev.*, vol. 122, pp. 1575–1593, July 1994.

[43] B. van Leer, "Towards the ultimate conservative difference scheme. v. a second-order sequel to godunov's method," *Journal of Computational Physics*, vol. 32, no. 1, pp. 101 – 136, 1979.

[44] L. E. Perez, "Ethane recovery from residue gas using pressure swing adsorption," Master's thesis, 2015.

[45] P. Danckwerts, "Continuous flow systems: distribution of residence times," *Chem. Eng. Sci*, vol. 2, no. 1, pp. 1–13, 1953.

[46] M. W. M. Matuszewski, "Quality guidlines for energy system studies: CO_2 impurity design parameters," 2012.

[47] NETL, "National energy technology laboratory, carbon capture technology program plan," January 2013.

[48] K. Deb, A. Pratap, S. Agarwal, and T. Meyarivan, "A fast and elitist multiobjective genetic algorithm: NSGA-II," *IEEE Trans. Evol. Comput.*, vol. 6, pp. 182–197, Apr 2002.

[49] R. Ben-Mansour, M. Habib, O. Bamidele, M. Basha, N. Qasem, A. Peedikakkal, T. Laoui, and M. Ali, "Carbon capture by physical adsorption: Materials, experimental investigations and numerical modeling and simulations–a review," *Applied Energy*, vol. 161, pp. 225–255, 2016.

[50] D. Xu, P. Xiao, J. Zhang, G. Li, G. Xiao, P. A. Webley, and Y. Zhai, "Effects of water vapour on CO_2 capture with vacuum swing adsorption using activated carbon," *Chem. Eng. Sci*, vol. 230, pp. 64 – 72, 2013.

[51] P. Nugent, Y. Belmabkhout, S. D. Burd, A. J. Cairns, R. Luebke, K. Forrest, T. Pham, S. Ma, B. Space, L. Wojtas, M. Eddaoudi, and M. J. Zaworotko, "Porous materials with optimal

adsorption thermodynamics and kinetics for CO_2 separation.," *Nature*, vol. 495, pp. 80 – 84, 2013.

[52] E. Magano, D. Friedrich, and S. Brandani, "Robust algorithms for the solution of the ideal adsorbed solution theory," *AIChE Journal*, 2014.

[53] H. O. R. Landa, D. Flockerzi, and A. Seidel-Morgenstern, "A method for efficiently solving the iast equations with an application to adsorber dynamics," *AIChE Journal*, vol. 59, no. 4, pp. 1263–1273, 2013.

[54] W. Zhang, Y. Shan, and A. Seidel-Morgenstern, "Breakthrough curves and elution profiles of single solutes in case of adsorption isotherms with two inflection points," *Journal of Chromatography A*, vol. 1107, no. 1, pp. 216–225, 2006.

[55] M. Mazzotti and A. Rajendran, "Equilibrium theory–based analysis of nonlinear waves in separation processes," *Annual review of chemical and biomolecular engineering*, vol. 4, pp. 119–141, 2013.

[56] M. Khurana and S. Farooq, "Simulation and optimization of a 6-step dual-reflux vsa cycle for post-combustion CO_2 capture," *Chem. Eng. Sci*, vol. 152, pp. 507–515, 2016.

[57] A. D. Ebner, A. Mehrotra, and J. A. Ritter, "Graphical approach for complex psa cycle scheduling," *Adsorption*, vol. 15, no. 4, pp. 406–421, 2009.

Appendix A

Nomenclature

A	Cross sectional area of column [m]
c	Gas phase concentration [$m^3 mol^{-1}$]
C_{pa}	Adsorbed phase specific heat capacity [J $kg^{-1} K^{-1}$]
C_{pg}	Gas phase specific heat capacity [J $kg^{-1} K^{-1}$]
C_{ps}	Adsorbent specific heat capacity [J $kg^{-1} K^{-1}$]
C_{pw}	Column wall specific heat capacity [J $kg^{-1} K^{-1}$]
D_M	Molecular diffusivity at 1 atm and 298 K [$m^2 s^{-1}$]
D_L	Axial dispersion coefficient [$m^2 s^{-1}$]
f	State variable
f_j	Cell average of the state variable
h_i	Inside heat transfer coefficient [W $m^{-2} K^{-1}$]
h_o	Outside heat transfer coefficient [W $m^{-2} K^{-1}$]
H	Enthalpy [J mol^{-1}]
k	mass transfer coefficient [s^{-1}]
K_w	Wall thermal conductivity [$W\ m^{-1} K^{-1}$]
K_Z	Effective gas thermal conductivity [W $m^{-1} K^{-1}$]
L	Column length [m]
P	Pressure [Pa]
$\bar{P}$	Dimensionless pressure
Pe	Peclet Number
Pe_h	Heat transfer Peclet number
q	Solid phase concentration [mol m^{-3}]
q_s	Reference saturation loading [mol m^{-3}]
r_i	Column inner radius [m]

r_o	Column outer radius [m]
r_p	Particle radius [m]
R	Universal gas constant [J $mol^{-1}K^{-1}$]
t	Time [s]
T	Temperature [K]
$\bar{T}$	Dimensionless temperature
$\bar{T}_a$	Dimensionless ambient temperature
$\bar{T}_w$	Dimensionless wall temperature
v_{feed}	Interstitial velocity [m s^{-1}]
$\bar{v}$	Dimensionless velcoity
x	Dimensionless solid phase composition
x^*	Dimensionless equilibrium solid phase composition
y	Gas phase mole fraction
Z	Dimensionless axial position
α	Dimensionless mass transfer coefficient
ε_b	Bed voidage
ε_p	Particle voidage
μ	Fluid viscosity [kg $m^{-1}s^{-1}$]
ρ_b	Bulk density of fluid [g cm^{-3}]
ρ_g	Density of fluid [kg m^{-3}]
ρ_s	Density of adsorbent [kg m^{-3}]
ρ_w	Density of column wall [kg m^{-3}]
Π	Dimensionless group in wall energy balance
τ	Dimensionless time
τ'	Tortuosity
Ω	Dimensionless group in column energy balance
Ψ	Dimensionless group in mass balance